Thesis

Salient features of the D3R radar enhancements

Submitted by

Shashank S. Joshil

Department of Electrical and Computer Engineering

In partial fulfillment of the requirements

For the Degree of Master of Science

Colorado State University

Fort Collins, Colorado

Fall 2018

Master's Committee:

Advisor: V. Chandrasekar

Anura P. Jayasumana
Susan P. James

Abstract

Salient features of the D3R radar enhancements

D3R radar was developed to serve as a ground validation tool for the dual precipitation radar in the core satellite for the Global Precipitation Measurement mission. In order to have more flexibility in operations and improve the features of D3R, the radar was upgraded. Simulations were carried out so that the best design could be determined and implemented on the upgraded D3R (D3R 2.0). The IF subsystems and the digital receiver module which consist of arbitrary waveform generators and the digital receivers of the Ku and Ka bands were changed to support the new features. To enhance signal processing features and make the system compatible with the new design, the D3R software was also upgraded. In this thesis, the design, implementation and tests carried out during the upgrade work for the D3R are presented. The range-velocity ambiguity techniques which work well with low frequency radars pose a challenge in the case of higher frequency radars such as in D3R due to limited Doppler spectrum available. The existing method in D3R to mitigate the range ambiguity problem using random phase codes and staggered PRT is analyzed and the performance of the method is demonstrated for D3R data. The performance of random phase codes and systematic phase codes for range ambiguity mitigation and future changes in D3R 2.0 range ambiguity mitigation technique are discussed. A velocity ambiguity mitigation technique using the dual-frequency information is developed for D3R 2.0; the implementation is explained along with its performance on radar observations. The D3R 2.0 went through initial calibration and testing before being deployed to the ICE-POP field campaign in South Korea. The first results after the upgrade are presented.

Acknowledgments

The graduate school experience at Colorado State University has been extremely valuable. I am thankful and indebted to my advisor Dr. V. Chandrasekar for his kindness, support, guidance and encouragement through my graduate study. Also, I would like to thank Dr. Anura P. Jayasumana and Dr. Susan P. James for serving as my committee members. I would like to thank Dr. Robert Beauchamp, Dr. Haonan Chen and Dr. Renzo Bechini for their guidance and inputs for my research. I would like to thank all the members of the radar group at Colorado State University, Mohit Kumar, Ryan Gooch, Sounak Biswas, Ivan Arias, Alexander Morin, Haiming Tan, Pratik Ramdasi, Dr. Minda Le, Amit Dutta, Sergio Graniello and Zach Mendez for your help during my graduate studies. I would like to thank Dr. Walter Petersen and David Wolff for their encouagement and support during my graduate work. I would also like to thank Dr. Manuel Vega for his inputs during my graduate work. I would like to express my gratitude to the staff at the CSU-CHILL radar facility, Jim George, Dr. Francesc Junyent and Pat Kennedy for their help during my graduate studies. I am deeply grateful to my parents, friends and family for their love, support and encouragement throughout the years in my graduate studies. This research is supported by the NASA GPM program.

Table of contents

List of tables

List of figures

Chapter 1

Introduction

1.1. Introduction to weather radars

Remote sensing plays a prominent role in various fields such as hydrology, meteorology and climate studies. Radio detection and ranging (RADAR) was researched and invented during the period of world war II. Since then, the applications of Radar have found uses in the areas of aviation, object tracking and remote sensing. Radar is the major tool in remote sensing which provides high resolution reliable data for a large span of area.

Radar is a complex system which uses electromagnetic waves to detect the position, size, speed and even shape of a target. The Radar system sends out electromagnetic signals in a particular direction; this signal travels through the propagation medium and the target scatters the incident signal. The signal is scattered isotropically from the target and some parts of the signal travel towards the radar. Radar receives this weak backscattered signal and information is extracted to characterize the target. This simple radar concept was operating in the initial days of radar technology. The next addition to the radar technology was the Doppler processing, which has the ability to measure velocity based on the change in frequency on the backscattered signal. Next came pulsed Doppler radar in which the radar sends out pulses of signal instead of sending a continuous signal. The next significant change in the radar technology came with the dual-polarization ability of the radars. In this instead of transmitting a single polarization signal, two signals with two polarizations (horizontal and vertical) are transmitted and the corresponding backscattered signals are received and processed.

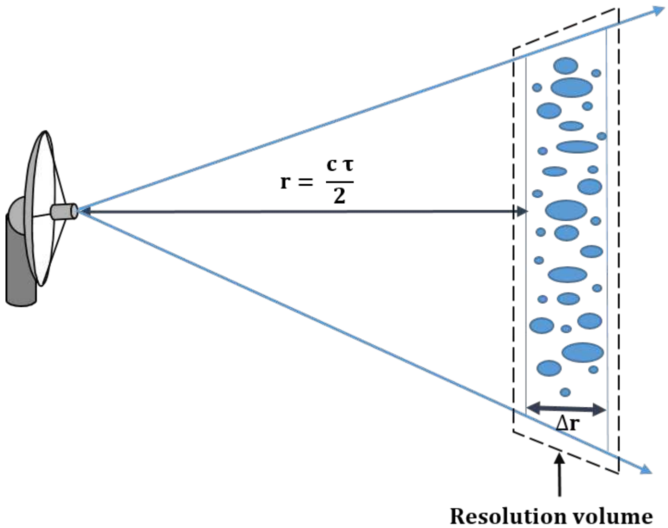

FIGURE 1.1. The incremental voltage due to scattering of particles located within a resolution volume ranging from (r, r+Δr).

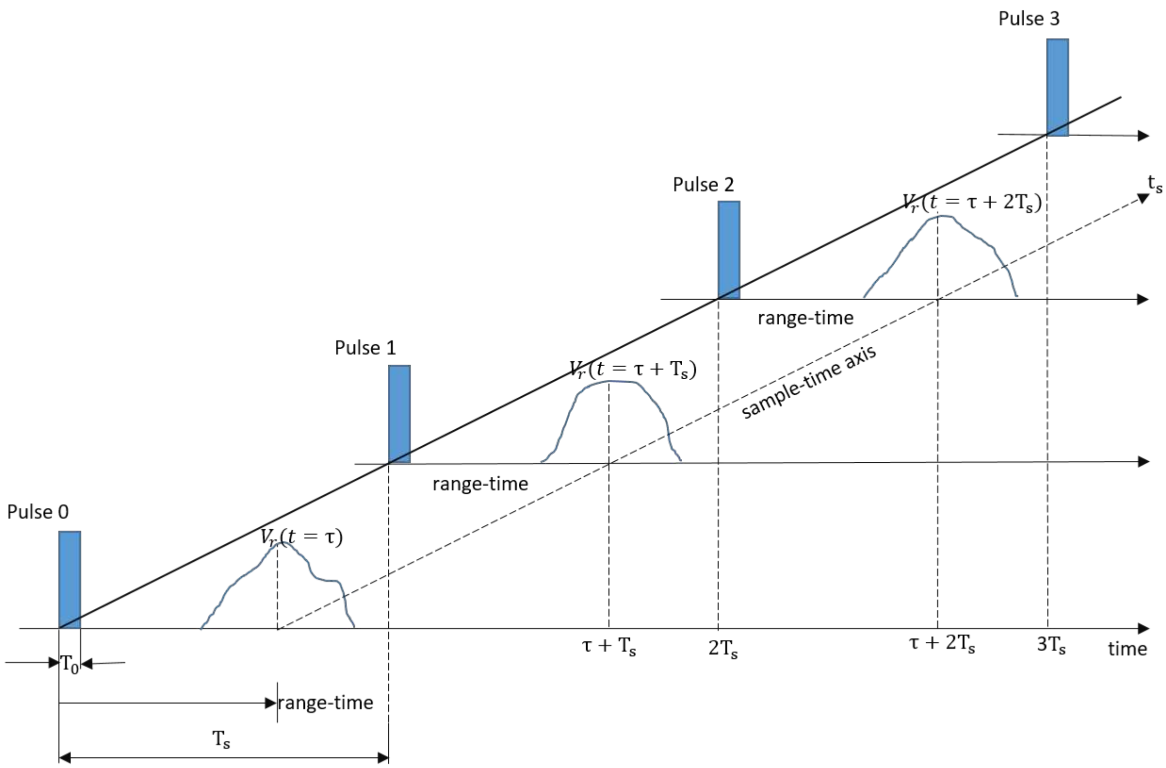

FIGURE 1.2. Illustration of range-time axis and sample-time axis with a pulse repetition time of T_s

.

The radars which are used to measure and characterize precipitation events are known as weather radars. Today most weather radars are pulsed radars and have the capability of Doppler and dual-polarization. Weather radars work on the same principle as hard target radars except that the target here is the precipitation volume. The target is not a single point; rather it is a collective distribution of particles over a volume. The volume which the radar samples is the range resolution volume, which extends radially from r to r+δr and the received voltage $V_r(t)$ at $t = \tau$ is based on the scattering of particles located within the resolution volume as illustrated in figure 1.1. Resolution volumes are typically spaced $cT_0/2$ apart, where T_0 is the pulse width [3]. The smaller the range resolution volume, the more information we get about the precipitation event. Pulsed radar transmits a train of pulses at a time interval known as the pulse repetition time (PRT). These train of pulses are sampled and are divided into range-time and sample-time. For a periodic pulsed train T_s apart, the range-time and sample-time is illustrated in figure 1.2.

The range$-$time for a single pulse transmitted is given by $r = 2\tau/c$, and the received voltage $V_r(t)$ at $t = \tau$ is due to back scatter from particles located in the resolution volume at rangetime . Here, for a periodic train of pulses, the received voltage at the same rangetime is given as $V_r(t = \tau)$, $V_r(t = \tau + T_s)$, . . . , $V_r(t = \tau + nT_s)$ which forms a sequence of temporal samples from the same resolution volume. The received voltage value for a given range$-$time can be viewed as uniformly spaced samples along the sample$-$time axis t_s. From this we can define the received voltage as a two$-$dimensional function with respect to range$-$time and sample$-$time. Due to the time varying properties of particles located in the resolution volume which correspond to τ, we see fluctuations in the sample$-$time axis.

The signal received by the radar is a complex stochastic signal. For a stochastic signal, the power spectral density provides the decomposition of the signal power into various frequencies contained in the signal. A Gaussian-shaped power spectral density or the Doppler spectrum [3] is given as

(1) $$S(\Omega) = \sum_{n=-\infty}^{\infty} R(n) e^{-j\Omega n}$$

The corresponding Doppler velocity spectrum is given by

(2) $$S(v) = \frac{S_0}{\sigma_v\sqrt{2\pi}} exp[-\frac{(v-\hat{v})^2}{2\sigma_v^2}]$$

The autocorrelation coefficient for a reflectivity weighed velocity spectrum is given as

(3) $$R(n) = |R(0)| e^{-j\frac{4\pi}{\lambda}\hat{v}nT_s} exp(-\frac{8\pi^2}{\lambda^2}\sigma_v^2 n^2 T_s^2)$$

where $\hat{v}$ is the mean Doppler velocity and σ_v is the Doppler spectral width.

Pulsed Doppler weather radars with polarization diversity can transmit and/or receive two orthogonal polarized signals. The transmission and reception of the signal in most pulsed radar systems is achieved through a single antenna. The intrinsic backscattering properties of particles in the resolution volume from the two polarization states enables measurement of characteristics of the particles such as size, shape, spatial orientation and type. The backscattering covariance matrix is used to describe these characteristics and is given as

(4) $$\Sigma_{BSA} =< \begin{bmatrix} |S_{hh}|^2 & \sqrt{2}S_{hh}S_{hv}^* & S_{hh}S_{vv}^* \\ \sqrt{2}S_{hv}S_{vv}^* & 2|S_{hv}|^2 & \sqrt{2}S_{hv}S_{vv}^* \\ S_{vv}S_{hh}^* & \sqrt{2}S_{vv}S_{hv}^* & |S_{hh}|^2 \end{bmatrix} >$$

Where S_{hh}, S_{hv}, S_{vh} and S_{vv} are the elements of the scattering matrix and angle brackets represents the ensemble averaging. The subscripts vh refers to "transmit horizontal polarization and receive vertical polarization" and vice versa. * denotes complex conjugate. Polarimetric variables are computed using the backscattering covariance matrix elements. Meteorological moments and polarimetric variables are estimated from the covariance matrix of the vector of received signals. The received signal **Z** and the corresponding covariance matrix **K** are given by

$$\mathbf{Z} = \begin{bmatrix} V_{hh} & V_{hv} & V_{vh} & V_{vv} \end{bmatrix}^T \tag{5}$$

$$\mathbf{K} = E[\mathbf{Z}\mathbf{Z}^{\mathbf{H}}] = E \begin{bmatrix} |V_{hh}|^2 & V_{hh}V_{vh}^* & V_{hh}V_{hv}^* & V_{hh}V_{vv}^* \\ V_{vh}V_{hh}^* & |V_{vh}|^2 & V_{vh}V_{hv}^* & V_{vh}V_{vv}^* \\ V_{hv}V_{hh}^* & V_{hv}V_{vh}^* & |V_{hv}|^2 & V_{hv}V_{vv}^* \\ V_{vv}V_{hh}^* & V_{vv}V_{vh}^* & V_{vv}V_{hv}^* & |V_{vv}|^2 \end{bmatrix} \tag{6}$$

Where T indicates transpose and H is the Hermitian operator. The elements of **K** give us the estimates of Σ_{BSA} . The relationship between **K** and Σ_{BSA} is given by

$$\mathbf{K} = \frac{C\Sigma_{BSA}}{r_0^2} \tag{7}$$

Where C is the radar constant and r_0 is the radar range to the resolution matrix of measurement. The various radar moments are now calculated as below

(1) Equivalent reflectivity factor: The radar reflectivity (η) is the backscattering cross section per unit volume and is dependent on the number, shape, physical state and their aspect with respect to the radar. In radar meteorology, it is conventional to represent η in terms of the equivalent reflectivity factor (Z_e). Z_e is the product of the received power, radar constant and the range factor expressed in mm^6m^{-1} or dBZ in decibel scale. The equivalent reflectivity factor in the decibel scale is given as below

(8) $$Z = P(dBm) + C + 20logr$$

where $P(dBm)$ is the received power, C is the radar constant and r is the range. For a horizontally polarized received signal the received power is given by

(9) $$P^h =< |V_{hh}|^2 >$$

(2) Differential reflectivity: The differential reflectivity (Zdr) gives the difference in received energy from the horizontal and vertical polarizations. In the decibel scale, Zdr is the difference between the horizontal and vertical received power as given below

(10) $$Zdr = P^h(dB) - P^v(dB)$$

(3) Co-polar correlation: The behavior of the horizontal and vertical polarized pulses within the resolution volume is measured using the Co-polar correlation. The values extend from 0 to 1 with higher values indicating similar behavior and lower values indicating dissimilar behavior. The co-polar correlation is given as

$$\rho_{HV} = \frac{| < V_{hh} V_{vv}^* > |}{\sqrt{P^h}\sqrt{P^v}} \tag{11}$$

(4) Differential Phase shift: The phase shift between the horizontal and vertical signal as the signal propagates through the propagation medium gives the differential phase shift. The phase of the complex correlation between the co-polar signals provides the differential phase as below

$$\phi_{dp} = arg[< V_{hh} V_{vv}^* >] \tag{12}$$

(5) Velocity: The relationship between the wavelength (λ), Doppler frequency shift (f_d) and the radial velocity is given by

$$v_r = -\frac{\lambda f_d}{2} \tag{13}$$

The negative sign in the above equation indicates that the precipitation particles are moving towards the radar. The maximum Doppler shift that can be measured is dependent on the PRT and is given by

$$f_{max} = \frac{1}{2PRT} \tag{14}$$

(6) Spectral width: This gives the information of distribution of the velocities in a resolution volume. It is the spread of the Doppler power spectrum and is computed using the variance.

1.2. Development and operations of D3R

The Tropical Rainfall Measurement Mission (TRMM) was developed as a joint collaboration between the National Aeronautics and Space Administration (NASA) and Japan Aerospace exploration (JAXA) to study rainfall from the view of a satellite, for climate and weather research. The TRMM satellite was launched in November 1997, with a design lifetime of 3 years. The satellite worked exceptionally well after the design lifetime and provided data for over 17 years. It was retired on April 2015. On board the satellite were many instruments, one among them was the precipitation radar. The precipitation radar was the first space borne instrument to provide a three dimensional storm structure. This radar was a single frequency radar operating at the Ku-band.

After this successful mission to map rainfall and aid climate and weather studies, the next mission following the TRMM was the Global Precipitation Measurement (GPM) mission. GPM is a network of satellites which provide global observations of rain and snow. GPM has a core satellite carrying radar and radiometric instruments to measure precipitation from space and serve as a standard for the remaining satellites that map precipitation. On board the GPM core satellite is the Ka-Ku band dual-frequency precipitation radar (DPR) that can make observations of the parameters directly related to the micro physics of precipitation, such as raindrop size distribution and rainfall rate. The Ku band is nearly the same as the TRMM precipitation radar while the Ka band provides higher sensitivity and is useful in measuring snow and light rain.

As we have measurements from two frequency bands, we can use the dual wavelength retrieval methods can be used to calculate drop size distribution and map the characteristics of the precipitation medium. Having dual frequency also enables the use of complex algorithms which perform better in mapping parameters such as rainfall rate. Since GPM's DPR serves as a reference to many instruments on the other satellites in the GPM mission, it is of the highest priority to maintain the quality of data from the DPR. In order to validate the data from DPR, the dual-frequency dual-polarization Doppler radar (D3R) was developed. D3R is a ground validation radar as a part of the GPM Ground Validation (GV) program to enable both physical validation support in terms of understanding the microphysical description of the observations, as well as algorithm retrieval implications [4]. D3R was developed as a joint collaboration between Colorado State University (CSU), NASA and remote sensing solutions. It operates at the nominal frequencies of 13.91 GHz at Ku band and 35.5 GHz at Ka band. It is a fully polarimetric, matched beam scanning weather radar system. The development of the D3R was accomplished using several innovative technologies and it resulted in a relatively compact system which was easily transportable. The D3R can enable more detailed insight into the microphysical structure of precipitation by providing coincident dual-frequency observations at high spatial resolution [5]. Some of the main features of the D3R include the use of a solid state amplifier and a novel waveform composed of three consecutive, frequency modulated, frequency separated pulses.

In the past seven years, the D3R has been in various field campaigns collecting quality data. Pictures of the D3R at various field campaigns are shown in figures 1.3 and 1.4. The

(A) D3R at MC3E field campaign.

(B) D3R at GCPEx field campaign.

(C) D3R at IFloodS field campaign.

FIGURE 1.3. D3R at field campaigns in the past.

geographic and seasonal variability of observations collected thus far with the D3R enables a unique opportunity for comparing regional and seasonal influences on the microphyical properties of precipitation at Ku- and Ka-bands [6]. The first campaign was the Mid-latitude Continental Convective Clouds Experiment (MC3E) which took place from 22nd of April to 6th of June in 2011. The radar was deployed near Lamont, Oklahoma in the region surrounding the Department of Energy (DOE) Atmospheric Radiation Measurement (ARM) Program Southern Great Plains Central Facility. Various instruments were present in this field campaign including a group of seven ground-based multi-frequency cloud and precipitation dual-polarimetric radars.

After this campaign, the D3R was sent to the CSU-CHILL radar facility for testing. Then the D3R was sent to its second field campaign which was the GPM Cold-season Precipitation Experiment (GCPEx). GCPEx field campaign was held from January 2012 to February 2012 in Ontario, Canada. The cold season helped the radar to collect snow data. The shortcomings of the GPM snowfall algorithm was addressed by measuring the microphysical properties and the associated remote sensing observations, in this campaign. The data from this campaign was also used to capture the ability of multi-frequency sensors to detect and estimate falling snow.

The D3R was located in CSU-CHILL radar facility in Greeley, Colorado from March 2012 to April 2013. During this period the D3R collected interesting precipitation data of both rainfall and snow. The simultaneous observations from the D3R and the CHILL S-band radar during this period helped to further investigate the precipitation properties at different frequency bands.

Next, as part of the GV program for the GPM project, the Iowa Flood Studies (IFloodS) field campaign took place in eastern Iowa from May 2013 to June 2013. This was a multi-organization field experiment conducted by NASA and coordinated by the Iowa Flood Center. In IFloodS, a vast network of ground instruments were deployed. These included multiple radars, rain gauges, and disdrometers, with a focus on measuring surface precipitation [7]. In this campaign, D3R was placed along with the NASA N-POL radar to study the triple-frequency evaluation of precipitation. After this campaign, the D3R was in operations at the Wallops Flight Facility (WFF), Virginia from November 2013 to March 2014.

The Integrated Precipitation and Hydrology Experiment (IPHEx) was the next field campaign which took place from April 2015 to June 2015 in the southern Appalachian Mountains in the eastern United States. This was a ground validation field campaign as part of the GPM mission. The goals of this field campaign were to evaluate how well the recently launched GPM core observatory DPR performed and to use the collected precipitation data to evaluate hydrological models and predict the hydrology of the region. From July 2015 to February 2015 D3R was placed in Newark, MD. During this period the D3R was co-located with the NASA N-POL radar.

The next field campaign for D3R was the Olympic Mountain Experiment (OLYMPEX). OLYMPEx field campaign took place in the Olympic Peninsula of Washington State from November 2015 through February 2016. Detailed atmospheric measurements were collected which was used to evaluate how well rain-observing satellites performed. There were various instruments in this field campaign which included aircraft observations. The primary goal of OLYMPEx is to validate rain and snow measurements in mid-latitude frontal systems moving from ocean to coast to mountains, and to determine how remotely sensed measurements of precipitation by GPM can be applied to a range of hydrologic, weather forecasting, and climate applications [8]. After the OLYMPEx field campaign D3R was sent back to the WFF for operations.

To improve the ability of the D3R for measuring precipitation at a finer scale, the radar went through an upgrade from April 2016 to August 2017. During this upgrade, the D3R went through sub-system changes and software upgrade, which will be discussed in detail in further chapters. After the D3R finished the system upgrade, it was sent to the International Collaborative Experiments for Pyeongchang 2018 Olympic and Paralympic Winter Games (ICE-POP 2018) field campaign in PyeongChang region of South Korea from October 2017 to June 2018. This was the first field campaign for the D3R outside the North American continent. During this campaign, the D3R was able to measure rain and snow in the complex terrain of South Korea. Currently, the D3R is at the CSU CHILL facility for further testing the features of the upgrade.

1.3. Organization of the thesis

A brief introduction to weather radars was given in section 1.1. It was also explained in this section how various radar moments are computed from the received signal. In section 1.2 a brief history of development of the D3R was provided; also, the various field campaigns where the D3R was deployed were described.

Chapter 2 describes the salient features of the D3R before the upgrade. The specifications of the D3R are described in section 2.1. Various sub-systems of the D3R are explained in detail with the help of a system architecture in section 2.2. The software architecture along with the networking of the D3R is explained in detail in section 2.3.

Chapter 3 explains the new features of the upgraded D3R. This chapter also explains the process of hardware and software modifications and testing during the upgrade. Section 3.1

(A) D3R at IPHEx field campaign.

(B) D3R at OLYMPEx field campaign.

(C) D3R at WFF.

FIGURE 1.4. D3R at field campaigns in the past.

discusses the hardware modification and changes, details for the new up-converter, down-converter and the digital module sections. The Different IF boards designed and developed are also shown. Section 3.2 explains the changes made in the software architecture of the D3R. Section 3.3 discusses the design aspects of the upgrade. In this section, the mechanical design aspect and the various performance trade-offs used for design are explained. Section 3.4 gives an overall picture of the testing and integration done during the upgrade period.

Chapter 4 provides an overview of the range-velocity ambiguity for Doppler weather radars and methods used to mitigate them. This chapter also discusses the methods used in D3R for the range and velocity ambiguity problem. Section 4.1 explains the range-ambiguity problem in detail. In this section, the second trip echoes and the staggered PRT for dealiasing overlaid echoes are discussed. In section 4.2, the phase coding scheme to characterize and mitigate the second trip echo are explained along with simulation results at Ku band. Section 4.3 explains the method used in D3R for second trip characterization and mitigation along with case studies from the radar. Section 4.4 talks about the velocity correction method used in D3R with simulations and test cases.

Chapter 5 discusses the first results of D3R after the upgrade. Data analysis of the D3R 2.0's data when the radar was deployed in the ICEPOP campaign in South Korea is presented. Section 5.1 speaks about the various calibration procedures which were completed for D3R 2.0 before and after deployment in the field campaign. Section 5.2 presents the analysis of D3R 2.0 data from the field campaign; it also shows the derived moments from the data. Section 5.3 discusses the vertical profile analysis which was performed for the data from the field campaign, this section gives an insight of how dual-polarization variables can be used to interpret different particle types. Section 5.4 shows a comparison of the performance of D3R 2.0 with other instruments in the field campaign.

Chapter 6 summarizes the upgrade work done on the D3R radar along with the features of D3R 2.0. The chapter ends with suggestions for future work.

Chapter 2

The D3R system

The Dual precipitation radar (DPR) on the GPM core satellites is a dual frequency radar space-borne system. The DPR provides observations from the satellite point of view, however being single polarized, it has certain limitations in understanding the microphysical process of the precipitation events. The D3R operating as a dual-frequency dual-polarization Doppler radar provides opportunities to investigate the microphysical aspects of the precipitation events and considered as a self consistent cross-validation tool. Complex algorithms can be developed to retrieve microphysical aspects from the DPR data when the D3R is not in the common observation volume. Microphysical properties of precipitation can be retrieved using the combination of dual-polarization and Doppler observations [9]. Having the features of dual-frequency, dual-polarization and Doppler in the D3R makes it the best candidate for ground validation. This chapter describes the specifications and system description of the D3R before the upgrade.

2.1. Specifications of the D3R

The D3R radar was designed such that it can be deployed in field campaigns to validate data from the DPR and study various microphysical processes. The operation of the D3R was mainly in high-latitude regions, where the observed temperatures had a wide range between -40° to $+40^\circ$ C and wind speed up to 60 miles/hour, this is because the GPM core satellite will be sampling precipitation at high latitudes. Being a transportable system, the D3R had to be assembled and disassembled in various harsh environments such as high wind, snow and unexpected weather conditions. Solid state transmitters were used in the D3R because of various factors such as varying operational temperatures, ability to be controlled remotely,

Table 2.1. Specifications of the D3R

System	
Frequency	13.91 GHz ±25 MHz (Ku band), 35.56 GHz ±25 MHz (Ka band)
Minimum detectable signal	Ku:8dBZ,Ka:3dBZ. Noise equivalent at 15 km and 150 m range resolution
Operational range resolution	150 m (nominal)
Operational range resolution	450 m
Maximum operational range	39.75 km
Angular coverage	0°-360°azimuth, -0.5°-90° elevation (full hemisphere)
Antenna	
Parabolic reflector diameter	Ku: 6 ft (72 in.), Ka: 28 in.
Gain	Ku: 45.6 dBi, Ka: 44.3 dBi
Half-power beam	Ku: 0.86°, Ka: 0.90°
Polarization	Dual linear simultaneous and alternate (H and V)
Maximum sidelobe level	-25dB
Cross-polarization isolation	<-30dB (on axis)
Ka-Ku beam alignment	Within 0.1°
Scan capability	$0°-24°$/ azimuth, $0°-12°$/ elevation
Scan types	PPI sector, RHI, surveillance, fixed, vertical pointing
Transmitter/Receiver	
Transmitter architecture	Solid state power amplifier modules
Peak power	Ku: 200W, Ka: 40 W per H and V channel
Duty cycle	30% maximum
Receiver noise figure	Ku: 4.8, Ka: 6.3
Receiver dynamic range	90 dB
Clutter suppression	GMAP-TD
Data Products	
Standard products	Equivalent reflectivity factor (Z_h), Doppler velocity (Ku unambiguous: 26.97 m/s), Spectral width
Dual-polarization products	Differential Reflectivity (Z_{dr}), Differential Propagation Phase (ϕ_{dp}), Co-polar Correlation Coefficient (ρ_{co}), Linear Depolarization Ratio (LDR) (in alternate mode of operation)
Derived products	Attenuation Corrected Reflectivity (CZ), Attenuation Corrected Differential Reflectivity (CZ_{dr}), Specific Differential Phase (K_{dp}), Rainfall Rate (RR), Drop Size Distribution (D_0, N_w), Hydrometeor types (HID)
Data format	NetCDF

ease of deployment and improved mean time between failures. Since solid state transmitters have low peak power compared to magnetron or klystron, pulse compression methods are used in the system to get the required power and support system sensitivity.

Research on solid state transmitters in the past decade has proven them to be stable and efficient system to be used in radars. Solid-state transmitters being used in precipitation radar systems are becoming increasingly viable [10]. The advantages of using a solid state system include low system operating voltages, more lifetime, no warm-up time as no hot cathodes are present and convenient waveform design implementation. When using pulse compression in radars which use the same antenna for transmission and reception, we encounter the problem of blind range. The blind range is the distance within range where the radar cannot detect signals. The cause of blind range is that the radar cannot be switched to receive mode until the transmitting signal is sent out. Longer the pulse, higher the blind range affecting the radar. To address the problem of blind range which arises due to pulse compression and also to address the issue of low peak power frequency, diverse waveforms are used.

The D3R employs a frequency-diversity waveform which consists of three frequency spaced sub-pulses to achieve its minimum range and sensitivity [1]. The pulse durations of the three pulses are 1 μs (short pulse), 20 μs (medium pulse) and 40 μs (long pulse). The medium and long pulses are nonlinear frequency modulated signals - they have an overall bandwidth of 3.6 MHz. The minimum integrated sidelobe level (ISL) filters used in the digital receiver of weather radars has given promising results [10]. This minimum ISL filter is used for both medium and long pulses. More details on the ISL filter are provided in the next chapter.

The technical specifications of the D3R are given in table 2.1. It can be seen that the Ka band can detect 5 dBZ better than the Ku band. The radar has a maximum operational range of approximately 40 kilometers. In order to accommodate system timing and internal calibration loops, the maximum range is cut off at this value. The radar can execute a full or sectoral plan position indicator (PPI) scan, half or full hemispherical range height indicator (RHI) scan or fixed scan or vertical scan modes. The Ku and Ka antenna alignment are calibrated to be within 0.1°. Various scan rates can be set for the antenna system depending on the antenna beamwidth which defines the angular resolution needed. The antenna beamwidth is related to the scan rate and number of pulses for integration as

$$\theta_B = \frac{N\omega_s}{f_p} \tag{15}$$

Where θ_B is the antenna beamwidth in degrees, ω_s is the scan rate in degrees per second, f_p is the pulse repetition frequency and N is the number of pulses for integration. From this equation, it can be seen that the antenna beamwidth and the scan rate are directly proportional to each other. It was discussed previously that the transmitters for Ku and Ka are solid state and have a peak power of 200 W for Ku and peak power of 40 W for Ka. The receiver dynamic range is 90 dB. GMAP-TD clutter suppression is used in the radar. Also in the table, it can be seen that the standard and dual-polarization products are obtained from the D3R. Additionally, derived products listed in the table can also be generated and the moments are stored in the NetCDF file format.

Figure 2.1. The D3R system.

2.2. System architecture of the D3R

As D3R radar is a dual frequency radar and there are two main systems connected with each frequency band of the radar. A picture of the D3R radar on the trailer is shown in figure 2.1. From this figure it can be seen that the Ku and Ka band antennas are placed next to each other in a common positioner system mounted on a flatbed trailer; this is to achieve co-alignment and system synchronization between the Ku and Ka band radars. In the initial design for the D3R, a single aperture design for the antenna was considered, but this design was not implemented due budget and time constraints. The antenna system is composed of two dual linearly polarized prime focus parabolic reflector antennas that have well matched bandwidths. Four structs, each placed 90 degrees apart, hold the antenna feed in place. Waveguides are routed from the feed of the antenna system to the back of the reflectors. The reflectors are lightweight due to the composite material graphite, over honeycomb. To minimize wind loading and accumulation of precipitation particles, each antenna is covered with an A-sandwich type radome. Hydrophobic coating is applied to the radomes regularly to prevent a water layer forming on the radar which causes attenuation.

An aluminum frame is used to mount the antennas, this frame is designed to keep the angular deflections within $0.1°$ in any plane. The aluminum frame integrates both antennas, the RF transceivers, and IF analog/digital electronics onto the positioning system which minimizes front-end losses and simplifies the integration of the slip-ring assembly [1]. These elements comprise the rotating subsystem in the system architecture diagram shown in figure 2.2.

In the rotating subsystem, the transceiver and IF electronics are separate for both Ku and Ka. The analog/digital IF electronics house the arbitrary waveform generator and the digital receivers. The signal from the waveform generator is sent to the solid state transmitter. From there, it is sent to the switch to control the transmit and receive signals. This is because the same antenna is used for transmission and reception of the signal. The signal is then sent to the antenna which is radiated. The signal received at the antenna goes through the switch to the receivers and reaches the IF stage. The received signal is then packed as a timeseries signal at the IF stage and sent to the servers through the positioning system. The positioning system of D3R is equipped with two one-gigabit Ethernet connections. It is also equipped with a 20A, 208-240 VAC circuit which are used to communicate and transfer power to the rotating subsystems. The positioner system provides six differential signal pairs for timing, control and housekeeping. A GPS unit is also housed in the rotating subsystem which provides GPS signals for the radar.

The non-rotating subsystems shown in figure 2.2 comprise of one gigabit network switch, a RAID storage device, four servers, an uninterrupted power system (UPS), a dehydrator and

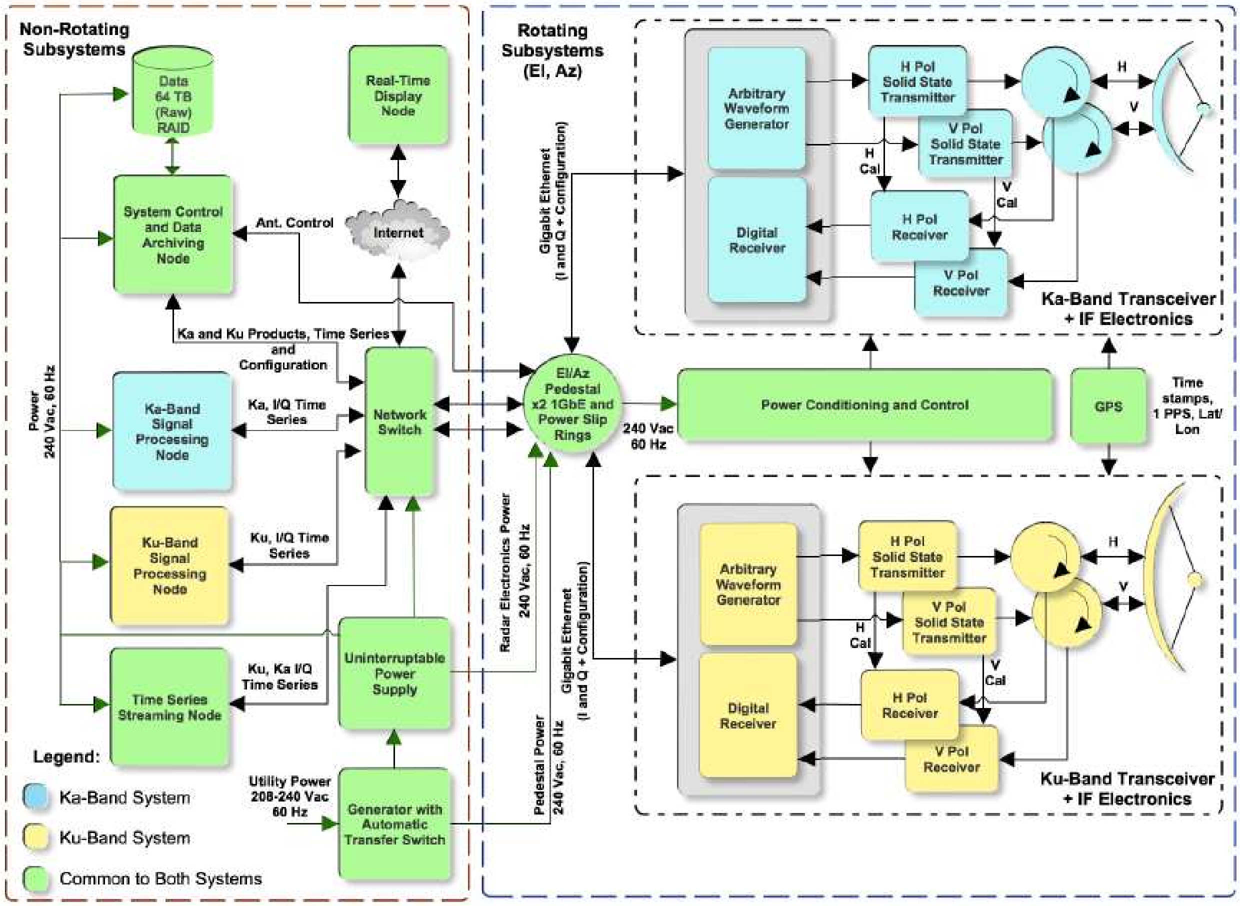

FIGURE 2.2. System architecture of the D3R [1].

a propane powered generator. All these subsystems except the propane powered generator are housed in temperature controlled enclosures which are located at the back of the trailer as shown in figure 2.1. The propane powered generator has a capacity to provide 14 kW and is located next to the antenna pedestal towards the front of the trailer as shown in figure 2.1. It has an automatic transfer switch which triggers the power control to the generator in case of a utility power failure. To prevent condensation, dry air from the dehydrator unit is cycled through the positioning system to all boxes in the rotating subsystem. The system control and data archiving block in the non-rotating subsystem handles the system control tasks such as on/off control, transmitter enable and antenna control. The timeseries I/Q data from the pedestal is routed to the signal processing and archiving nodes from the network switch. The time-series streaming server enables the processing and archiving of time-series data simultaneously without exceeding the slip-ring data transfer bandwidth. The signal processing node handles the moment generation and archiving of data products in real time. There are separate signal processing nodes for Ku and Ka band data. The real time output data is then available for display using a communication protocol defined for the VCHILL software [11]. In addition to this, any authorized user can have access to the real time data using an internet connection. The entire system is powered by a single 50 A, 208-240 VAC, 50-60 Hz circuit. The UPS and generator can ease the setup and testing of the radar when deployed on a field since they can function without utility power for a short time. The trailer is equipped with four outriggers with electric jacks which are used to level the trailer and provide stability during high wind conditions.

The D3R as mentioned before is a transportable system; when disassembling the radar for deployment in a different location, the rotating subsystem is disassembled with the help of a forklift. The antennas are not removed from the frame to make sure that the co-alignment does not change. The modules are stored in crates. The non-rotating systems are stable and fixed to the trailer, so there is no need to disassemble them. The trailer is then transported using a tow vehicle. At the assembly, all the modules are put together again with the help of a forklift. The setup or teardown process takes one or two days to be finished.

2.3. Software architecture of the D3R

The D3R software architecture is shown in figure 2.3. Dark gray boxes in the diagram represent hardware or firmware devices and the light gray boxes represent the software modules running on the general purpose servers. The Ethernet enabled power distribution unit (PDU) controls and powers all the hardware/firmware devices. In the event of a system

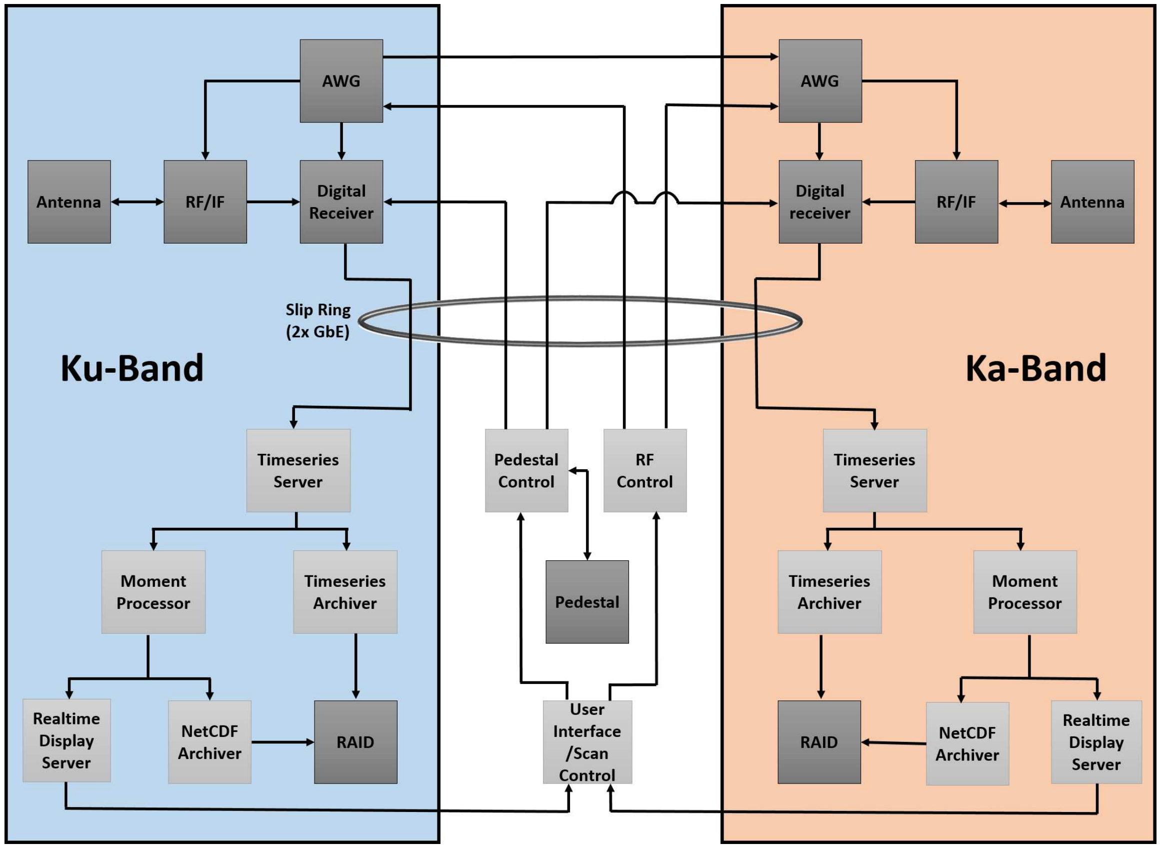

FIGURE 2.3. Software architecture of the D3R.

power issue, the PDU has the capability to perform a full remote recovery of the system. This is an added advantage of the D3R because it can control the radar remotely using an Internet connection. The antenna control is common for both Ku and Ka since they are mounted on a common frame. Antenna positioning is done by controlling the pedestal. By providing the scan parameters (start and stop azimuth, start and stop elevation, direction of movement and movement rate) the antenna pedestal can be configured for a required scan. The pedestal can also be queried to get the status and current position information. A serial communication interface is provided by the pedestal hardware for all communications, a serial to Ethernet adapter is used to allow pedestal to be controlled remotely for any networked computer. A sequence of scans can be programmed by executing a set of commands.

The RF control and data acquisition are separate for Ku and Ka bands. The local oscillators, arbitrary waveform generators (AWG) and digital receivers for both Ku and Ka band are housed in the IF box enclosure. The AWG is used to enable the RF control. AWG allows for timing and trigger generation, generation and configuration of the input waveform, phase control of the transmit waveform on a pulse by pulse basis, set the pulse repetition time (PRT). The AWG is also used to control the timing to generate the staggered mode sequence of transmitted pulses which have non-uniform PRT. The AWG is also used to enable or disable the transmit triggers. The Ka band trigger is operated as a slave with the Ku band trigger. By doing this, the synchronous operation of the system is achieved. The standard operational mode of the D3R is the Simultaneous Transmit And Receive (STAR) of both polarization channels with 400 μs/600 μs staggered PRT. For uniform PRT, the duration used is 500 μs. The D3R also operates in the alternate mode, which provides two more modes of operation.

The D3R's digital receivers are implemented using an FPGA based analog acquisition board hosted by a single board computer running on the Linux operating system. The digital receiver encodes the system status into the timeseries structure. Timeseries structure also contains information about the operating mode of the AWG, information about the PRT selection, polarization mode and version of the FPGA in the encoded form. The pedestal status and the information of azimuth and elevation are also encoded into the timeseries structure. This timeseries signal is then sent through the gigabit Ethernet connections for data processing. The Ku and Ka digital receivers have dedicated gigabit Ethernet connections. These gigabit lines are routed through the pedestal slip ring to the respective data processing servers. RF control and housekeeping functions which control and monitor the system share these gigabit connections.

Data processing is done on general purpose servers running Linux operating system. The gigabit Ethernet connections as mentioned earlier are used to share data between the digital receivers and processing servers. Having functional modules in the software divides the system operations divided into many servers. Specialized data processing software is used. The software used for data processing is divided into functional modules and network enabled interfaces for data transport. The timeseries data obtained from the digital receiver is sent to the timeseries archiver module from which the timeseries data is archived into the RAID module (Redundant array of inexpensive disks). The RAID is also used to provide fault tolerance.

The D3R moment processor detects the radar operation and generates various moments on a ray by ray basis. The radar and processing parameters used in the moment processor is fully customizable. They allows for online calibration, measurements of an internal RF source and measurements of the transmit powers via the transmitter calibration mechanisms. Once the moment is generated for a scan the moment files in the NetCDF format are sent to the NetCDf archiver from which they are stored in the RAID system.

The D3R uses a user computer to control the data software and the data stream through a network connection to the appropriate servers. A graphical user interface (GUI) or command line can be used to set and run the scans in the D3R. The system control and status information can be accessed using the GUI or command line. A complex scan sequence can be configured by stacking up multiple scans. The scan period field can be set to allow a time gap between the scan cycle. The real time display server provides us the real time telemetry information and radar moments. Though the flexibility of the real time display is limited for zooming and data filtering, it provides the radar operator a look at the radar observations in real time.

Chapter 3

Engineering description of the D3R upgrade

D3R was deployed successfully in many field campaigns and had collected extensive data. However, there were many rigid constraints that went into the initial radar design which limited the scope of research to an extent. The D3R radar had fixed frequencies with fixed filters. The disadvantage of this configuration is that the range resolution and sensitivity of the radar could not be improved. From a science perspective, high sensitivity and lower resolution will provide fine details of the weather events and engineers are working continuously to improve these factors in a radar. The waveforms used in the D3R for the short, medium and long pulses were fixed by the digital receiver. Modifications to the radar pulses were not possible in the old design. It is important to change the characteristics of pulses to improve the performance of the radar and to get quality data. The FPGA's used previously were at the maximum capacity, additional programming on the FPGA boards was not possible. Also, the previous hardware for the D3R was designed such that the transmit waveform generator was separated from the receiver.

Keeping the above-mentioned limitations in mind and to improve the performance of the radar which will open doors for more opportunities in research, D3R went through an upgrade from August 2016 to September 2017. The upgraded D3R is referred to as D3R 2.0. The goals of the upgrade was to improve the sensitivity, improve the range resolution and to have flexibility for programmable waveforms and filters. With a science point of view, the new D3R could aid the research using the high resolution data, up to five times improvement in the spatial resolution is available with the D3R 2.0. The sensitivity of the radar is improved by tuning the receiver bandwidth to up to 3 dB. The new waveforms which can be used in the D3R 2.0 will give an opportunity to enhance the polarimetric operation. The new waveforms will be useful for the characterization and mitigation of range-overlaid contamination of the signal. The transmitter waveform generator and the digital receiver are coupled so that we can make use of synchronous pulse-by-pulse change of transmit pulse and receive filters. Also, the new filters which are in the radar are much more capable of reducing the peak sidelobe level. The operations of CSU CHILL S-band radar has proven robust in the past years. Since it has a through design quantification, the upgraded design for the D3R is in common with the CSU CHILL S-band radar. Enhancements in one system will improve the other; this will provide more opportunities to improve signal processing and performance of the radars.

3.1. Hardware modifications and changes

The major changes in the hardware are in the arbitrary waveform generator and digital receiver along with the IF electronics associated with them, these blocks are a part of the rotating subsystems in the D3R architecture. Since D3R Ku and Ka band share the same design of these blocks with only scaling in frequency, the changes in the design and hardware are explained with respect to Ku band system. The transceiver system block diagram of the D3R Ku and Ka band is shown in figure 3.1. The highlighted sections in the blue are the modules which were redesigned and changed. The highlighted sections in the orange will be replaced by a digital module which has the functions of the arbitrary waveform generator and digital receiver.

A more detailed signal routing block diagram of these changed systems is shown in figure 3.2. In this figure, we can see the overall division of design and functionality in different sub-systems. These sub-systems were designed for Ku and Ka band (with different IF frequencies)

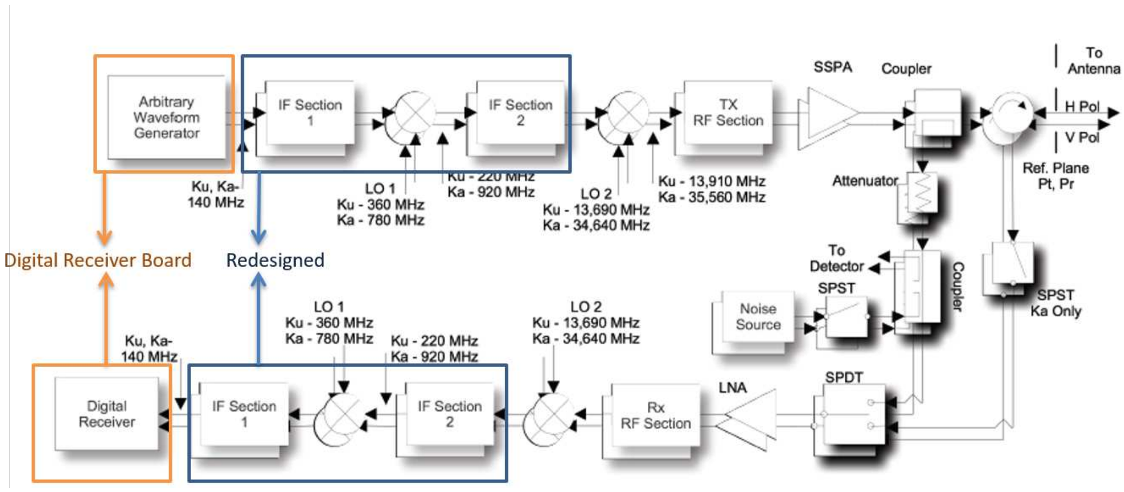

FIGURE 3.1. Transceiver block diagram with changed subsystems highlighted.

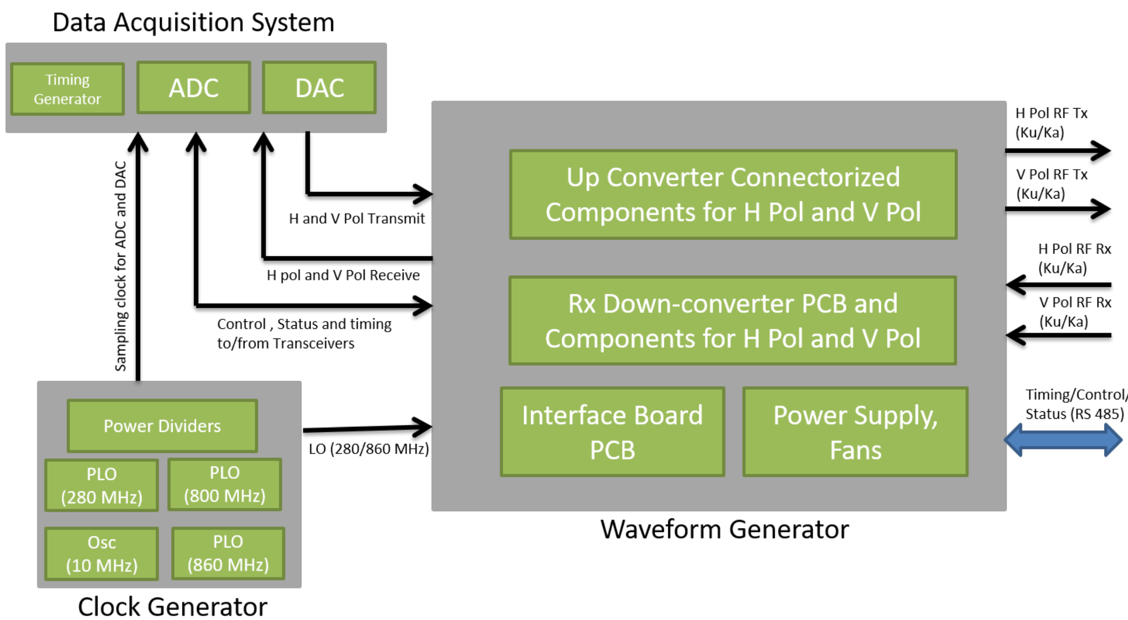

FIGURE 3.2. Redesigned blocks of IF stages of Ku/Ka transceivers.

[12]. The clock generation scheme and the IF up-converter and down-converter have been changed with respect to the previous system. In this figure, we can see the overall division of design and functionality in different sub-systems.

3.1.1. DESIGN OF DOWN-CONVERTER CHAIN. Gain and mixer stages are implemented to arrive at the 60 MHz IF which goes into the H-pol and V-pol channels in the digital module. For Ku band, the IF receiver chain starts with the 220 MHz band pass filter (BPF) with 50 MHZ as the 3 dB bandwidth this module is followed by an attenuator and then a blocking capacitor. The next module which follows is an amplifier. This amplifier is a flat gain, low noise amplifier with the frequency band of 200 $\pm$15 MHz, which is required. Next, a low pass filter (LPF) is used to reject the harmonics generated by the amplifier module. This signal is sent to the mixer module where the other input is the local oscillator (LO). Before the LO input is given to the mixer the signal is sent through attenuators and amplifiers, to achieve a gain of 10 dB. The mixer board layout and the realized broad is shown in figure 3.3. For the realization of boards, components were selected and procured and printed circuit board (PCB) layout was designed in-house. The components were integrated into the PCB at CSU using an infrared IC heater. Picture of a board being assembled is shown in figure 3.4.

The mixer output is given as an input to the amplifier, which has built-in stabilization network. The line widths in the PCB are in accordance with controlled impedance requirements. The power consumption of the amplifier is 0.35 W and can tolerate a temperature rise of 8°C. The inter-modulation products at 220 MHz and 280 MHz are suppressed by filters in the amplifier board and anti-aliasing filter (which is a connectorized component). With an overall gain of 18 dB after the mixer, the final power levels for these inter-modulation products are -168 dBc and -150 dBc respectively. The 1dB compression point of the amplifier makes sure that the ADC is not damaged in the long run with high power from near ranges or ground clutter. The amplifier board layout and the realized broad is shown in figure 3.5.

For designing the boards, the LO and RF paths are made symmetric. To minimize emissions, line lengths are made small compared to the wavelength. The trace widths are computed based on the layer stack-up and dielectric constant of the substrate. The layer

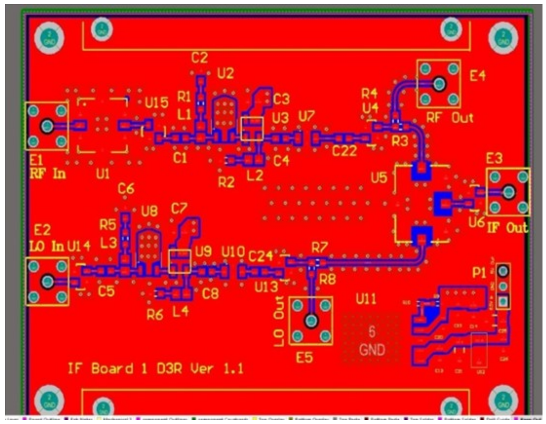

(A) Mixer board layout.

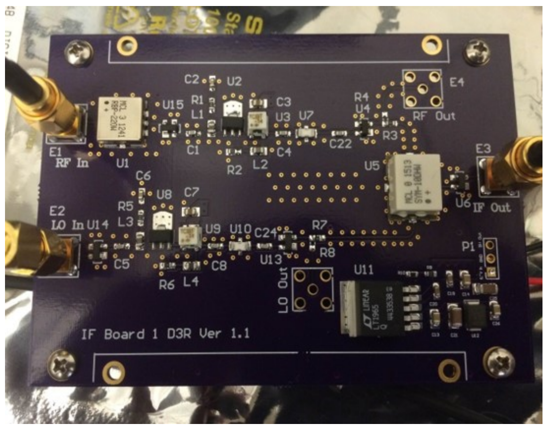

(B) Realized mixer board.

FIGURE 3.3. Mixer board layout and realization.

stackup is the four-layer prototype. The whole of the top and bottom layers are ground planes with split islands for power. This is done to minimize the loop currents.

3.1.2. DESIGN OF UP-CONVERTER CHAIN. The digital module along with the DAC interface has the capability to generate a range of frequencies which has reasonable sampling rates. This enables the digital in-phase and quadrature (I/Q) samples to be interfaced from FPGA to DAC and allows for feasible filter design. To meet the dynamic range requirements, simulation of the mixer products and the rejection required were done which in turn helped to design the IF stages and the analog bandwidth required at these IF stages. The main challenge in the design was to remove the local oscillator (LO) feedthrough, which is

Figure 3.4. Integration of components on to PCB using infrared IC heater.

a high power spurious component by trading off with other intermodulation power levels. The analog bandwidth was narrowed down to get the adequate rejection of LO feedthrough and other mixer products. With these simulations of the mixer products and calculating the amount of gain requires at the IF sections, the up-converter design for the Ku and Ka band was accomplished.

The LO generation components were segregated to a single module called clock box and the IF up-converter stages to the waveform box. The power requirements for the LO to drive the mixer was + 17 dBm; this was partially satisfied at the clock box and partially at the waveform box level. The new design met the requirements of power to drive the transceiver inputs. Also, good spectral purity of the signals was achieved using adequate filtering stages. The filter requirements were determined based on the simulations of mixer products and the

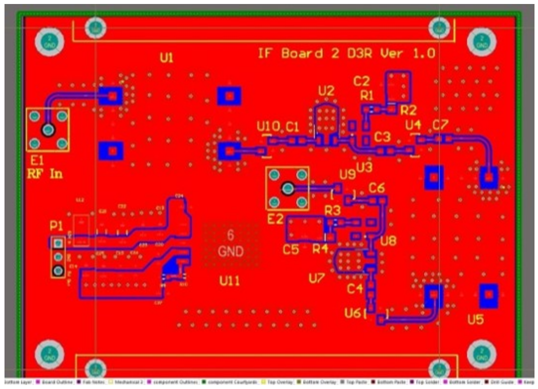

(A) Amplifier board layout.

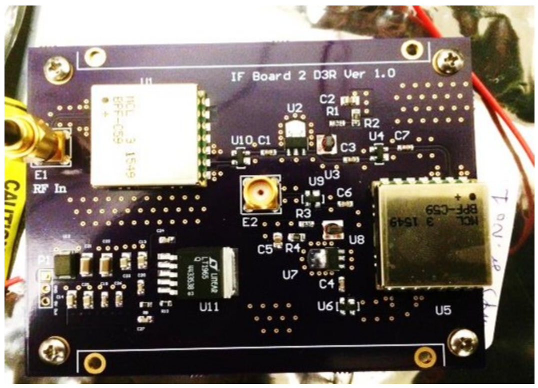

(B) Realized amplifier board.

FIGURE 3.5. Amplifier board layout and realization.

LO leakage. The filter design was more stringent for up-converter stages than the receive because the operating power at each stage is high and most of the components operate in the 3 dB compression level in the transmit chain.

3.1.3. DESIGN OF INTERFACE BOARD. The interface board converts the signal from low-voltage differential signalling (LVDS) to RS485. The board drives nine pairs of the RS485 signals. This board also takes in nine inputs from the transceivers and converts them to the LVDS signal before sending it to the digital receiver. For RS485 lines which traverses long distances, transient suppressors are added. The coaxial inputs signal to this board are the 1 pps and synchronization (sync) signal and the coaxial output signal is the sync out. The sync signals are used to maintain synchronization between the Ku and Ka band systems.

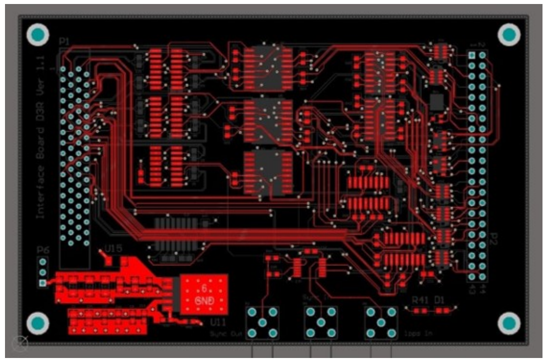

(A) Interface board layout.

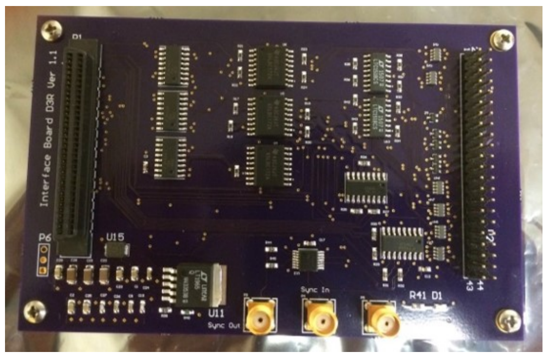

(B) Realized interface board.

FIGURE 3.6. Interface board layout and realization.

Power dissipated by the linear regulator on this board is 0.215W. DD package is used for the linear regulator; hence the thermal resistance will be in the range of 25C/W to 35C/W depending on the copper area. Thus the junction temperature rise above ambient would be 0.215W 30C/W = 6.45C. The interface board layout and the realized board are shown in figure 3.6.

3.1.4. DESIGN OF CLOCK BOX. The IF frequency plan was accomplished after many simulations were done and also depending on the availability of the synthesizer modules at the particular frequencies. To meet the required levels of both the up-converter chain and down-converter chain, appropriate amplification and attenuation stages were added. The block diagram of the synthesis of different frequencies at the IF stage is shown in figure 3.7. All these components reside in clock box. The realized clock box is shown in figure 3.8.

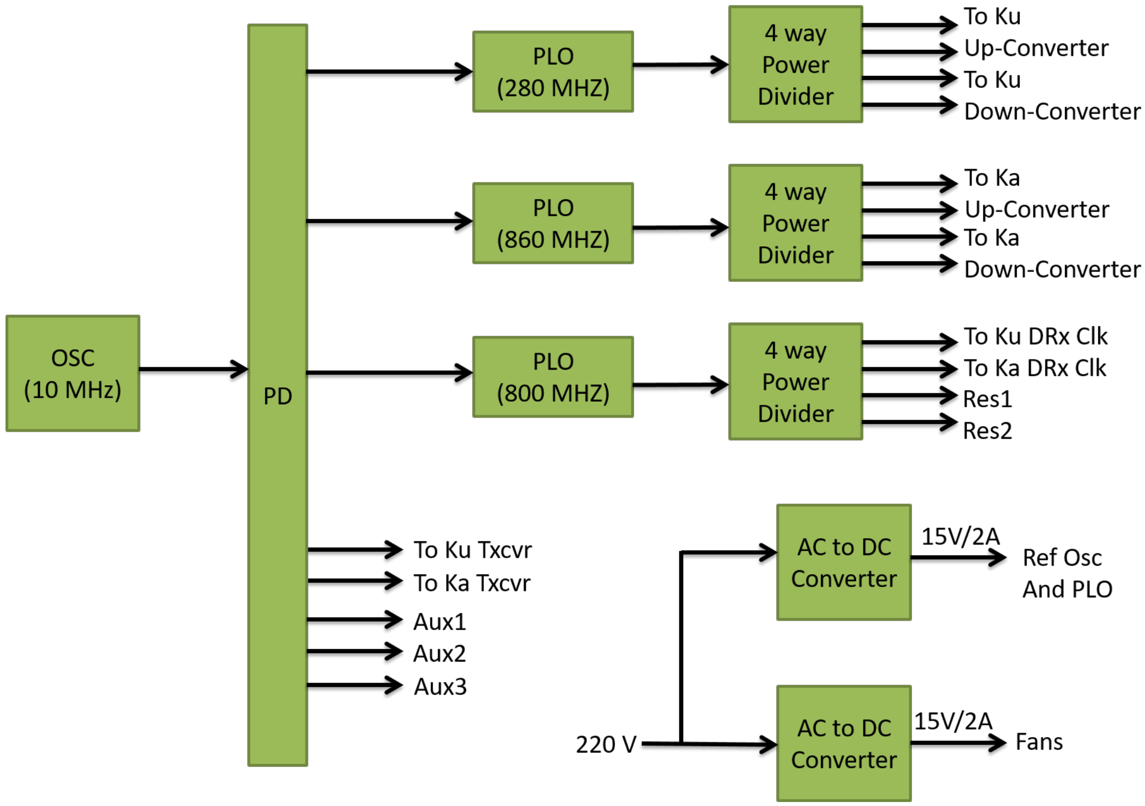

FIGURE 3.7. Block diagram showing synthesis of different IF frequencies and clock signals.

FIGURE 3.8. Realized clock box.

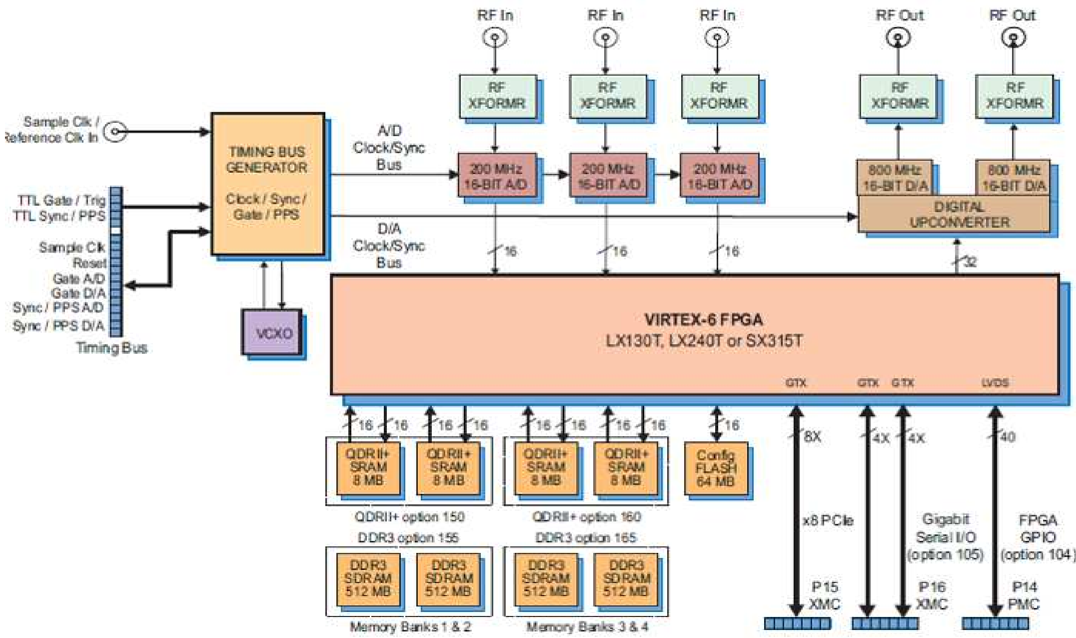

FIGURE 3.9. FPGA module on a single board computer [2].

3.1.5. IMPLEMENTATION ON DIGITAL RECEIVER FPGA. Both the IF waveform generator and the digital receive sections have been packaged into a high-speed digital module, based on Virtex 6 Field Programmable Gate Arrays (FPGA) [13]. This module includes three 200MHz, 16bit ADC's, two 800 MHz DAC's and four banks of memory [2]. A more detailed architecture of this module is given in figure 3.9. The ADC's and DAC's in this module have a high spurious free dynamic range (SFDR) (> 90 dBc), so as to enable sampling of intense storms to light cloud and snow observations. If the receive gain is tailored to toggle the lowest bit of the ADC converter the system's sensitivity can be improved. This is because the noise will be contained in the lowest bits. This is one of the advantages of having a high dynamic range. However, if the SFDR is not good, then an additional spurious signal may be detected along with the weather echoes. These spurious signals may be due to the inter-modulation products of the mixer, aliasing, improper filtering and also due to the non-linearities in the ADC itself.

Figure 3.10. Digital receiver chassis which houses the arbitrary waveform generator and the digital receiver.

3.2. Software modification and changes

Software modifications and changes for the D3R was done with a plan to keep minimum change in the overall software architecture and maintain the hierarchy. Since we use arbitrary waveform generator and digital receiver which is in common with CSU S-band radar, the software for these modules is already designed and developed by the engineers at CSU. It is a specialized software of CSU, which undergoes regular updates. This software is proven robust and dependable as it is operational in the CSU CHILL radars without any glitches in the past. An added software feature in one system will aid the other system; this is the advantage of having common software between the two systems. This software has control and flexibility for timing control, waveform generation and adjusting different system parameters on the go.

The D3R 2.0 employs frequency diversity waveform consisting of two frequency spaced subpulses, $1\mu s$ and $20\mu s$. The long pulse which was used in the initial design of the D3R is omitted. The modified software architecture is shown in figure 3.11. The output from the digital receiver is a custom format timeseries packet, which consists of timeseries data and the associated header. The header structure and the timeseries data packing in the timeseries packet were different compared to the previous D3R timeseries packet. A converter software

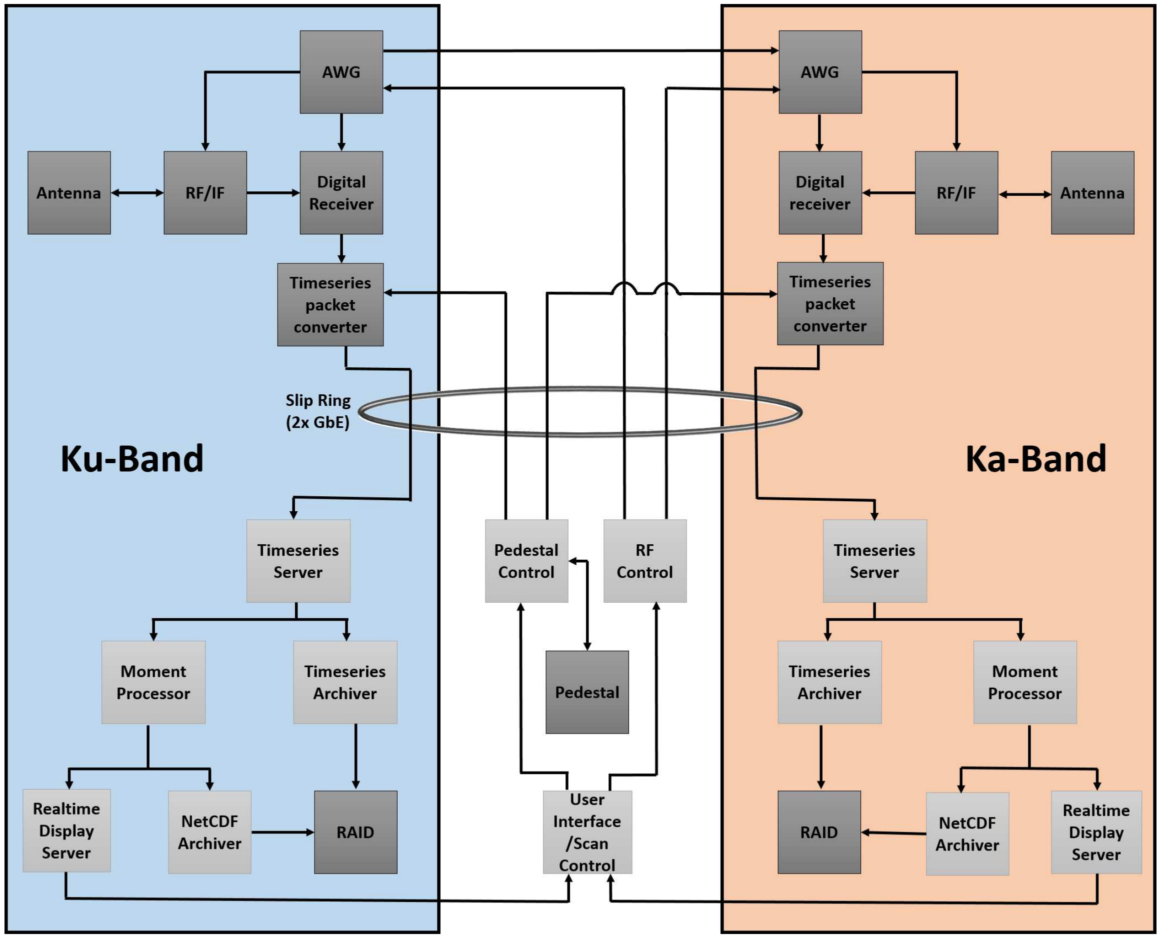

FIGURE 3.11. New software architecture of D3R.

module was designed and implemented after we get the output from the digital receiver as seen in the new architecture. The GPS signals and the antenna position signals were captured and packed into the timeseries header. This made the software in the servers compatible with the data from the new digital receiver. Modifications in the moment processor were done to accommodate new signal processing features for the upgrade.

The overall software was modified to handle the 30 meter range resolution which is a new feature of D3R 2.0. The firmware part of the software is unchanged which can handle the 30 m data by packing more data on to the timeseries packet. The data packet size increases by five times to accommodate high resolution (30 m) data. The timeseries archiver, moment processor and NetCDF archiver were modified accordingly to handle the 30 m resolution data.

3.3. Design aspects of the upgrade

Various design aspects for the D3R upgrade is discussed in this section. For designing the IF stages with the mixer, the spurious response of the mixer and rejections of the filters were checked and designed accordingly. The form factors for existing sub-systems were preserved but modified internally; this was done so that there are minimal changes in cabling and power supply.

3.3.1. Mechanical aspects.

To protect the electronics which are mounted on the IF boards, shielding enclosures were selected. The enclosures are basically 3in width, 5in length and 2in height boxes. They were designed with mounting bars and bulkhead panel mount SMA connectors with allowance for internal cabling. The boxes were modeled prior to manufacture. The models and the enclosures are shown in figure 3.12.

These smaller boxes along with the filters, interface board and power supply are placed in a bigger enclosure. Cabling and routing for this enclosure are done considering the shortest and efficient path. All the connectors are in the front. Eight fans are present in the box which regulates the temperature inside the box. Temperature testing was done to see the minimum and peak temperatures of the heat dissipated by the whole enclosure by placing it in a bigger box replicating the IF box on the radar. After the box reached a certain threshold temperature, the power supply was switched off. The performance was studied during this test. Figure 3.13 shows the Ku electronics housed inside the bigger enclosure and figure 3.14 shows the Ka electronics housed inside the bigger enclosure. From the figures, we can see that the component placement is done effectively considering air flow and cabling.

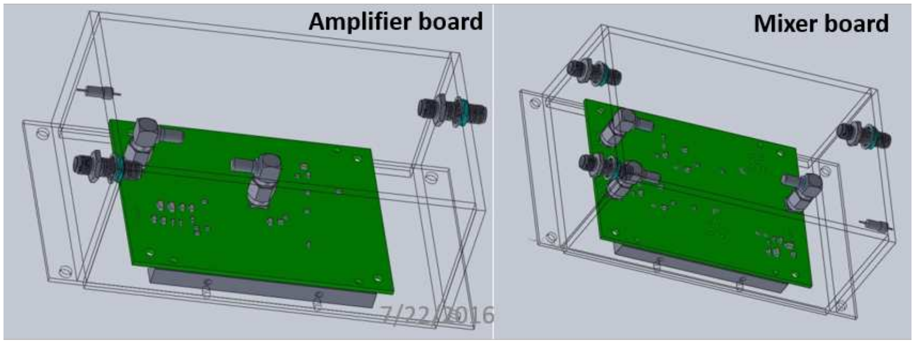

(A) Models of enclosures.

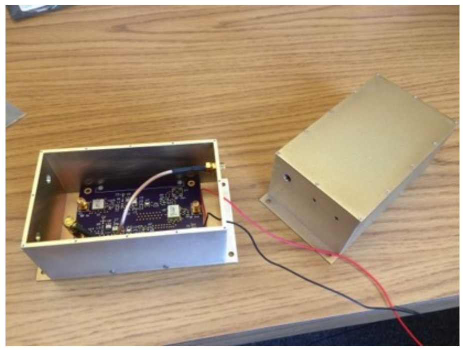

(B) IF boards placed inside enclosures.

FIGURE 3.12. Shield enclosures for RF boards.

FIGURE 3.13. Realized Ku IF design.

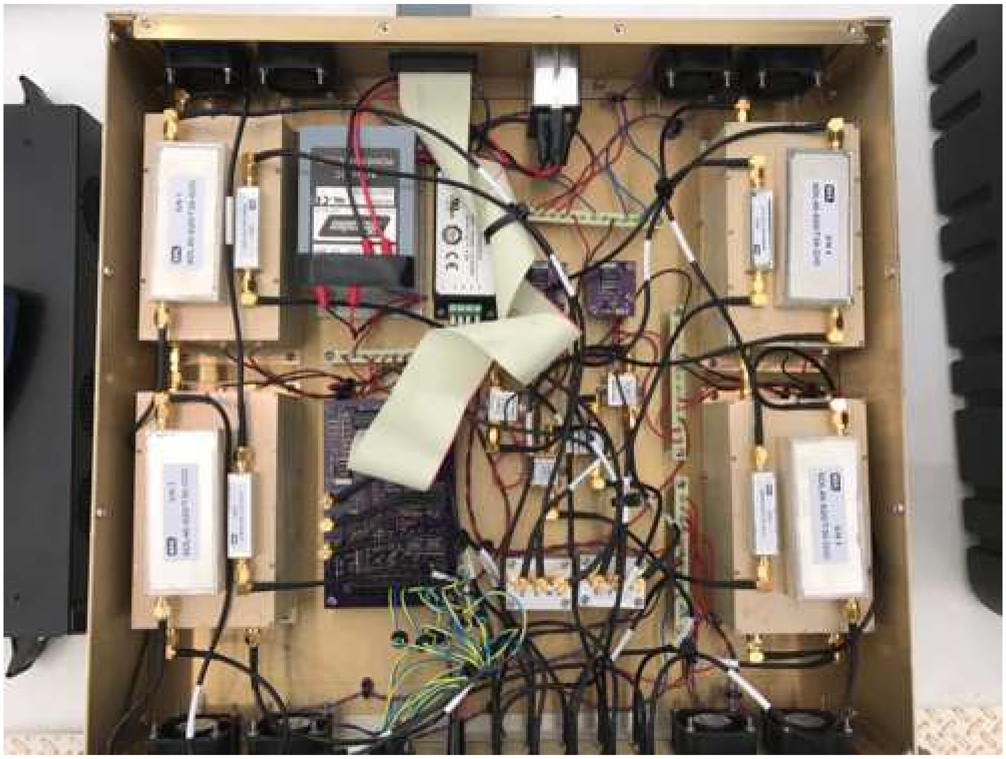

FIGURE 3.14. Realized Ka IF design.

3.3.2. WAVEFORM DESIGN. Frequency modulation (FM) scheme of radar will decide the level of sidelobes in the signal. Researchers have put in great amount of effort to design the best frequency modulation scheme. The figure shows the frequency profile of linear and non-linear frequency modulation schemes. The linear FM is a linear sweep in the frequency domain with time and amplitude windows are used to reduce the sidelobe power. The same effect can be achieved with non-linear FM at the beginning and end of the sweep. In D3R we have used linear FM and used the criterion of minimization of integrated sidelobe level (ISL) energy instead of peak sidelobe minimization as used in hard targets. Since the minimum ISL filter is designed to minimize the total energy in the sidelobes it has a much lower sidelobe compared to window functions. ISL filter also has a lower finite bandwidth loss factor compared to a window based mismatched filter. We use additional non zero coefficients to bring down the sidelobe energy.

Figure 3.15 (A) shows the results of simulation of linear FM based pulse compression system using minimum ISL and a matched filter. For the simulation bandwidth of 5 MHz and time duration of 20 μs is used. From the figure, we can see that the sidelobe level of the matched filter is much higher than the ISL counterpart. The ISL filter has much wider impulse response than the matched filter due to the use of additional non zero coefficients (ANZC). Broadening of the mainlobe of the ISL filter leads to coarser resolution. This can be traded off with the sidelobe power. The figure 3.15 (B) shows the trade-off between the ANZC's and the sidelobe power. From the figure, we can see that the higher the ANZC's lower is the peak sidelobe power but longer number of samples. Having a large number of ANZC's will amount to large filter lengths which comes at a hardware expense. But using a large number of ANZC's will affect the weather returns at farther ranges because of the large lengths of these filter lengths. This makes it difficult for the engineers to achieve optimal side lobe performance at all range gates. A better strategy is to have all constraints embedded in an adaptive filter to derive a least square formulation of the problem, which might be implemented in the future. This will have the advantage of shaping the sidelobe energy to gain high sensitivity in intense reflectivity gradients.

3.3.3. Sensitivity. Sensitivity is an important specification for any radar. Sensitivity is the ability of the radar to detect weak precipitation echoes as well as intense precipitation echoes. It is mostly linked with the ability of the radar to detect weak precipitation echoes with the system noise as the limiting factor. In the weather radar system, the final bandlimiting of noise is performed by the pulse compression filters and hence their frequency characteristics are quite important for the sensitivity point of view. Figure 3.16 shows the frequency characteristics of a 5 MHz pulse compression filter synthesized. So not only the time domain characteristics of sidelobe performance are important, but also the frequency

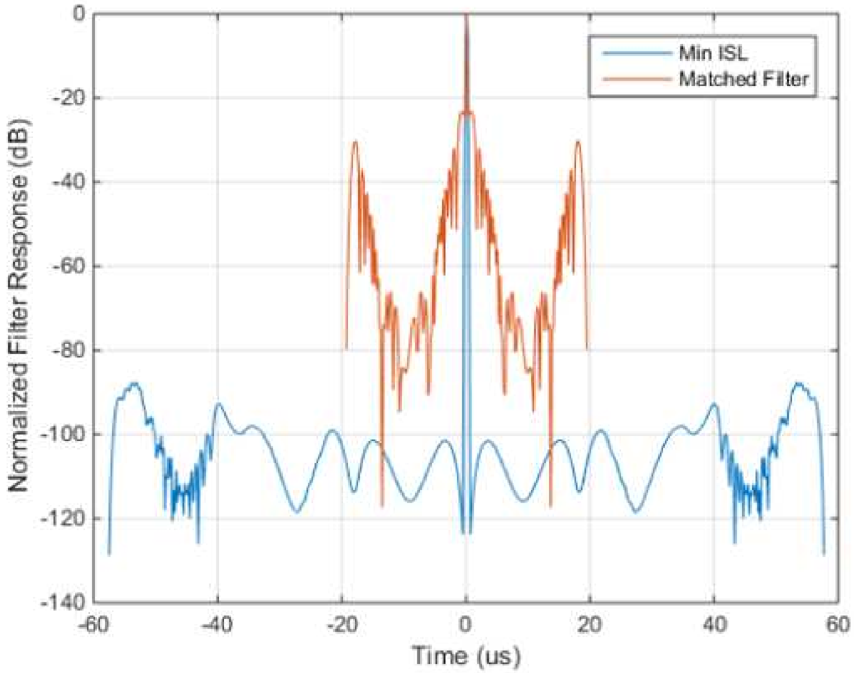

(A) Matched and Mis-matched LFM Filter Response.

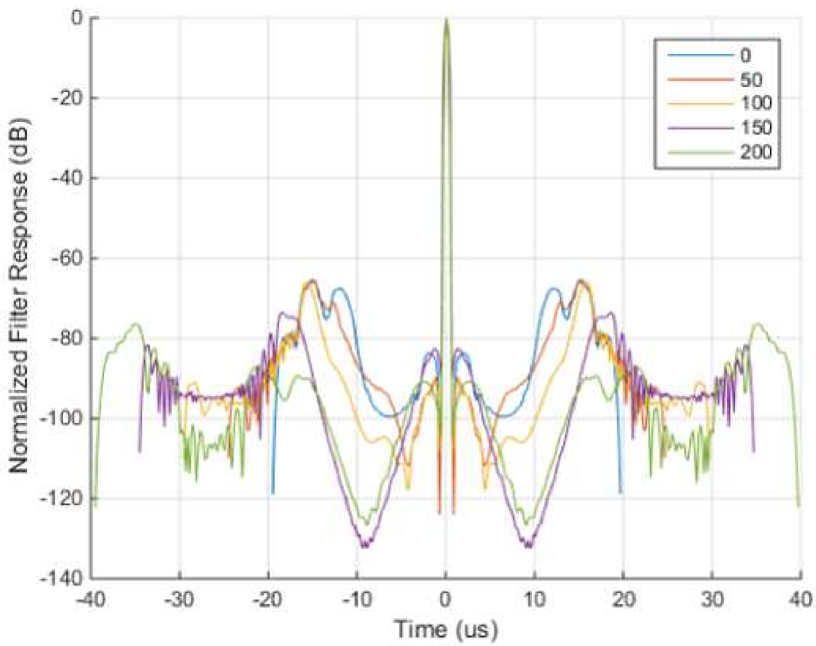

(B) Sidelobe performance for different ANZCs percentage.

FIGURE 3.15. Results of simulation of LFM based pulse compression system

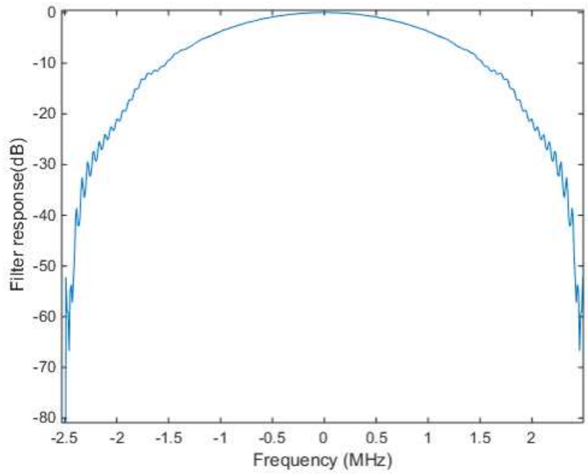

FIGURE 3.16. Pulse compression filter frequency response. System parameters: B = 5 MHz, T_S = 5 MHz and T = 20 μs

characteristics of these filters are important for sensitivity analysis. As we open up higher bandwidth, the noise power will be increased. Wideband pulse compression filters will give better range resolution but can reduce the system sensitivity performance due to increased noise power [14]. We compute the curve of minimum detectable reflectivity by computing the noise power at the output of these compression filters. Typically, a single pulse sensitivity is plotted. Sensitivity for a radar is usually defined in terms of reflectivity. The Reflectivity can be computed from received power P_0 as

$$Z_e = CR^2P_0 \tag{16}$$

Where C is the radar constant and R is the range. The minimum detectable reflectivity as a function of range is computed by setting the received power equal to the noise power i.e., signal to noise ratio (SNR) is unity. The noise power is computed by considering the noise from the antenna, low noise amplifiers and the gain of the receive system. The minimum detectable reflectivity in logarithmic scale is given as

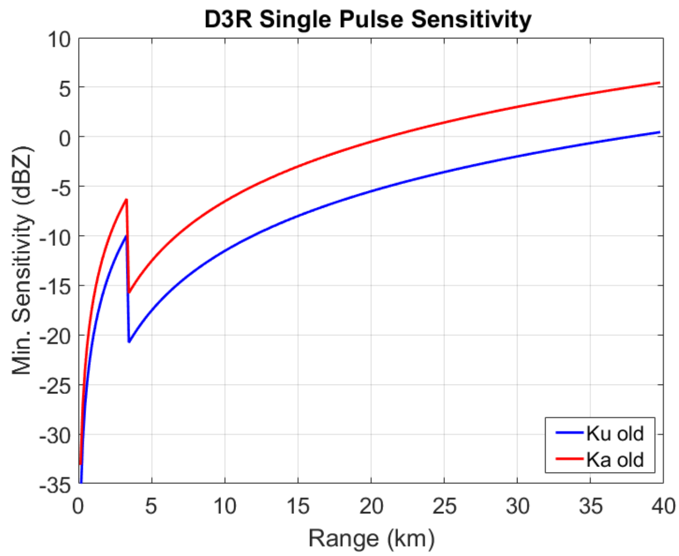

(A) B = 3.6 MHz and resolution = 150 m.

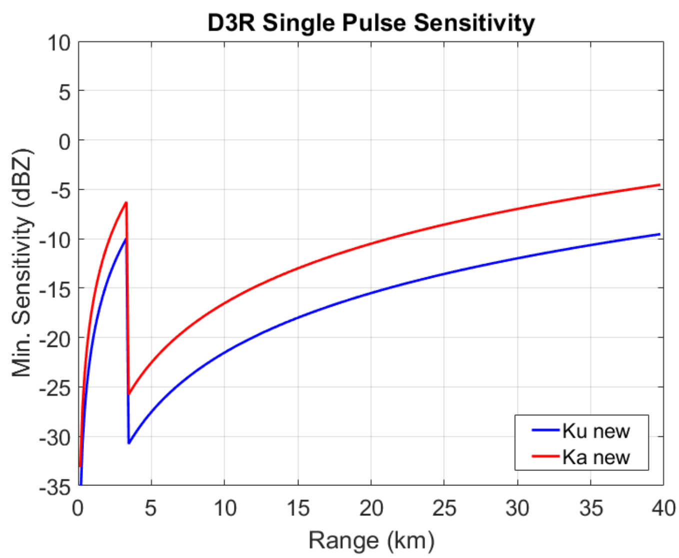

(B) B = 1 MHz and resolution = 150 m.

FIGURE 3.17. Sensitivity curves of D3R

$$min(Z_e) = 10log_{10}(kTB) + C + 20log_{10}(R) \tag{17}$$

Where k is the Boltzmann constant, T is the noise temperature and B is the bandwidth. The curve of the minimum detectable reflectivity is plotted as a function of range and mean noise power. The sensitivity curves for the previous system and the new system is shown in figure 3.17. The plots in the figure have a short pulse sensitivity curve till 3.8 km; then the medium pulse sensitivity curve takes over. This explains the jump in the sensitivity curve at 3.8 km in range. Comparing 3.17 (A) and 3.17 (B) it can be seen that for Ku at 15 km distance, the old system has a sensitivity around -8 dBZ and the new system has a sensitivity around -18 dBZ. The sensitivity has an improvement in the new system. It should be noted that there are other factors which affect the overall sensitivity if the system. Sensitivity degrades with higher bandwidth, but higher bandwidth enables higher baseband data rate which will in turn improve the resolution. There is always a trade-off between the range resolution and sensitivity of the radar.

D3R 2.0 will have the capability to handle new phase coded waveforms. In the previous system, only random phase coding scheme was present. In D3R 2.0 systematic phase codes which perform better than the random phase codes will be implemented. These coding schemes will be incorporated in the new waveform sections of the upgraded hardware. Also in the simultaneous transmit and receive mode of operation (STAR), coding of horizontal and vertical polarization transmit pulse with orthogonal codes lead to better cross-pol measurements.

3.4. Testing and integration of D3R 2.0

The upgrade for D3R was done in two stages. The Ku IF stages, digital receiver and software was upgraded in the first phase and then the Ka IF stages, digital receiver and software were upgraded in the second phase. the preliminary design review (PDR) was done in early 2016, in which various design features and options were discussed. The critical design review (CDR) was held in mid-July 2016, where the various design features and time-frame

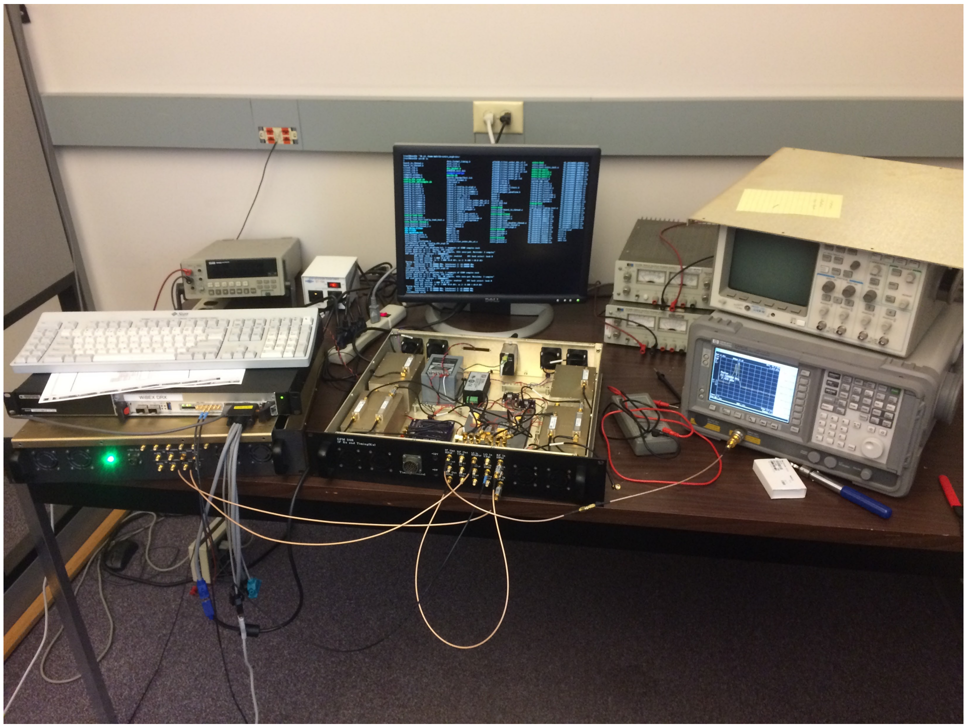

FIGURE 3.18. Test setup at CSU.

of the upgrade were critically examined. In the CDR meeting, various simulations results were discussed. The Ku IF stages were built and the digital module was configured from mid-July 2016 to mid-October 2016. A test setup was done at CSU to test and measure the signals at the IF box. The test setup for one of the boxes is shown in figure 3.18 Modifications for mechanical block enclosures of the IF box was done at the CSU CHILL radar facility.

In the last two weeks of October 2016, the designed IF boxes and the digital module was taken to Goddard Space Flight Center (GSFC) in Maryland for bench testing. The setup for bench testing is shown in figure 3.19. During this time the transceivers from the radar were integrated with the designed boxes to see the performance of the system. Various timing adjustments and signal levels were checked to ensure the integrity of signals from one stage to the next. The Ku IF boxes and the digital module were integrated to the radar during the end of November 2016 at Wallops Flight Facility (WFF). The radar trailer was bought indoors, various field tests were conducted and the new boxes designed were integrated onto

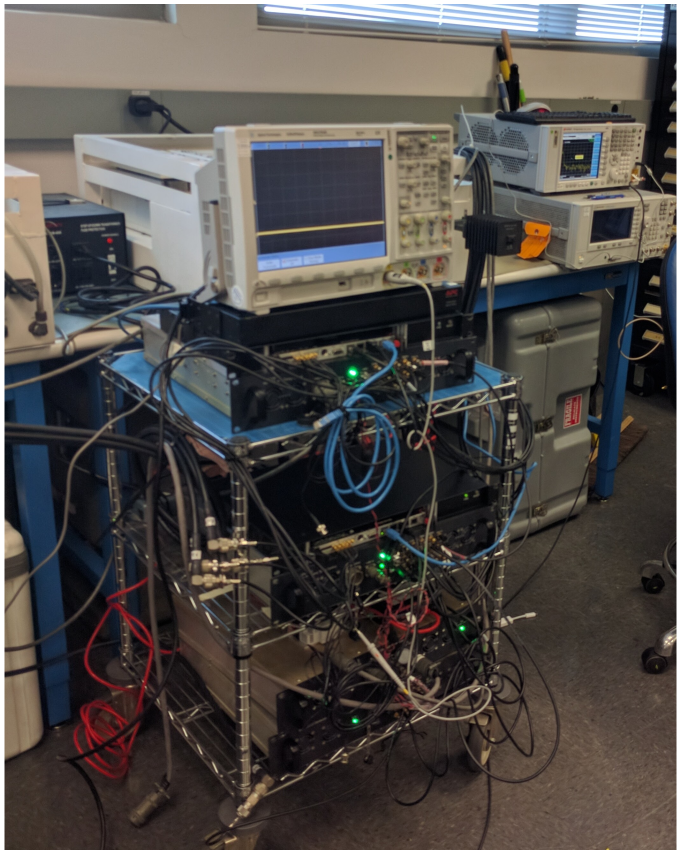

FIGURE 3.19. Test setup at GSFC for bench testing.

the radar. At the end of this integration, the radar was operational with the new Ku band system and old Ka band system. This allowed us to quantify and see the performance of the newly designed boxes with reference to the old Ka design.

Parameters of the Ku band system were tweaked in the software to achieve optimal results. In parallel, the design of Ka band IF stages and configuration of Ka band digital module was done from January 2017 to April 2017. Integration of the Ka band modules on to the radar was accomplished in mid-May 2017. Pictures from the radar hardware integration in WFF is shown in figure 3.20. This completed the hardware integration of the upgraded D3R. The system parameters were monitored and adjusted in June and July of 2017. Tower calibration exercise was one in August 2017 for verifying reflectivity against radar cross section (corner reflector was used). The radar was packed and shipped for the

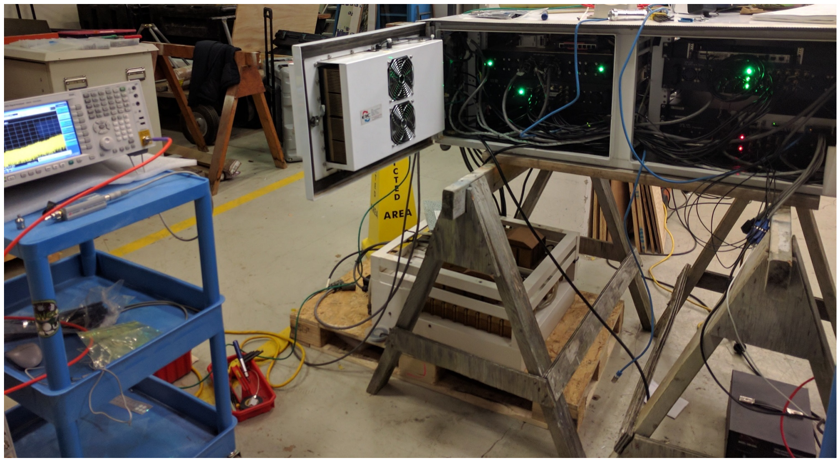

(A) IF and digital module integration and testing.

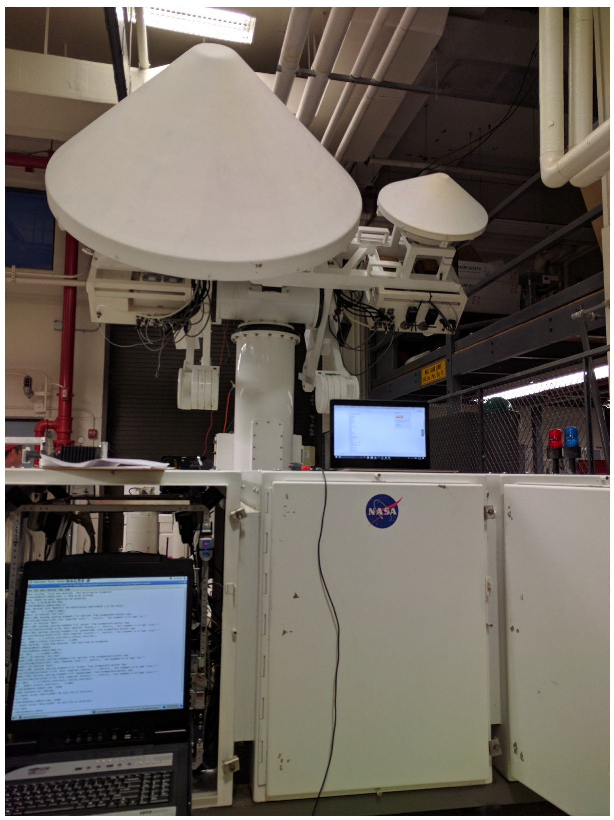

(B) Radar at an indoor location where integration was done.

Figure 3.20. New hardware integration at WFF.

first deployment after upgrade in September 2017. With D3R 2.0 having the features of high resolution, reconfigurable waveform design and filters makes it an agile research platform to study microphysics.

3.4.1. Signal level and timing measurement results.

Signals levels should be measured so that we can ensure the proper signal level is being generated by the system. Managing the timing of the system such as transmit time and receive time should be taken care accurately to achieve the desired performance from the radar. Getting the expected output in signal levels and timing ensures that all the subsystems are working as expected. In this subsection, the signal levels and timing measurements are discussed for Ku band system. A similar analysis was carried out for the Ka system.

Figure 3.21 shows the spectrum analyzer output for 10 MHz which is input to the Ku transceiver. From the figure, we can see that the center frequency is at 10 MHz with a signal level of 2.2 dBm. Figure 3.22 shows the H-Pol RF measurements for the short and medium pulses. In the measurements, the test cable loss of +1.2 dB should be considered. In figure 3.22 (A) we can see that the signal level of short pulse is -12.935 dBm and in figure 3.22 (B) we can see that the signal level of the medium pulse is -13.434 dBm which are in the desired levels.

Figure 3.23 shows the timing measurements of the short and medium pulses. In figure 3.23 (A) we can see that the short pulse spans about 1 μs and in figure 3.23 (B) the medium pulse spans about 20 μs, these verify that the output of the system is achieved with designed timings. Figure 3.24 shows the uniform PRT and staggered PRT sequence for pulse transmission from the D3R 2.0. From the figures, we can see that the uniform PRT of $500\mu s$ and staggered PRT with $T_1 = 400\mu s$ and $T_2 = 600\mu s$ is obtained correctly.

3.5. Acknowledgment for upgrade of D3R

Hardware designs and changes for D3R explained in this chapter was done along with Mohit Kumar, Manuel Vega and V. Chandrasekar.

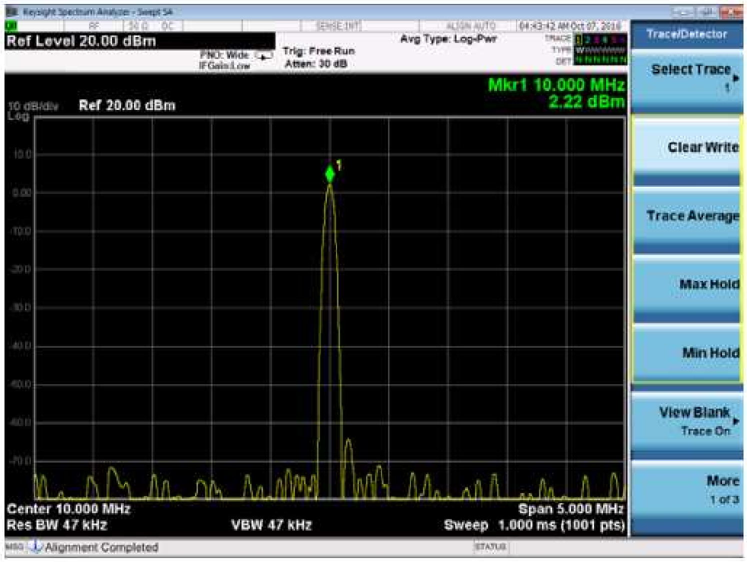

FIGURE 3.21. 10 MHz input to Ku transceiver.

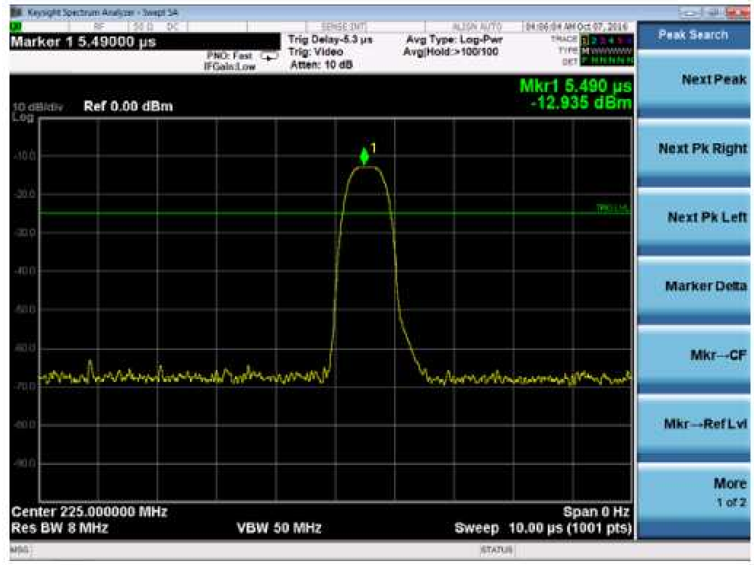

(A) H-Pol RF output short pulse (+1.2 dB test cable loss).

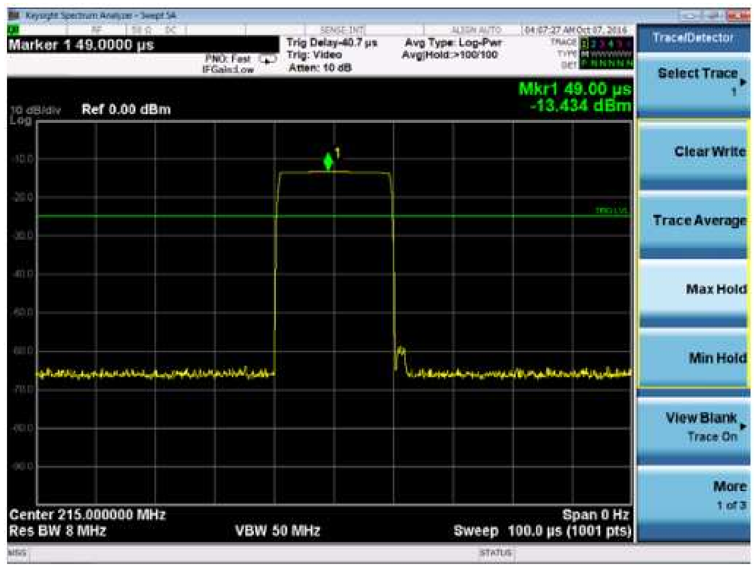

(B) H-Pol RF output medium pulse (+1.2 dB test cable loss).

Figure 3.22. H-Pol RF measurements for short and medium pulses.

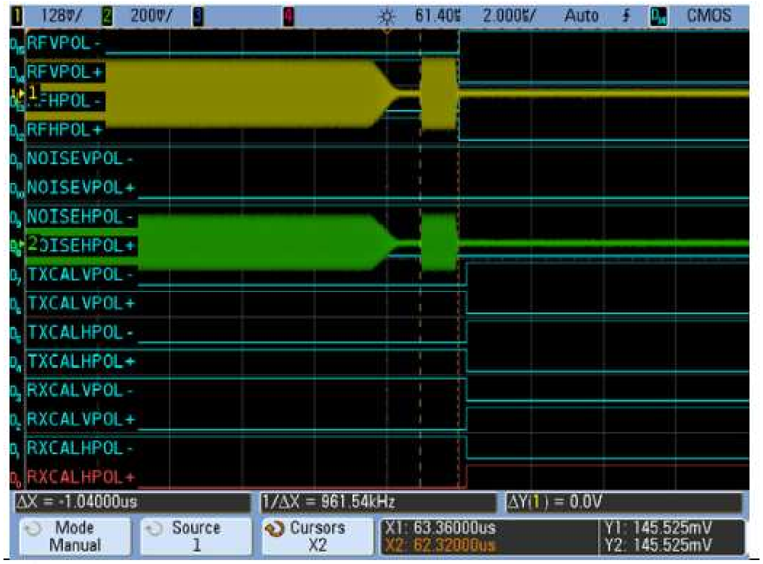

(A) Short pulse time period.

(B) Medium pulse time period.

FIGURE 3.23. Timing measurements for short and medium pulses.

(A) Uniform PRT sequence with $T = 500\mu s$.

(B) Staggered PRT sequence with $T_1 = 400\mu s$ and $T_2 = 600\mu s$.

FIGURE 3.24. Uniform and staggered PRT sequence timing measurement.

Chapter 4

Range and velocity ambiguity mitigation for D3R

4.1. Background Theory

4.1.1. Introduction to range-velocity ambiguity.

Range and velocity are two key moment variables in any meteorological radar. The maximum unambiguous range (r_a) and the maximum unambiguous velocity (v_a) of any pulsed Doppler radar is limited by the systems pulse repetition frequency (PRF). The pulse repetition time (PRT) and PRF are related as

$$PRT = \frac{1}{PRF} \tag{18}$$

Pulsed Doppler radars having a PRT of T, will have a maximum unambiguous range given by [3]

$$r_a = \frac{cT}{2} \tag{19}$$

where c is the velocity of light. It can be seen from this equation that the r_a and T are directly proportional to each other. The maximum unambiguous velocity is given by

$$v_a = \frac{\lambda}{4T} \tag{20}$$

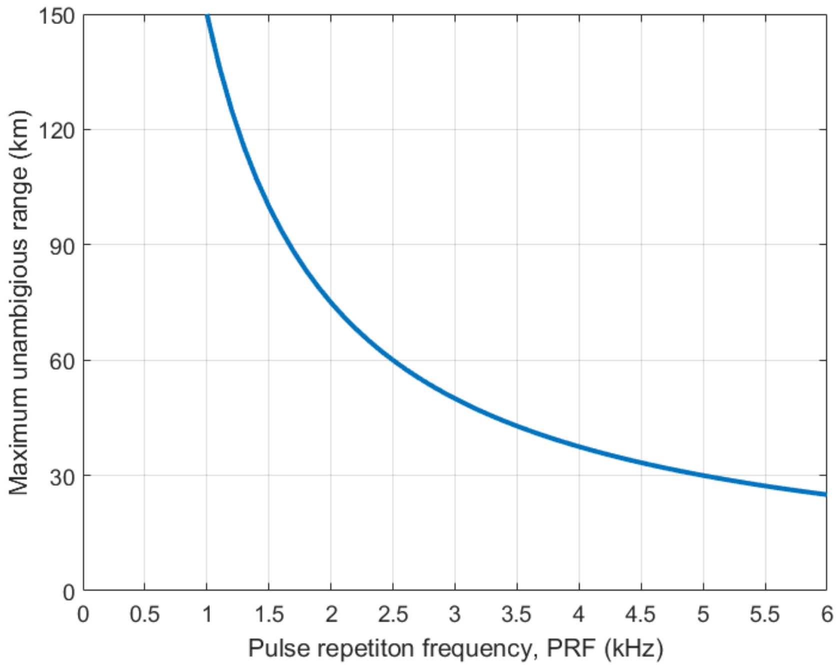

FIGURE 4.1. Illustration of range limitation with increasing the pulse repetition frequency.

Where λ is the wavelength which is related to the frequency of the radar (f) as $\lambda = \frac{c}{f}$. It can be seen from this equation that the v_a and T are inversely proportional to each other. As both r_a and v_a are dependent on T, the relation between them is given by [15]

$$r_a v_a = \frac{c\lambda}{8} \tag{21}$$

From this equation, we can see that there is a limitation between the maximum unambiguous range and maximum unambiguous velocity and is dependent on the wavelength at which the radar system is operating. For Doppler radars transmitting uniformly spaced pulses, it is known that there is coupling between the maximum unambiguous range and maximum unambiguous velocity; r_a or v_a can only be increased at the cost of a proportional decrease in the other [16].

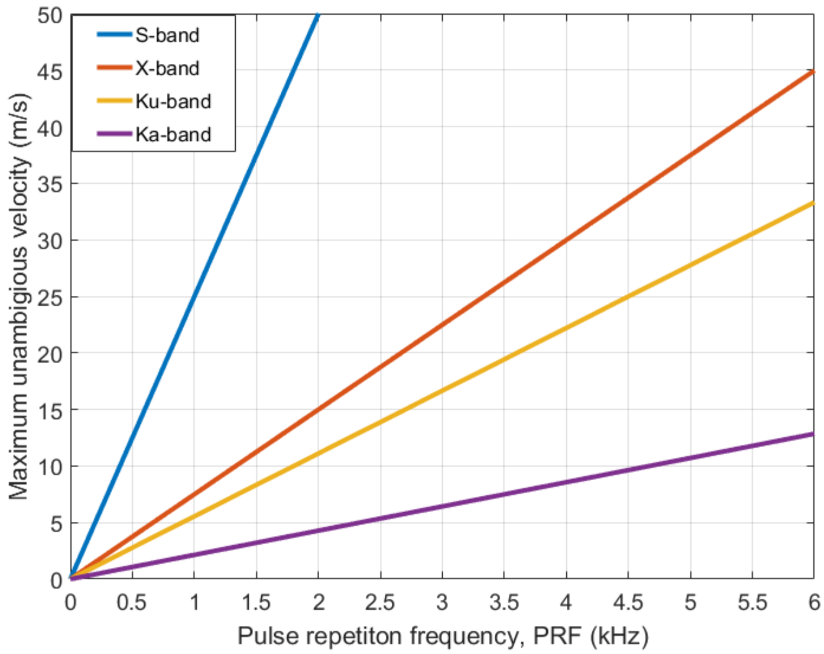

FIGURE 4.2. Illustration of velocity limitation with increasing the pulse repetition frequency at different frequency bands.

The r_a limitation is graphically shown in 4.1 and the v_a limitation is graphically shown in 4.2. From these figures, it is clearly seen that increasing the PRF will increase the v_a linearly but non-linearly decreases the r_a. Consider PRF at 2 kHz, the corresponding r_a is 75 km and the corresponding v_a for X-band is 15 m/s, if the v_a had to be increased to say 30 m/s then the r_a would reduce to 37.5 km. Also as radar operating frequencies increase, typically T decreases to maintain a minimum unambiguous velocity. As a result of this the maximum unambiguous range decreases. For radars operating at these higher frequencies with reduced maximum range, the probability of overlaid echoes present in the signal increases. There is always a trade-off between the r_a and v_a for a given radar having uniform PRT, this is a limitation of the pulsed Doppler radar systems operating with a uniform PRT and is known as the range-velocity ambiguity.

4.1.2. Second-trip echoes. To ensure accurate data is provided to the user from a radar, detection of the second trip and higher order trip echoes is important. The pulsed Doppler radar transmits a train of radar pulses at a PRF; if an echo of a given pulse is received after the transmission of the next pulse, then the echo is considered a second trip echo. In other words, when echoes beyond the maximum range are recorded in such a position to coincide with the location of first trip echoes, the echoes are said to be overlaid. When r_a is limited, the probability of having second trip echoes in the received signal will be high. This problem is most commonly seen in the high frequency radars since they have a short range as compared to the low-frequency radars. It is important to detect these overlaid echoes in the radar signal as they can cause misinterpretation of the data. In order to ensure good quality data to the user, it is necessary to detect and mitigate these overlaid echoes from the original signal received at the radar [15].

The problem of second trip echo is less complicated when the first and second trip echoes do not overlap on each other. However, it is possible to have both first trip and second trip echoes overlapped in the received signal which makes the detection and characterization more complicated. "If a significant storm is located at a distance exceeding the unambiguous range of radar, the second-trip echo can have serious contamination to the first-trip echo [17]". There will be four possibilities when dealing with received signals with second trip echoes and these possibilities are explained with the help of figure 4.3. The radar's range is given by r_{max} in the figure.

(1) Noise only: when there is no precipitation event within or outside the radar's range there will be only measured noise present in the data. This noise signal is undesired and will be filtered out in the signal processor of the radar.

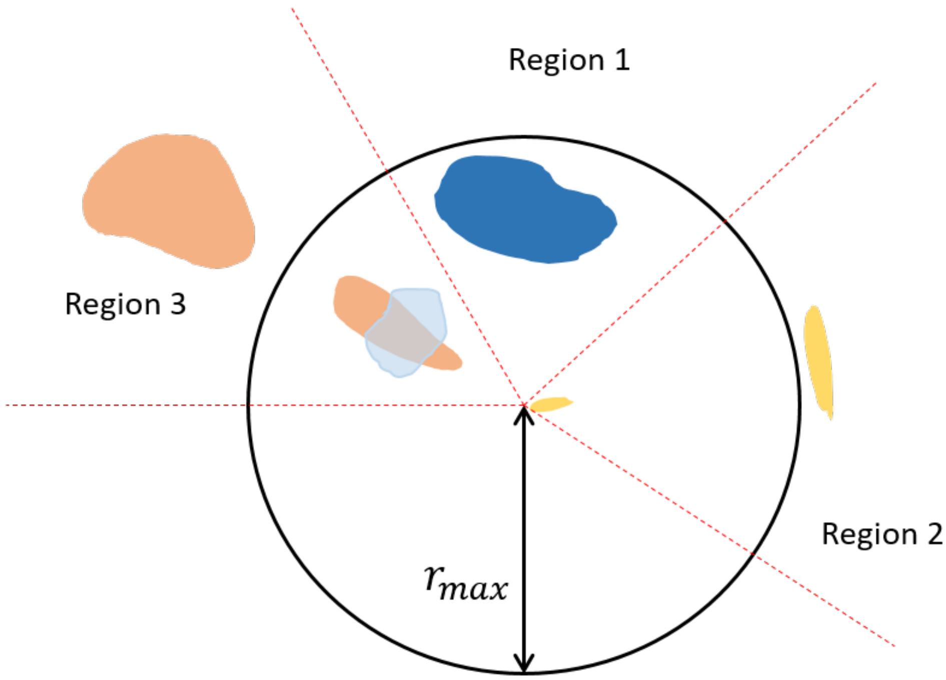

FIGURE 4.3. Illustration of second trip echoes .

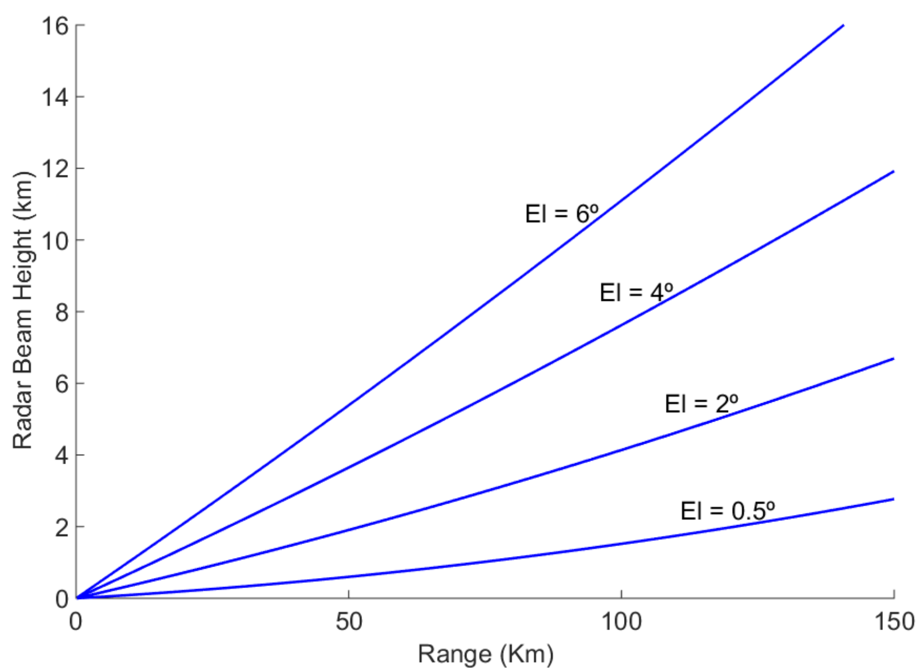

FIGURE 4.4. Radar beam height versus range plot to show the radar beam propagation.

(2) First trip only: If a precipitation event is confined within the radar range and there is no other event happening outside the radar's range, then we encounter only the first trip echoes. In figure 4.3, in region 1 we have precipitation event shown in dark blue, this is the only event in this region and is within the radar's range, so we encounter only first trip echoes.

(3) Second trip only: If there is a precipitation event outside the radar's range and no event is present within the radar's range as shown in the region 2 in figure 4.3, then the received signal at the radar will have only second trip echo. The yellow event outside the radar range will get detected as second trip in the first trip range.

(4) First and second trip overlapped: If there is a precipitation event within and outside the radar's range as shown in region 3, the received signal at the radar will have both first and second trip echoes overlapped. In the figure consider the light blue region as the first trip echo and the orange region outside the radar range as second trip echo, the second trip echo overlaps with the first trip and contaminates the first trip signal as illustrated in the figure.

The second trip echoes look narrower and extend radially towards the center of the radar. At first glance, a radial and narrow echo in the radar display are classified as second trip by meteorologists. Most of the precipitation events are observed below 15 km from the ground, which is limited to the lower part of the troposphere. The radar beam propagation for the different elevation angles is shown in figure 4.4. The earth's curvature is taken care while plotting the beam propagation in this figure; we can see that the 4° beam reaches 12 km at 150 km in range, for radars which have a short range, we could possibly see the second trip echoes even with 4° or 6° elevation.

If a precipitation event is present outside the maximum unambiguous range of the radar, at low elevation angles the radar beam might strike the event and second trip echoes might be present in the signal. The probability of encountering second trip echoes are high at lower elevation angles compared to the higher elevation angles. However, if the vertical depth of the precipitation event is large, then we could see second trip echoes from radar data which is scanning at high elevation angles such as $8°$ in elevation.

4.1.3. Staggered PRT for range-velocity ambiguity solution. The problem of range-velocity ambiguity has been looked into by many researchers in the past and they have come up with methods to improve them. The staggered PRT was one of the methods to increase the maximum r_a and v_a. Dual PRF was another method in which the r_a and v_a was increased. Extensive research was done on the staggered PRT and dual PRF by and many methods have been proposed which gives better output than the uniform PRT transmission.

A high PRF radar may have no ambiguous velocities but will have a very high probability of interference from overlaid echoes. This basic trade-off is especially troublesome at the shorter wavelengths and various attempts have been made to circumvent the difficulty and improve the quality of the signals [18]. Staggered PRT is one of the popular methods used to mitigate the range-velocity dilemma of pulsed Doppler radar.

A typical staggered PRT sequence consists of two staggered periods T_1 and T_2 of pulse spacing. The uniform and staggered PRT pulse scheme are shown in figure 4.5. We can see from the figure that in the staggered PRT the two staggered periods are alternated and a pulse is transmitted at the beginning of each staggered period. For a staggered PRT T_2 is typically greater than T_1. The PRT ratio can be expressed as the ratio of two integers multiples of the radar system's clock $\frac{m}{n}$ [19]. The ratio of staggered PRT is given as

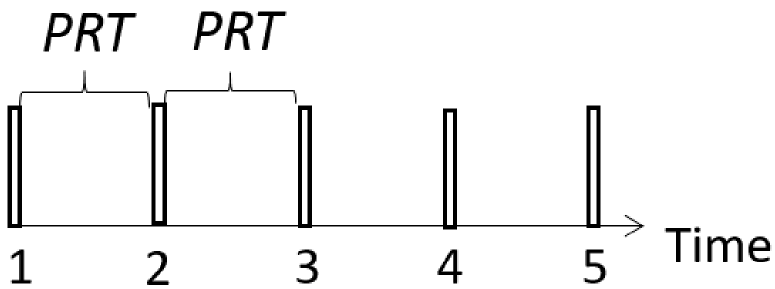

(A) Uniform PRT pulse sequence.

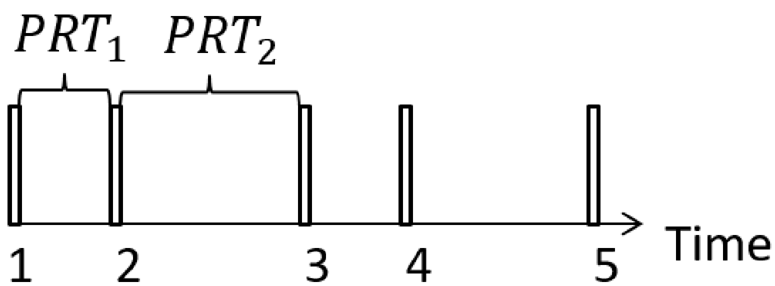

(B) Staggered PRT pulse sequence.

FIGURE 4.5. Uniform and staggered PRT pulse sequence

$$\kappa = \frac{T_1}{T_2} \tag{22}$$

The range-velocity equation 21 for a staggered PRT is given as

$$r_a v_a = \frac{T_1}{T_1 - T_2} \frac{c\lambda}{8} \tag{23}$$

where T_1 and $T2$ are the two staggered periods. From the above equation we can see that when the difference between the two PRT's are small, r_a and v_a can be significantly increased. But decreasing the difference to a very small value will introduce more error

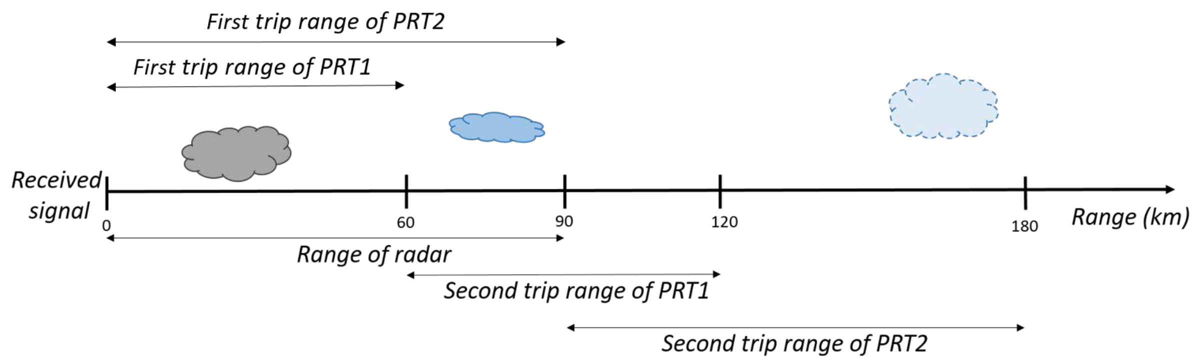

(A) Received signal

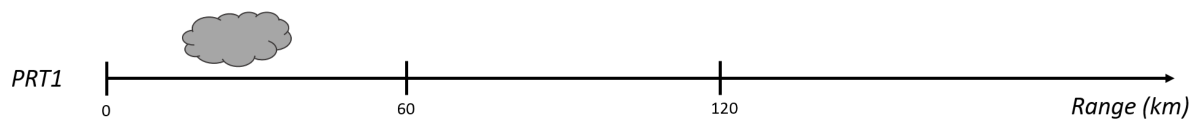

(B) Output of PRT_1 after range dealiasing.

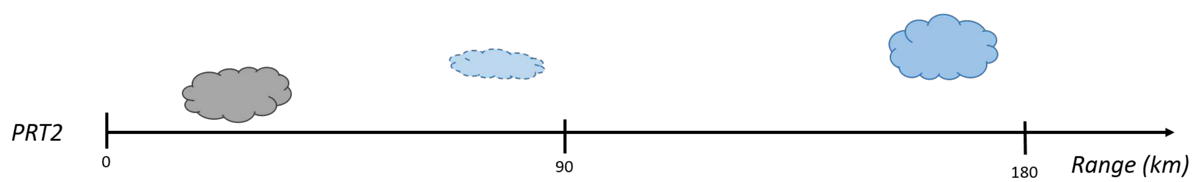

(C) Output of PRT_2 after range dealiasing.

FIGURE 4.6. Illustration of dealiasing of second trip echoes using staggered PRT.

during the moment estimation in the radar. Also in staggered PRT lag-one autocorrelation estimates are made independent with respect to each PRT, these estimates are combined such that the effective maximum unambiguous velocity is extended. The staggering of PRT is implemented in both the polarization of the radar signal [19].

The staggered PRT technique is used to dealias the second trip echoes when second trip echoes are present in the received signal and separated from the first trip echoes. When using the staggered PRT technique the maximum unambiguous range of the radar will be dependent on the longer of two PRT. To understand the second trip dealiasing using the staggered PRT , let us consider D3R timing system, in D3R we use staggered PRT with T_1 = 400 μs which corresponds to maximum unambiguous range of 60 km and T_2 = 600 μs which corresponds to maximum unambiguous range of 90 km, the operational range of the D3R is limited to 40 Km which limits the received signal from these PRT. For illustration let us consider the ranges to be 60 Km and 90 Km for T_1 and T_2 respectively. The PRT ratio of the radar is $\frac{2}{3}$. If the received signal has a second trip echo, based on which PRT the second trip echo is present we can dealias the signal to its correct range gate. This involves first characterizing and classifying the echoes as first trip and/or second trip. If both first trip and second trip overlap, both the first trip and second trip signal moments are computed. In Figure 4.6(a), the maximum operational range of the radar is 0 km to 90 km (a result of the PRT used), second trip range interval of T_1 which spans from 60 km to 120 km and second trip range interval of T_2 which spans from 90 km to 180 km is also shown. Let us also assume that the received signal consist of both first and second trip echoes and second trip echo is associated with T_2. In figure 4.6(a) the first trip is shown as an event in gray and second trip is shown as an event in blue. After separating T_1 and T_2 data When we see the T_1 data as shown in Figure 4.6(b), since no second trip is present we can see only first trip event, but when we take a look at T_2 as shown in Figure 4.6(c), we see first trip signal as well as second tip signal which is unfolded to the correct range between 90 km - 180 km. By using this method, the second trip echoes received if any can correctly be placed in their range bins after detection.

4.2. Phase Coding for Separating Overlaid Echoes

Coding the transmitted pulse from the radar was implemented so that the receiving data from each pulse would be unique, these were known as the phase coding schemes. Phase coding schemes were studied to improve the quality of the signals which would be corrupt by second or higher order trip echoes. In the phase-coding scheme, the transmitted pulses are tagged with a phase code or switching phase. The switching phase can be random phase sequences or systematic phase sequence [20]. The phase codes which are assigned to each transmitted pulse is unique with respect to the next few pulses. This phase code information which is added to the pulse is stored digitally to be used in re-cohering the received signal.

Different phase coding schemes were used in the past such as random phase codes and systematic phase codes [21] [22]. In the past, random phase codes and SZ codes for X and S-band radars have been studied and implemented [20]. In this thesis, simulation results for random phase codes and SZ codes for Ku and Ka band is studies with the help of simulations. Currently, researchers have been working on different intra-pulse and inter-pulse coding schemes which will make the radar systems more robust.

4.2.1. Systematic phase codes. Systematic phase codes are sequences which have a periodic property. The systematic sequences is defined as

$$R(\tau) = \begin{cases} N, & \tau = 0(modN) \\ 0, & \tau \neq 0(modN) \end{cases} \tag{24}$$

There are many sequences which satisfy this property; Chu sequences are one among them. Chu sequences and SZ codes are exactly the same [23]. SZ sequences are always defined as SZ(n/M), this is because the n/M factor decides the spectral distribution of the modulated incoherent signals. In this study n=8, M=64 is considered. For SZ(n/M) sequence, the switching code is given by

(25) $$\psi_k^i = -\sum_{m=0}^{k}[\frac{n\pi}{M}\sum_{p=0}^{2i}(m+p)^2]; i = 0, 1, 2, ...and k = 0, 1, 2, , ..., M-1$$

The corresponding modulation code is given by

(26) $$\phi_k^i = (\frac{n\pi}{M})\sum_{m=0}^{2i}(m+k)^2]; i = 0, 1, 2, ...and k = 0, 1, 2, , ..., M-1$$

The modulation code has a periodicity of P given by

(27) $$\frac{M}{n} = \frac{P}{r}$$

where r is an odd integer. The periodicity of the switching code is 4P.

4.2.2. Random phase codes. Random phase codes are basically a random sequence generated and each value is added to the transmitting phase of the radar pulse. Random sequences are those sequences which have zero aperiodic autocorrelation at nonzero lags. The random phase sequence is defined as

(28) $$R(\tau) = \begin{cases} N, & \tau = 0 \\ 0, & \text{otherwise} \end{cases}$$

Realistically finite length sequence with this property cannot be generated. However, we can generate pseudo-random sequences which have very low autocorrelation at nonzero lags. In dual-polarized radars for two channels (Horizontal and vertical polarization) two pseudo-random sequences are generated such that

$$C_{i,j}(\tau) = 0, \forall \tau \tag{29}$$

4.2.3. Moment estimation using phase codes. A radar employing random phase coding will have an independent, uniformly distributed, starting phase for each transmitted pulse. The codes are digitally stored in the radar and the received signal is checked for their coherency. The phase shift of transmitted pulse causes received signal to be coherent only with their respective transmitted pulse and incoherent with other pulses [21]. In a random phase-coded waveform the received second- and higher-order trips are random phase modulated [20]. Similarly in systematic phase codes the received second- and higher-order trips are phase modulated base on the systematic phase code used.

Second trip echoes can be eliminated using random and systematic phase codes. This process is explained in detail using the figure 4.7. This overall process is explained with respect to random phase coding; however, this process is similar to systematic phase coding. Let us assume the received signal from the radar consists of first and second trip echoes in the resolution volume. The spectra of the signal which spans from $+v_a$ to $-v_a$ is shown in the figure 4.7(A), in this figure the blue spectra corresponds to the spectral components of the first trip and the yellow components correspond to the spectral components of the second trip signal. For the ease of illustration, the two spectra are not overlapped, however, if the two spectra may be overlapped in the actual signal and this method still holds good. The out-of-trip signal will appear as white noise when cohered to the first-trip phase [24].

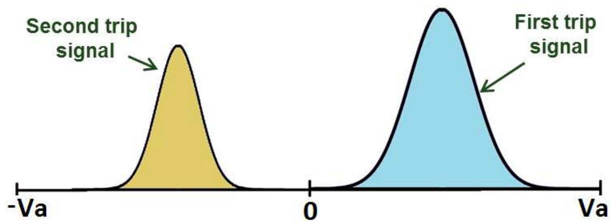

(A) Received signal spectra.

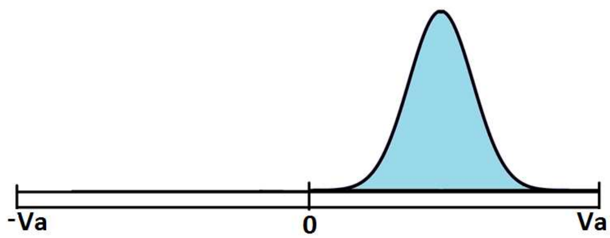

(B) Spectra of received signal cohered to first trip.

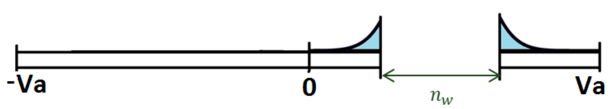

(C) Notch filtered signal after removing the first trip components.

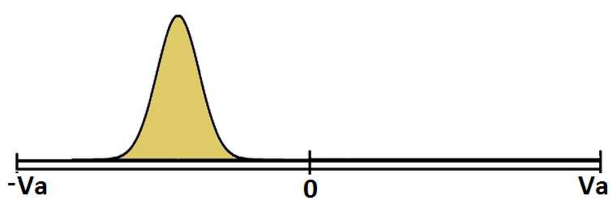

(D) Spectra of filtered signal cohered to second trip.

FIGURE 4.7. Illustration of separating first and second trip signals using random phase coding scheme.

So when the received signal from the radar is cohered for the first trip, the second trip components will be embedded in the signal as white noise, the spectra of the received signal cohered with the first trip is shown in figure 4.7(B). In this figure, we can see only the first trip components are present and the second trip components are embedded in the noise. The first trip moments are computed using this signal. Next, the first trip signal components are removed from this signal using a band reject filter with a notch width n_w which is centered on the first trip spectrum. The spectrum of the filtered signal which looks like noise is shown in figure 4.7(C). It should also be noted that a part of the second trip signal which is embedded in the noise component is removed by filtering the signal. The notch width of the band rejection filter is chosen appropriately. The filtered noise signal is then re-cohered with second trip, using the random code stored for the previous pulse. The spectrum of the re-cohered signal is shown in figure 4.7(D). The noise floor in this spectra will be increased due to the filtering of the signal in the previous stage. The second trip moments are now calculated. Corrections for the second trip moments estimated due to filtering at previous stage are applied. The power of the second trip P_2 is computes using $P_2 = P_{NF}/(1 - n_w)$, where P_{NF} is the power of notch filtered signal. This way we can estimate the first and second trip moments using the random phase code scheme, this method also works when the first trip and second trip signal overlap on each other. This process forms part of the algorithm used in range ambiguity characterization and mitigation fro D3R 2.0 explained in the next section. For systematic codes such as SZ codes, the methods explained above is similar except that the second trip will appear as side bands with symmetric properties instead of white noise.

4.2.4. Results of simulations of SZ phase codes for second trip estimation at Ku band. Simulations were done to see the performance of SZ codes for second-trip estimation. Simulations were carried out at both frequency bands of Ku and Ka. For the simulation, SZ codes were considered with n = 8 and M = 64. The spectral width of the second trip is taken as 2 m/s. The first trip spectral width was varied from 0.5 to 5 and the first trip power to second trip power ratio was varied from 1 to 70, at each value the second trip parameters were estimated taking N=64 samples.

Figure 4.8 shows the results of simulation at Ku band. Figure 4.8 (A) shows the bias in second trip power estimated ($\hat{p}_2$), figure 4.8 (B) shows the bias in second trip velocity estimated ($\hat{v}_2$) and figure 4.8 (C) shows the standard deviation of error in second trip velocity estimated ($\hat{v}_2$). From this figure, we can see that an unbiased estimate will only be obtained in the recovery region. For 2 m/s spectral width in the first trip, an unbiased estimate will be obtained only till $p1/p2 < 25dB$. As we go higher in spectral width of the first trip, the recovery region becomes very small.

Figure 4.9 shows the results of simulation at Ka band. Figure 4.9 (A) shows the bias in second trip power estimated ($\hat{p}_2$), figure 4.8 (B) shows the bias in second trip velocity estimated ($\hat{v}_2$) and figure 4.8 (C) shows the standard deviation of error in second trip velocity estimated ($\hat{v}_2$). From this figure, we can see that an unbiased estimate will only be obtained in the recovery region. For 1 m/s spectral width in the first trip, an unbiased estimate will be obtained only till $p1/p2 < 20dB$. We can see that the recovery region is very small as compared to Ku, this is due to the increase in frequency which decreases the v_a. Phase codes at Ka band will work reasonably for only limited data.

4.2.5. Results of simulations of random phase codes for second trip estimation at Ku band. Simulations were done to see the performance of random codes for second-trip estimation. Simulations were carried out at both frequency bands of Ku and Ka. For the simulation. The spectral width of the second trip is taken as 2 m/s. The first trip

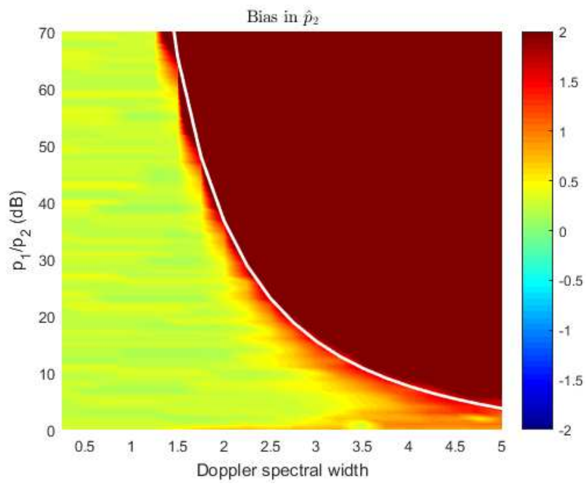

(A) Estimated second trip power bias.

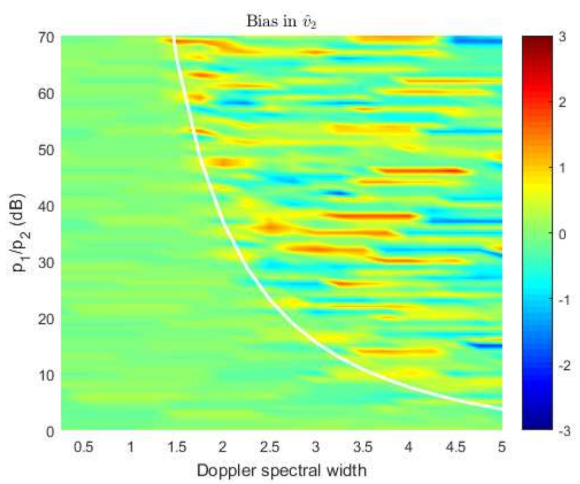

(B) Estimated second trip velocity bias.

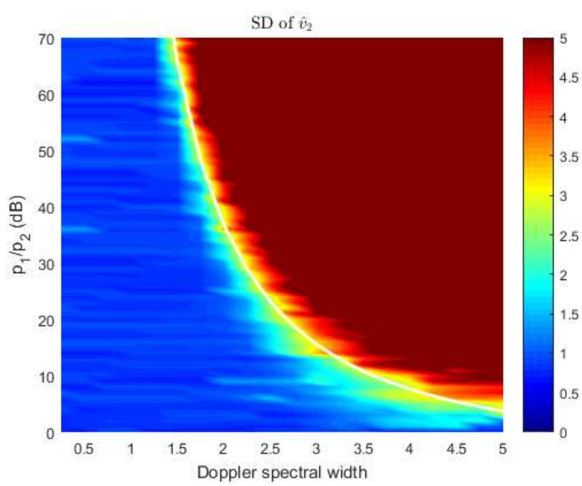

(C) Estimated second trip velocity standard deviation.

FIGURE 4.8. Second trip estimation results using SZ phase codes at Ku band.

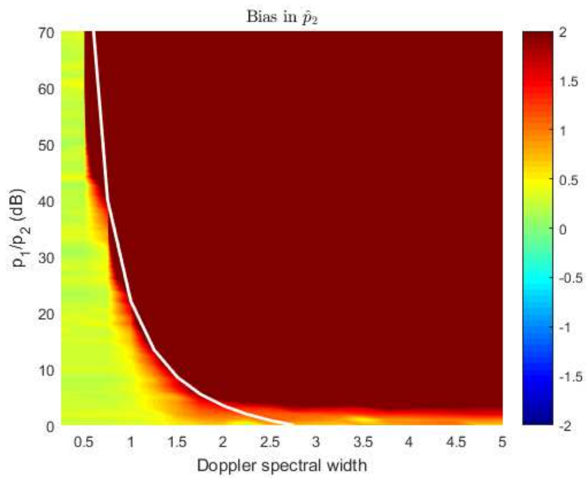

(A) Estimated second trip power bias.

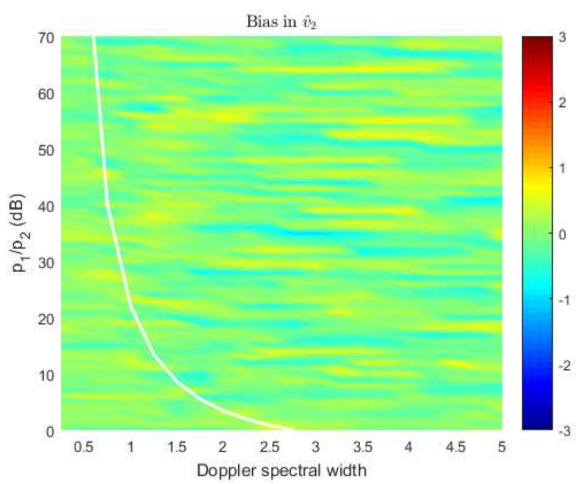

(B) Estimated second trip velocity bias.

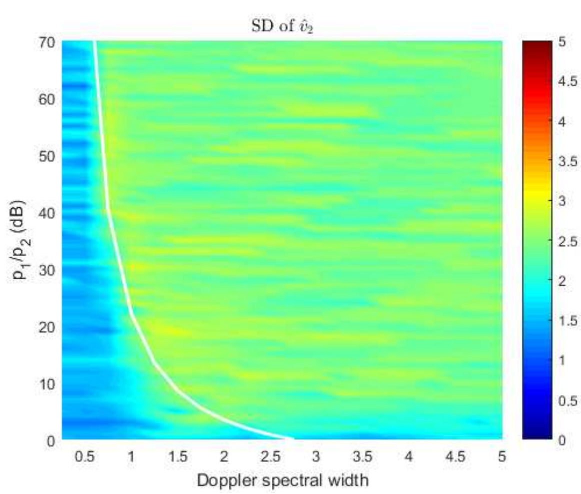

(C) Estimated second trip velocity standard deviation.

FIGURE 4.9. Second trip estimation results using SZ phase codes at Ka band.

spectral width was varied from 0.5 to 5 and the first trip power to second trip power ratio was varied from 1 to 70, at each value the second trip parameters were estimated taking N=64 samples.

Figure 4.10 shows the results of simulation at Ku band. Figure 4.10 (A) shows the bias in second trip power estimated ($\hat{p}_2$), figure 4.10 (B) shows the bias in second trip velocity estimated ($\hat{v}_2$) and figure 4.10 (C) shows the standard deviation of error in second trip velocity estimated ($\hat{v}_2$). From this figure, we can see that an unbiased estimate will only be obtained in the recovery region. For 2 m/s spectral width in the first trip, an unbiased estimate will be obtained only till $p1/p2 < 20dB$. As we go higher in spectral width of the first trip, the recovery region becomes very small.

Figure 4.11 shows the results of simulation at Ka band. Figure 4.11 (A) shows the bias in second trip power estimated ($\hat{p}_2$), figure 4.11 (B) shows the bias in second trip velocity estimated ($\hat{v}_2$) and figure 4.11 (C) shows the standard deviation of error in second trip velocity estimated ($\hat{v}_2$). From this figure, we can see that an unbiased estimate will only be obtained in the recovery region. For 1 m/s spectral width in the first trip, an unbiased estimate will be obtained only till $p1/p2 < 10dB$. We can see that the recovery region is very small as compared to Ku, this is due to the increase in frequency which decreases the v_a. Phase codes at Ka band will work reasonably for only limited data.

Also comparing the SZ and random phase codes, we can see that SZ phase codes perform better than random phase codes. The recovery region of SZ phase codes is greater than when using random phase codes. Also, bias of second trip estimates from SZ code is less noisy compared to random phase codes.

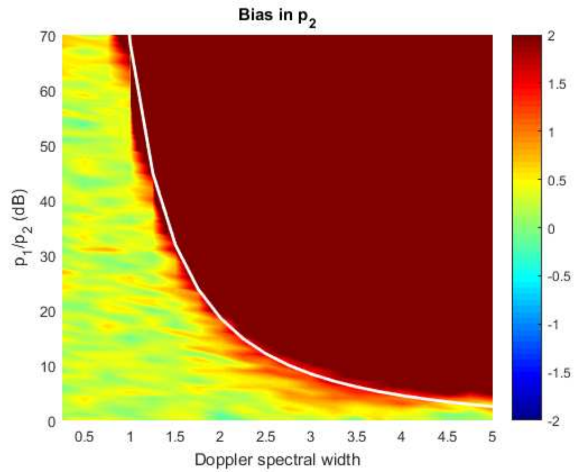

(A) Estimated second trip power bias.

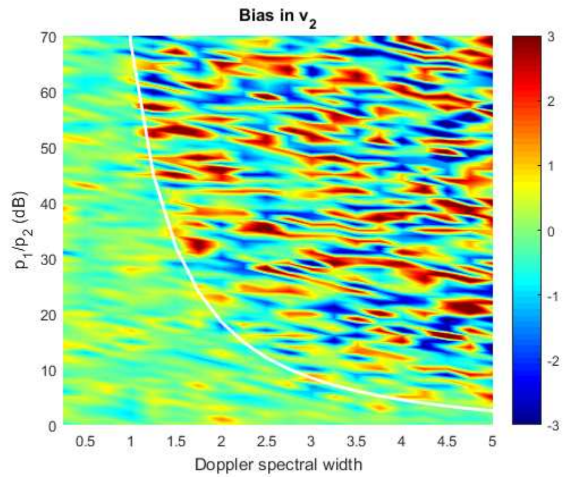

(B) Estimated second trip velocity bias.

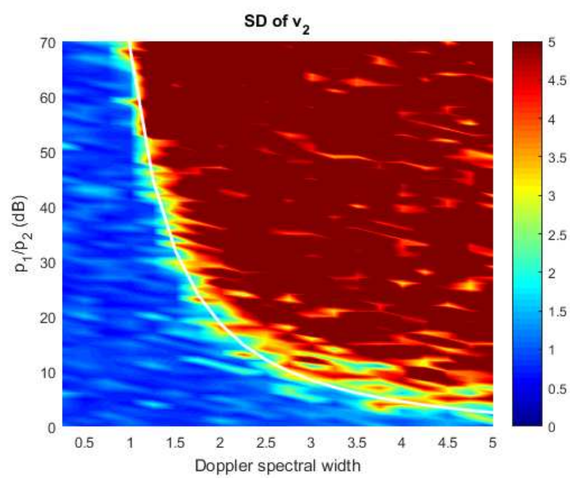

(C) Estimated second trip velocity standard deviation.

Figure 4.10. Second trip estimation results using random phase codes at Ku band.

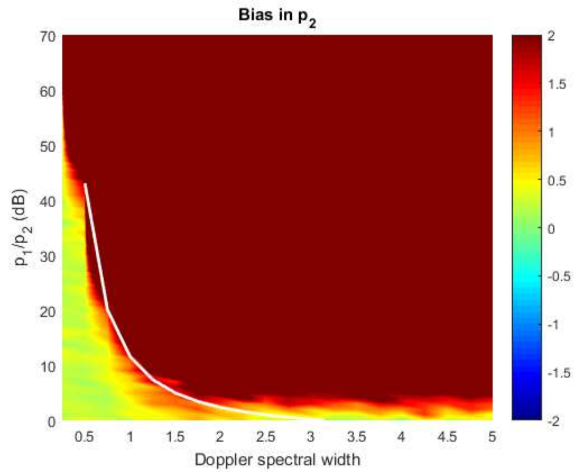

(A) Estimated second trip power bias.

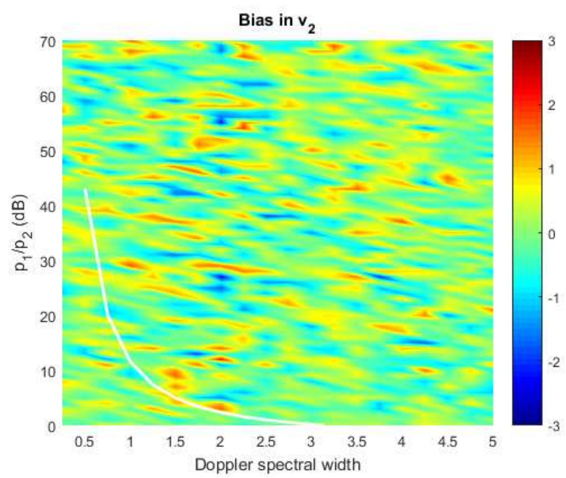

(B) Estimated second trip velocity bias.

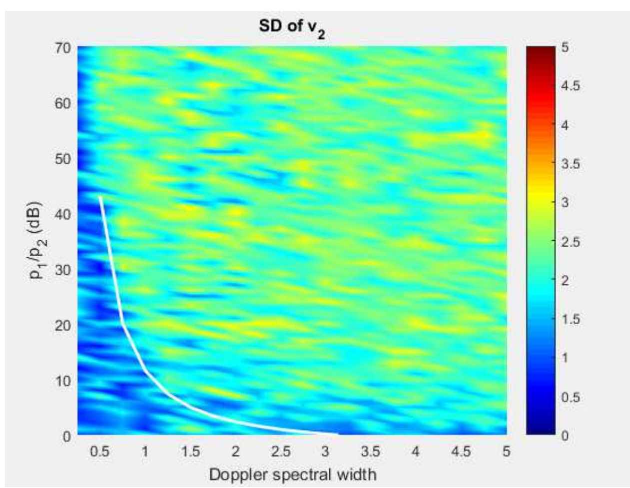

(C) Estimated second trip velocity standard deviation.

FIGURE 4.11. Second trip estimation results using random phase codes at Ka band.

4.3. Range ambiguity characterization and mitigation for D3R

4.3.1. Algorithm. The signal received at the radar receiver is sent to the amplifier stages and then the signal is sent to the digital receiver where the I/Q signals are generated. This I/Q signals are sent to the moment processor where all the signal processing for the data is accomplished and we get the output as radar moments. The range ambiguity characterization and mitigation is done in the signal processor and the algorithm explained below is implemented in the signal processor.

Few radars use both staggered PRT and phase coding to overcome range ambiguity and other radars either use staggered PRT or phase coding or none for their processing of the received radar signal. In D3R, the algorithm uses the information of staggered PRT and the random phase coding which will characterize and mitigate the second trip echoes. The combination of these two methods works well when the first trip and the second trip echoes do not overlap on each other. When there is an overlap of the first and the second trip this method will give errors in the estimation of second trip, depending on the spectrum width of the first trip. This is because of limited Doppler spectrum available. For Ku band with PRF $500\mu s$, the v_a is 10.78 m/s. The algorithm is explained using a flowchart shown in figure 4.12. The use of systematic phase codes such as SZ codes will be implemented in future and their results will be studied.

The received signal at the signal processor is separated corresponding to the two PRT's ($400\mu s$ and $600\mu s$). The total power of each PRT signal is then computed. Next, the power of the signals is compared with the noise threshold level of the system. It is important to carefully choose the noise threshold level based on the noise floor of the radar system. The noise threshold is set little above the noise floor of the system. If we choose a noise threshold which is too high, we might lose precipitation data from the signal. If the received power

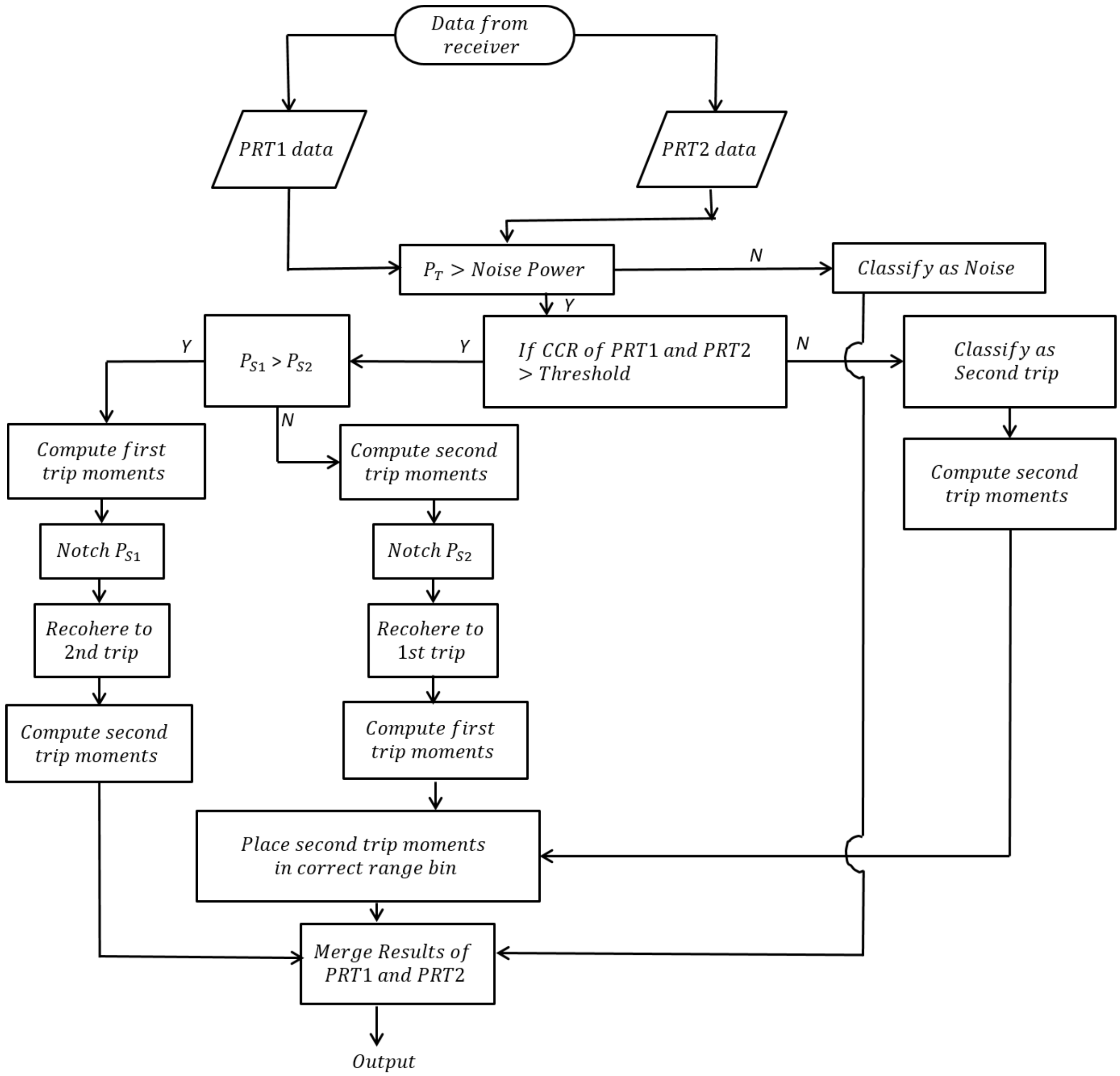

FIGURE 4.12. Flowchart of range ambiguity characterization and mitigation.

from the resolution volume of both the PRT's are below the noise threshold, then the data is classified as noise signal and subsequently removed from the processing.

If the signal is not a noise signal, then for that particular range bin correlation of the two PRT signals is computed. If the correlation of the signal is less than the correlation threshold, then the signals are classified as second trip signals with no overlap on the first trip. This is because if a first trip signal is present, we will have correlated signal components present in both PRT's and the correlation between the two PRT's will be high. If the received signals have correlation values higher than the correlation threshold, then the signals are classified as signals containing first and second trip signals.

After the signals are compared with the correlation threshold, if the signals are classified as second trip signals then the second trip moments are computed. The second trip moments computed are places in their respective range bin, this is the advantage of using the staggered PRT's. We can correctly assign the range bin of the second trip using the staggered PRT, which would not have been possible with uniform PRT signals.

If the correlation is higher than the correlation threshold. The signal is cohered to both first and second trip using the random phase codes and their respective power is computed for each PRTs' data. Using the information of computed powers, if the power of the first trip is greater than the second trip, the first trip moments are computed and placed in the respective range bin. A band rejection filter with spectral width n_w is applied for the first trip signal. The filtered signal is then cohered to the second trip; the second trip moments are computed and placed in the correct range bin. This process is done as explained in the previous section. If the second trip power is greater than the first trip, the second trip moments are computed. Then the band rejection filter is applied to the second trip spectra, and the signal is cohered for the first trip. The first trip moments are then computed. The first and second trip signals are then placed in their respective range bins.

In the final step, the results from both the PRT's are merged to produce the final received power versus range profile. This final result will have the first trip and the second trip signals in their respective range bins.

4.3.2. Case studies with D3R data. In this sub-section actual radar data from the D3R is considered to demonstrate the effectiveness of the algorithm explained. Two cases are considered here in which the second trip echoes are present. The first case is taken from

11th of November 2015 at 16:35 UTC when the D3R was deployed in Moclips, WA, USA as part of the GPM OLYMPEx ground validation field campaign. The elevation angle of the scan is 0.54°.

Figure 4.13 (A) shows the reflectivity moment from the D3R in which the second trip echoes are present. The red circle highlights the region in which second trip echoes are present. From this figure, it can be clearly seen that the first trip echoes are corrupted by the second trip echoes and the user might interpret the second trip echoes as precipitation event happening at that particular region. It is also seen from the figure that the second trip echoes have radial features and extend towards the center of the radar. The second trip echoes can mostly be seen in the western region of the radar, on the eastern side the reflectivities are dominated by the first trip echoes.

The range ambiguity characterization and mitigation algorithm is applied, the reflectivity output after correction is applied for the first trip range is shown in figure 4.13 (B). From this figure, it can be seen that the second trip echoes have been removed from the first trip region. Figure 4.14 (A) shows the estimation of second trip reflectivity. The second trip reflectivity values are placed in their respective range bins. Range factor in the reflectivity is taken care when the second trip data is placed in the correct range bins.

In order to verify the second trip echoes determined are actually present in those range bins, a reflectivity plot from the NASA NPOL radar which was located near to the D3R during the field campaign is shown in figure 4.14 (B). We are able to see echoes from such large distances from the NASA NPOL radar in the first trip itself because this radar is operating at S-band frequency, so we get a larger unambiguous range than that of the D3R. Comparing with the NPOL reflectivity, we can see that the algorithm performed well in characterizing and mitigating second trip echoes. However, we can also see from the figure that there are some estimation errors in the output data.

The second case is taken from 29th July 2016 at 13:51 UTC when the D3R was in Wallops Flight Facility, VA, USA. The elevation angle of the scan is 6°. This is an interesting case because we can observe second trip echoes when the radar is scanning at such high elevation angles.

Figure 4.15 (A) shows the reflectivity moment from the D3R in which the second trip echoes are present. The second trip echoes present are highlighted in red. In this case, the first trip echoes are mostly located in the farther ranges of the north western region. We can see the radial features of the second trip echoes. We can also observe that the second trip signal located on the south eastern side looks like a first trip signal because of the high reflectivity values present.

The range ambiguity characterization and mitigation algorithm is applied, the reflectivity output after correction is applied for the first trip range is shown in figure 4.15 (B). From this figure, it can be seen that the second trip echoes have been removed from the first trip region. Figure 4.16 (A) shows the estimation of second trip reflectivity. The second trip reflectivity values are placed in their respective range bins. Range factor in the reflectivity is taken care when the second trip data is placed in the correct range bins.

In order to verify the second trip echoes determined are actually present in those range bins, a reflectivity plot from the nearest NEXRAD radar, KDOX is taken. NEXRAD is a network of dual-polarized radars operating and providing meteorological information across the USA. The KDOX reflectivity plot centered at Wallops flight facility where the D3R was located is shown in 4.16 (B). Since NEXRAD radars also operate in the S-band they have large operational range, so we can see the echoes from far distances in the first trip itself.

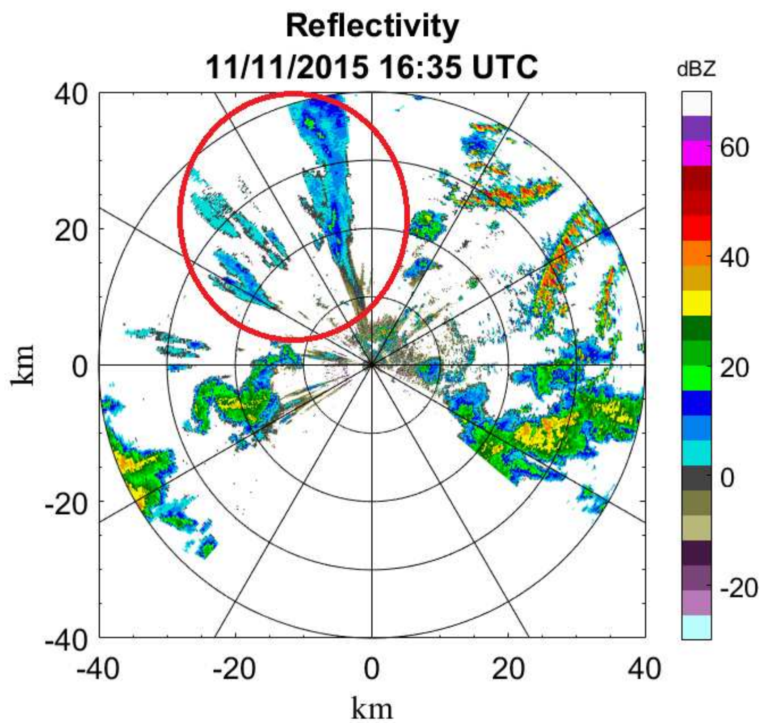

(A) Reflectivity output from the D3R without any correction.

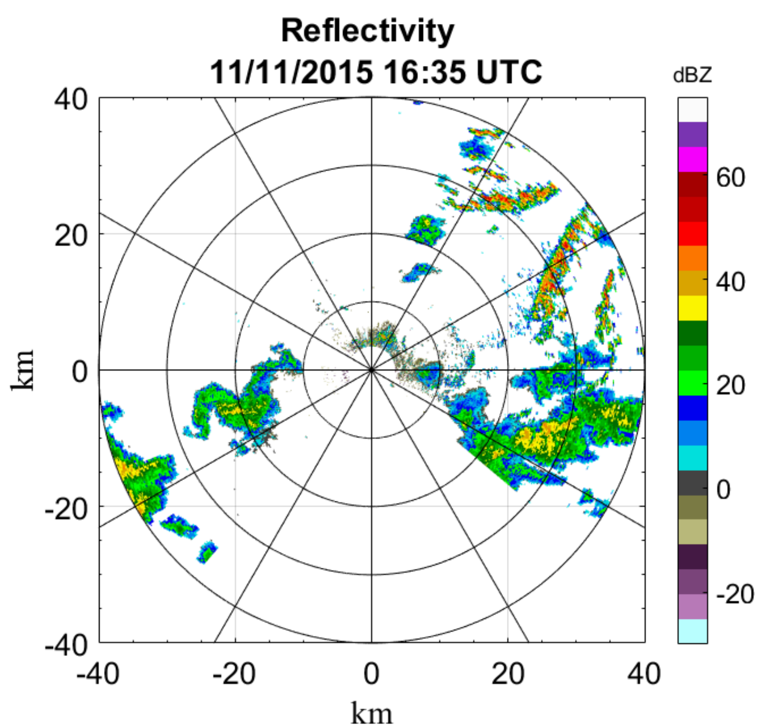

(B) Reflectivity output from the D3R after correction (first trip range).

FIGURE 4.13. Performance of second trip characterization and mitigation algorithm for 11th of November 2015 case, first trip range plots.

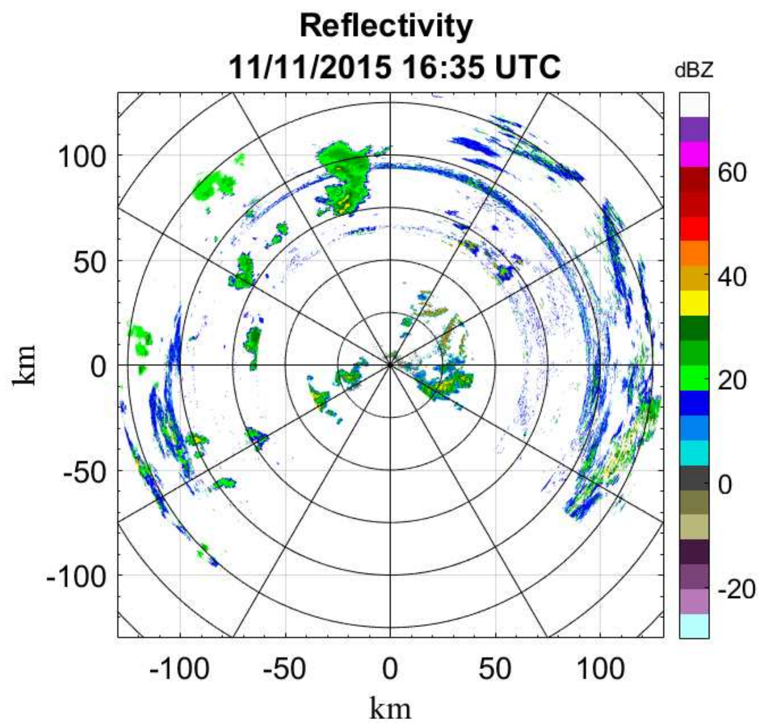

(A) Reflectivity output from the D3R after correction (second trip range).

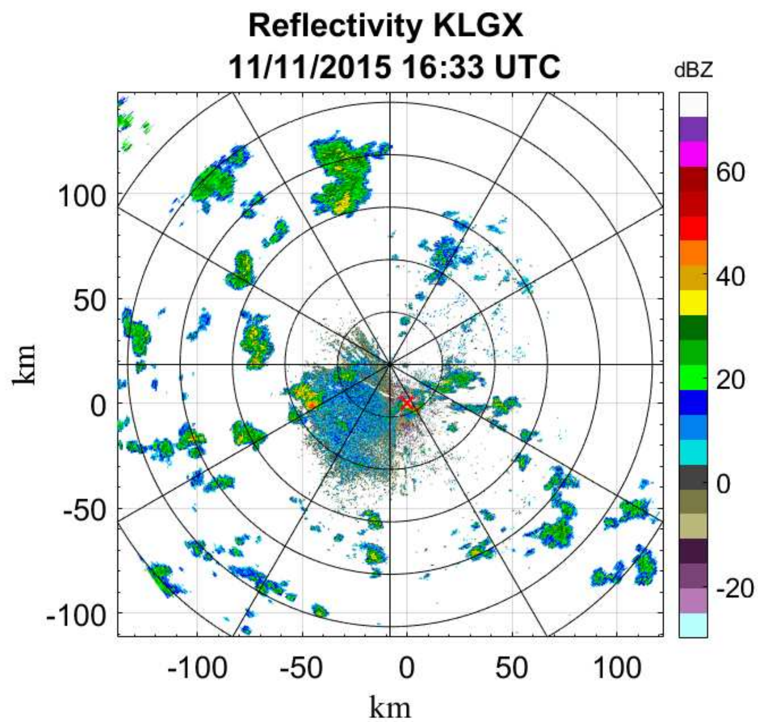

(B) Reflectivity from NASA NPOL radar.

FIGURE 4.14. Performance of second trip characterization and mitigation algorithm for 11th of November 2015 case, second trip range plots.

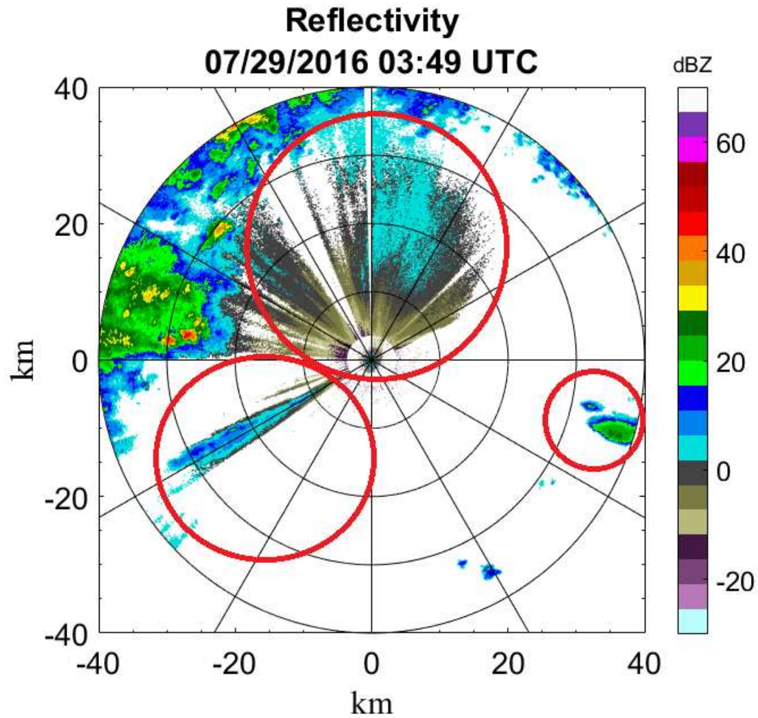

(A) Reflectivity output from the D3R without any correction.

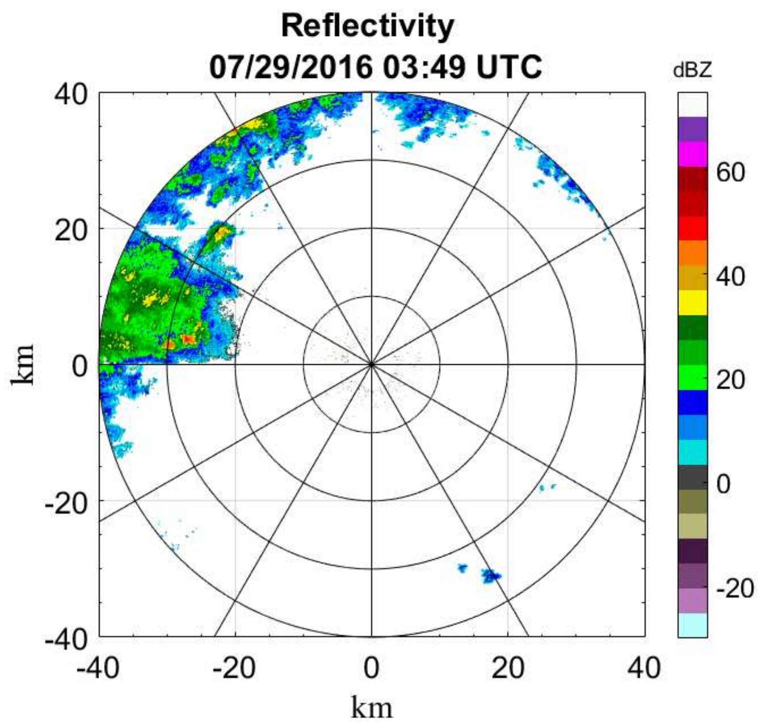

(B) Reflectivity output from the D3R after correction (first trip range).

FIGURE 4.15. Performance of second trip characterization and mitigation algorithm for 29th July 2016 case, first trip range plots.

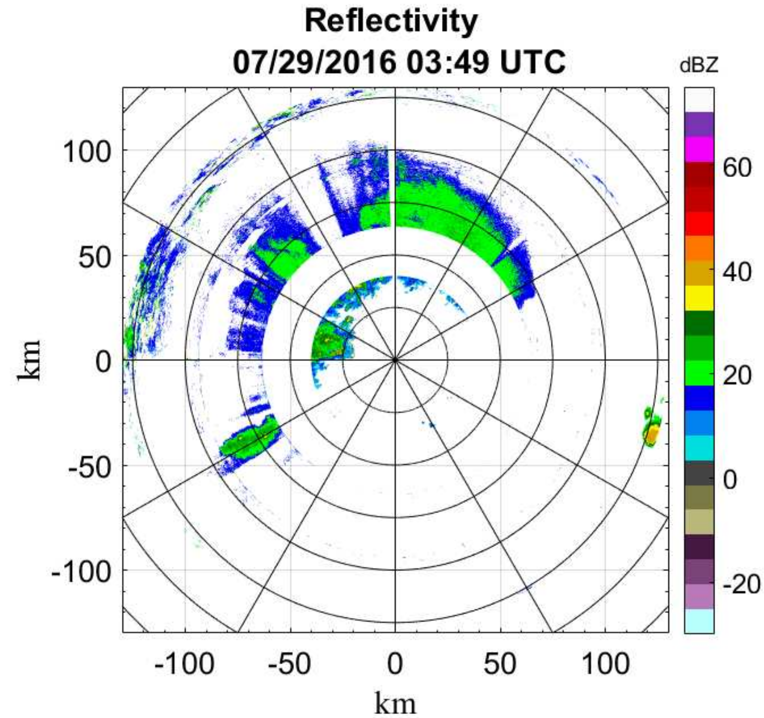

(A) Reflectivity output from the D3R after correction (second trip range).

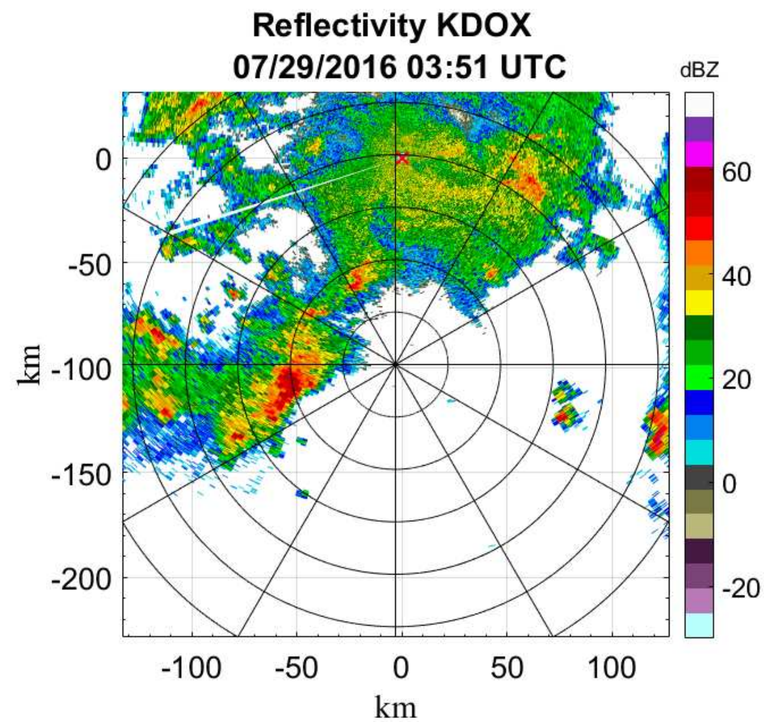

(B) Reflectivity from NEXRAD KDOX radar.

FIGURE 4.16. Performance of second trip characterization and mitigation algorithm for 29th July 2016 case, second trip range plots.

Comparing the result with the KDOX reflectivity, we can see that the algorithm performed well. However in this case also we can see some estimation errors in the output data.

4.4. Velocity ambiguity mitigation algorithm for D3R

Staggered PRT and staggered-PRF techniques for extending the unambiguous velocity have been known for more than two decades and are available on several operational Doppler weather radars, especially for radars operating at higher wavelengths [25]. But as we go higher in frequency the v_a values will get smaller, the improvement we get using the staggered PRT or dual PRF is also insufficient to span the full range of velocities of the precipitation event, as mentioned earlier some of the storms might go up to 80 m/s and detecting these high velocities is crucial especially for algorithms such as tornado tracking. An algorithm which increases the v_a for dual-frequency radars is presented in this work. We can see that the velocities can the correctly unfolded to the original velocity values from this method.

In this section, the method to dealias the velocity folding for dual-frequency radars like D3R is explained. As discussed earlier the maximum/minimum velocity value a radar can measure is dependent on the frequency of operation of the radar and the PRF at which the radar is operating. It is also dependent on the maximum range a radar can observe. The range and velocity are fixed for a given radar, but for high frequency radars, the velocity range will be limited. The velocity range is improved using the staggered PRT technique the velocity range improvement depends on the two PRT's which are used, but we would still not get a dynamic range that will cover all the velocity components of the storm. To give an idea of the velocity ranges let us consider a D3R Ka band radar system operating at 35.56 GHz. Let the PRT of radar in uniform mode be 500 μs and when operating in staggered mode be 400 μs and 600 μs respectively. With these parameters, the v_a in uniform mode is

4.22 m/s and in staggered mode is 10.55 m/s. We can see that even for staggered mode v_a is not sufficient to represent the full range of velocity values for a decent startiform event.

The velocities for a dual frequency radar operating at 13.5 GHz which is in the Ku band and 35.5 GHz which is in the Ka band are simulated. It is assumed that the radar is operating in the staggered mode with v_a of Ku at 27 m/s and v_a of Ka at 10.6 m/s. Velocities up to 80 m/s are simulated, for both Ku and Ka frequency bands and the velocities are folded based on the v_a's. The simulated Doppler velocities after aliasing of Ku and Ka band is shown in figure 4.17. In this figure, we can see that the Ku and Ka velocities are folded once it crosses the interval of v_a.

For dual frequency radars, both the frequency bands share a common resolution volume when scanning. They scan the same resolution volume at a given instant of time. It is also true that the velocities of both the frequency bands are true and unaliased within v_a corresponding to the higher frequency band. The velocities of the two frequency bands are computed and their difference is compared with a threshold value. If the velocities are less than the threshold value, then the velocities are marked as correct, if they are greater than the threshold they are marked as incorrect velocity value. This information is used to create a mask of correct and incorrect velocities by subtracting the velocities of the two frequency bands. Next, the incorrect velocities are separated to positive and negative regions and a mask is created as shown in figure 4.18 (A). It should be noted that multiple zero regions can be present if the unambiguous velocities are low. The mask generation is done considering these cases to get accurate results.

Velocities are corrected using the positive and negative mask values by adding $2v_a$ and $-2v_a$ respectively. In the next stage, the difference between the corrected velocity value and the Ku velocity value is taken. This difference is compared to a threshold and the mask is

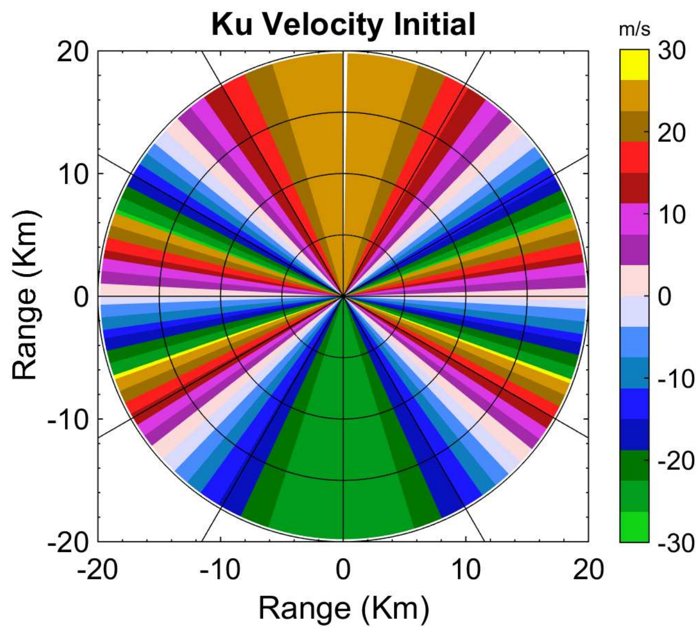

(A) Simulated Ku velocity values before correction

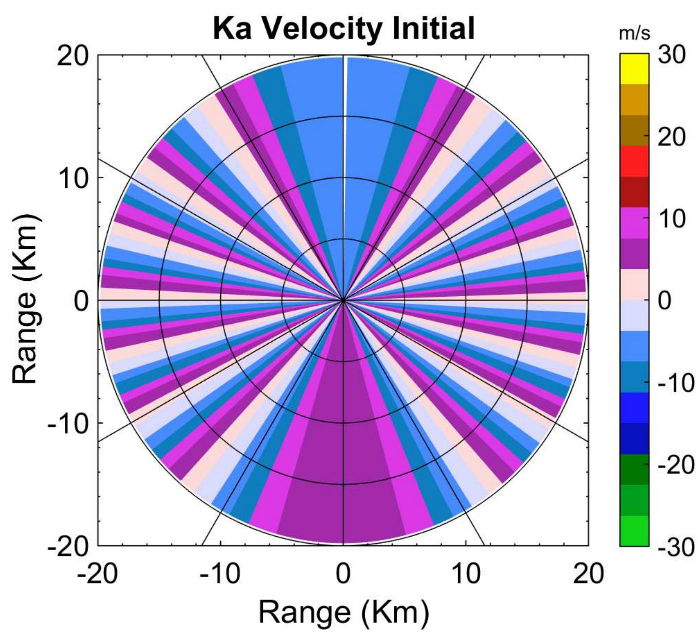

(B) Simulated Ka velocity values before correction

FIGURE 4.17. Simulation of velocities before correction.

updated as shown in figure 4.18 (B). The velocity values are again corrected accordingly in this stage. The third stage mask is shown in figure 4.18 (C) and the velocities of Ka band is corrected. In this way, the velocities are iteratively corrected for Ku and Ka band using the information of the correct, positive and negative velocities. The final corrected velocities are shown in figure 4.19. We can see from this figure that all the velocities of Ku and Ka band are corrected and we get the true velocities. The scatter plot of the velocities of Ku and Ka before and after correction is shown in figure 4.20. From the scatter plots we can see that there is one to one relationship between the Ku and Ka band velocities after correction.

4.4.1. Case studies with D3R data. Since D3R is a dual-frequency radar, the radars velocity data is considered to show the performance of the velocity ambiguity mitigation method discussed in the previous sub-section. Two cases of data are considered here. The first case is taken on 3rd of December 2015 when the D3R was deployed in Moclips, WA, USA as part of the GPM OLYMPEx ground validation field campaign. The D3R was operating in staggered mode of operation with $PRT_1 = 600\mu s$ and $PRT_4 = 400\mu s$, elevation angle of the scan is 0.54 degrees.

Figure 4.21 shows the velocity data from Ku and Ka band before the correction is applied. This is how the velocity moment looks from the output of the D3R signal processor. The unambiguous velocities of Ku and Ka band when operating in staggered mode is 27 m/s and 10.6 m/s; we can see the velocities folding after these values in the figures.

Figure 4.22 shows the velocity data from Ku and Ka band after the correction is applied. The intermediate stages of velocity correction are not shown here. From the figures, we can see that the velocity values of both Ku and Ka have been unfolded to actual velocity values of the storm. We also see that this method will give output in the regions where both Ku and Ka velocities are present. The scatter plots of the velocity data before correction and

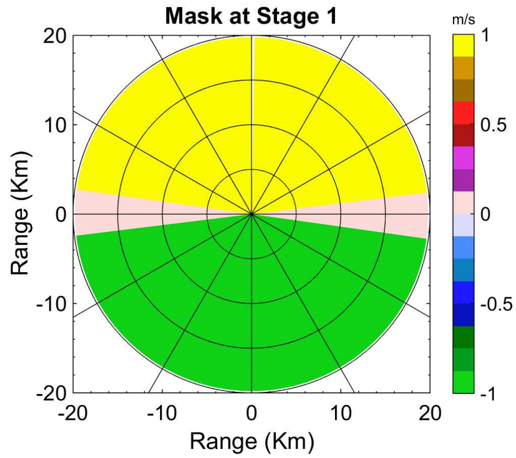

(A) Mask used for unfolding at stage 1

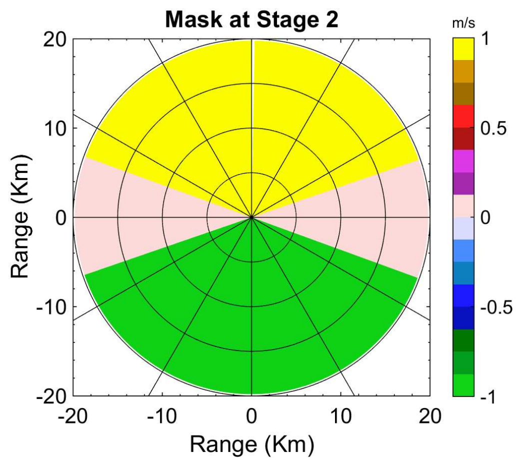

(B) Mask used for unfolding at stage 1

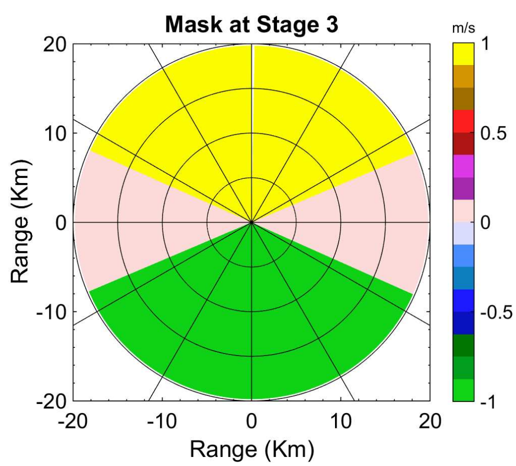

(C) Mask used for unfolding at stage 1

FIGURE 4.18. Correction masks applied at each stage.

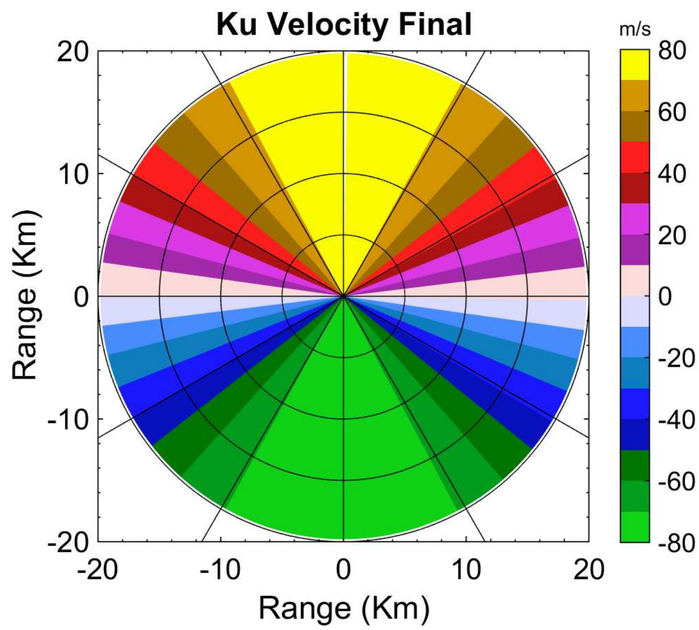

(A) Simulated Ku velocity values after correction

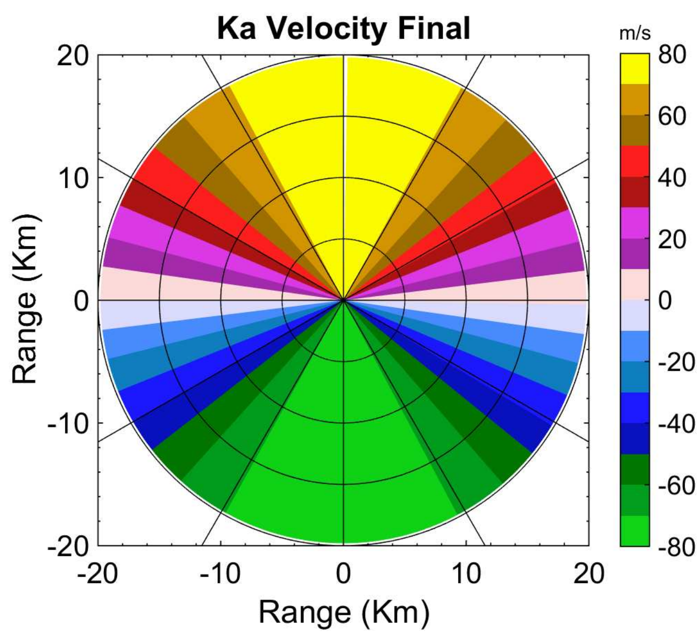

(B) Simulated Ka velocity values after correction

Figure 4.19. Corrected velocities for simulated data.

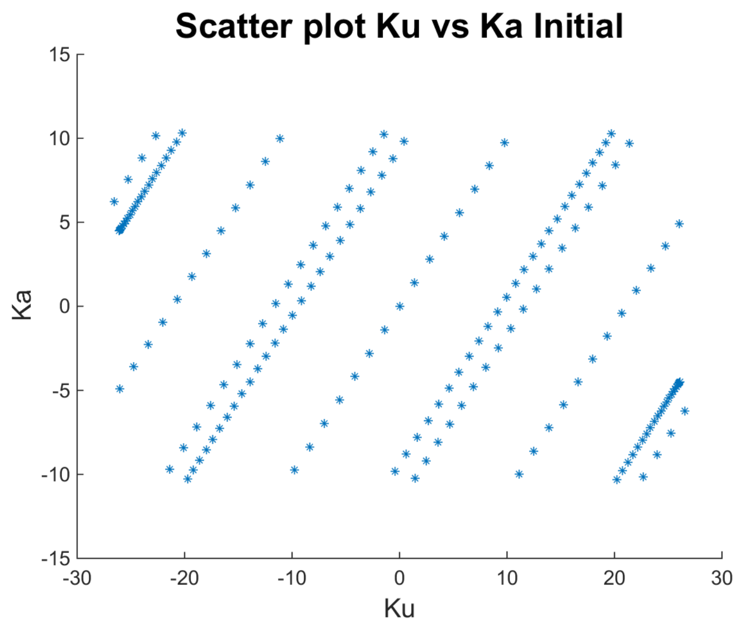

(A) Scatter plot of Ku versus Ka velocity simulated values before correction

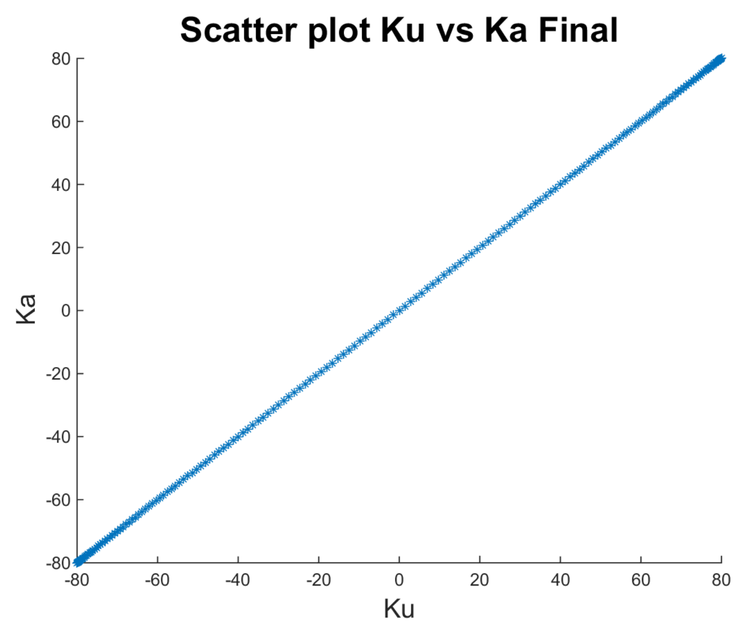

(B) Scatter plot of Ku versus Ka velocity for simulated values after correction

FIGURE 4.20. Scatter plots before and after correction for simulated data.

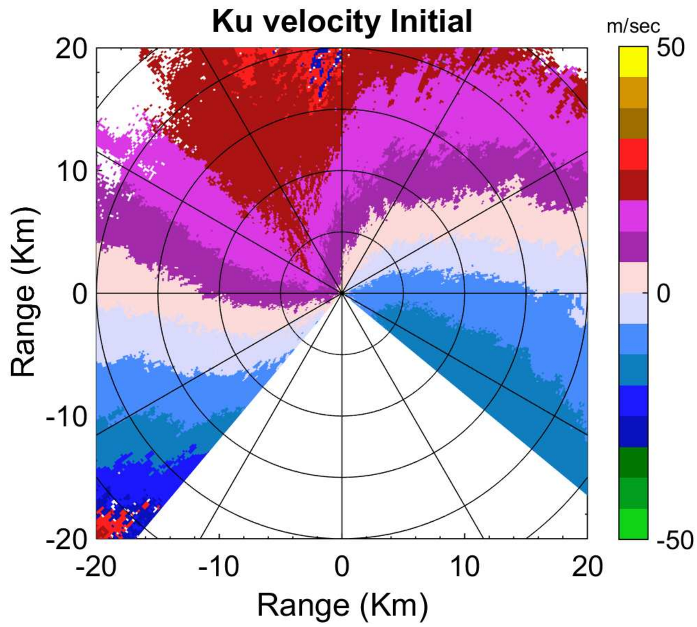

(A) Ku velocity before correction for 3rd December 2015 case.

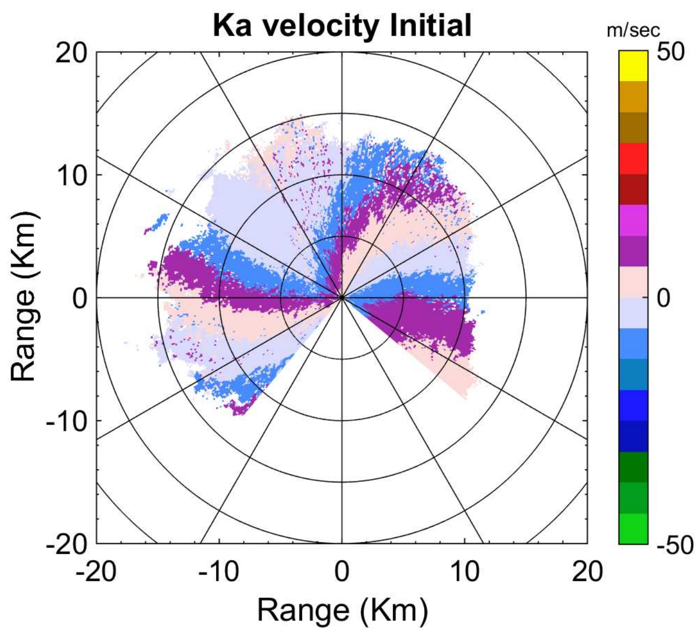

(B) Ka velocity before correction for 3rd December 2015 case.

FIGURE 4.21. Velocities before correction for 3rd December 2015 case.

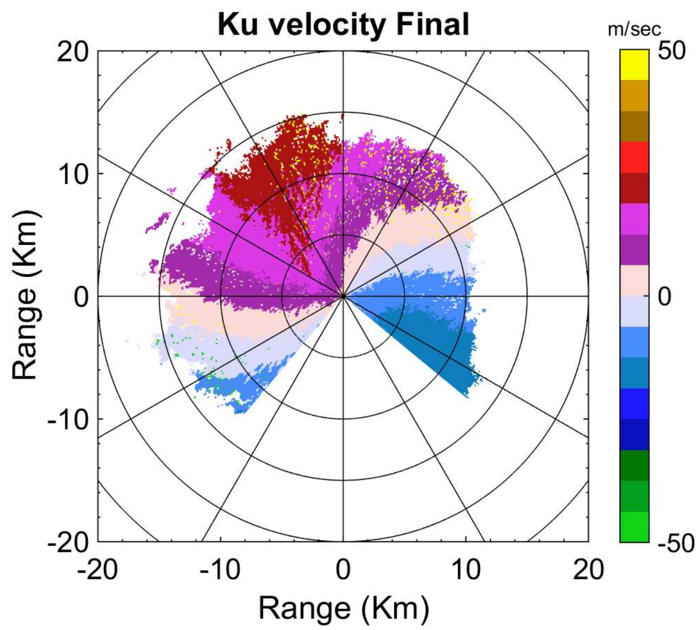

(A) Ku velocity after correction for 3rd December 2015 case.

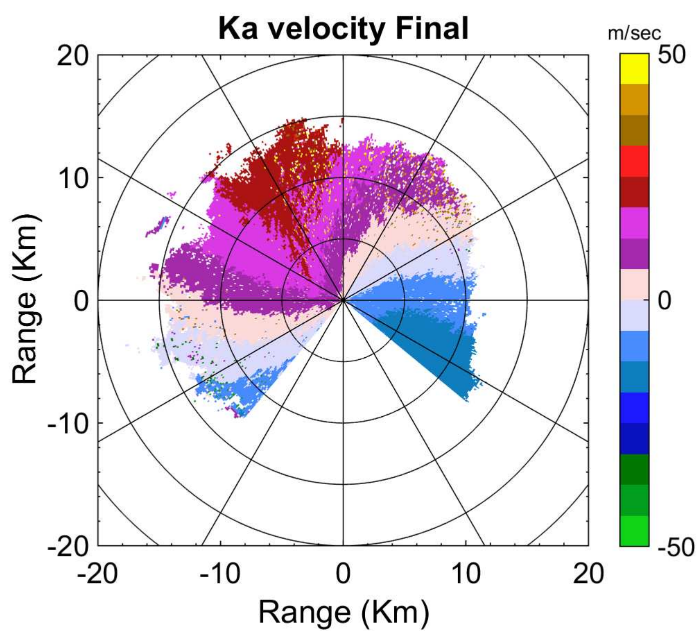

(B) Ka velocity after correction for 3rd December 2015 case.

FIGURE 4.22. Corrected velocities for 3rd December 2015 case.

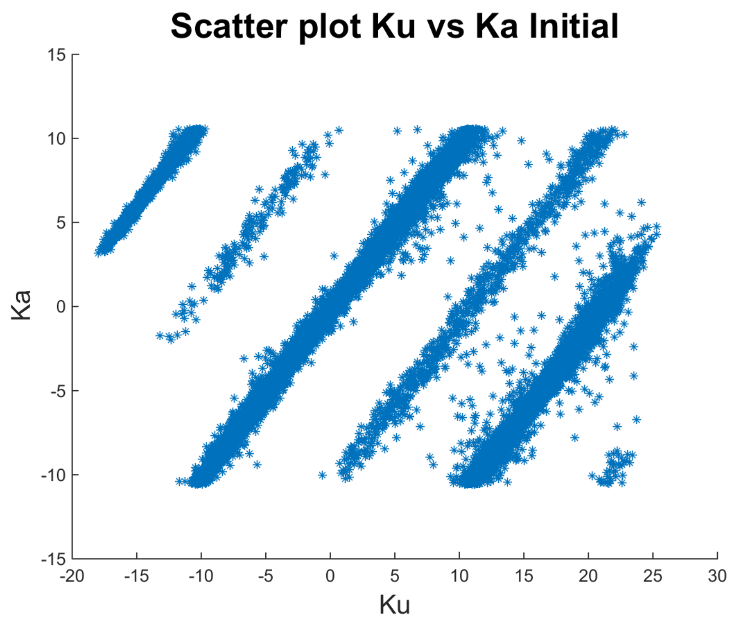

(A) Scatter plot of Ku versus Ka velocity for for 3rd December 2015 before correction

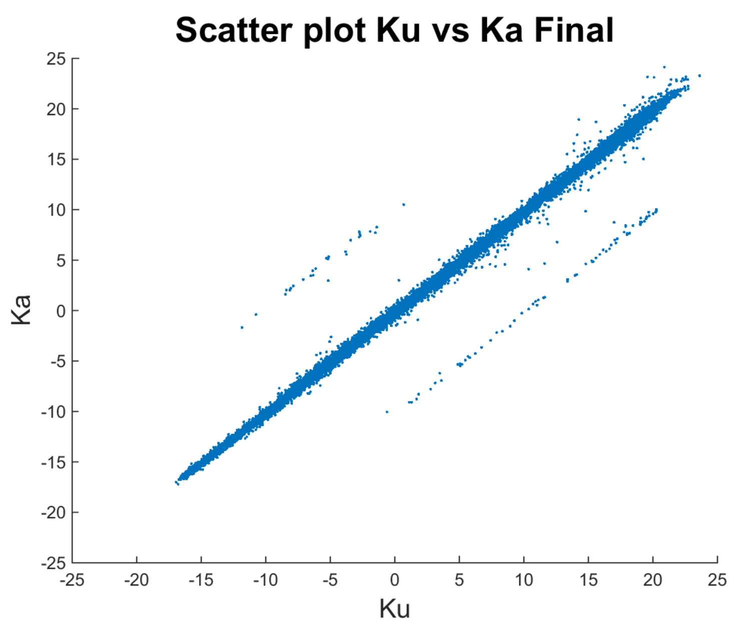

(B) Scatter plot of Ku versus Ka velocity for for 3rd December 2015 after correction

FIGURE 4.23. Scatter plots before and after correction for 3rd December 2015 case.

after correction is shown in figure 4.23. From the scatter plots of data before the correction, we can see the velocity folding which is present in the data and after correction the scatter plot looks good with very few error points.

The second case is taken on 4th March 2017 when the D3R was in Wallops Flight Facility, VA, USA. The D3R was operating in staggered mode of operation with $PRT_1 = 600\mu s$ and $PRT_2 = 400\mu s$, elevation angle of the scan is 0.54 degrees.

Figure 4.24 shows the velocity data from Ku and Ka band before the correction is applied. This is how the velocity moment looks from the output of the D3R signal processor. The unambiguous velocities of Ku and Ka band when operating in staggered mode is 27 m/s and 10.6 m/s; we can see the velocities folding after these values in the figures.

Figure 4.25 shows the velocity data from Ku and Ka band after the correction is applied. The intermediate stages of velocity correction are not shown here. From the figures, we can see that the velocity values of both Ku and Ka have been unfolded to actual velocity values of the storm. We also see that this method will give output in the regions where both Ku and Ka velocities are present. The scatter plots of the velocity data before correction and after correction is shown in figure 4.26. From the scatter plots of data before the correction, we can see the velocity folding which is present in the data and after correction the scatter plot looks good with very few error points.

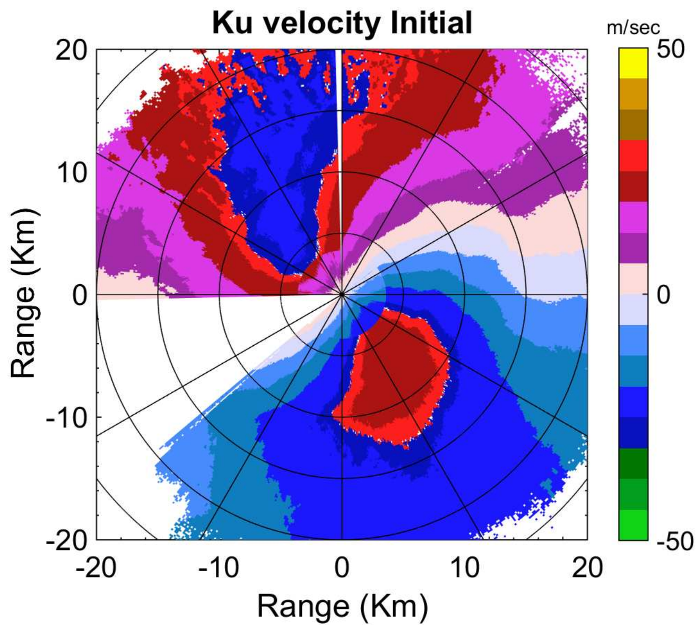

(A) Ku velocity before correction for 4th March 2017 case.

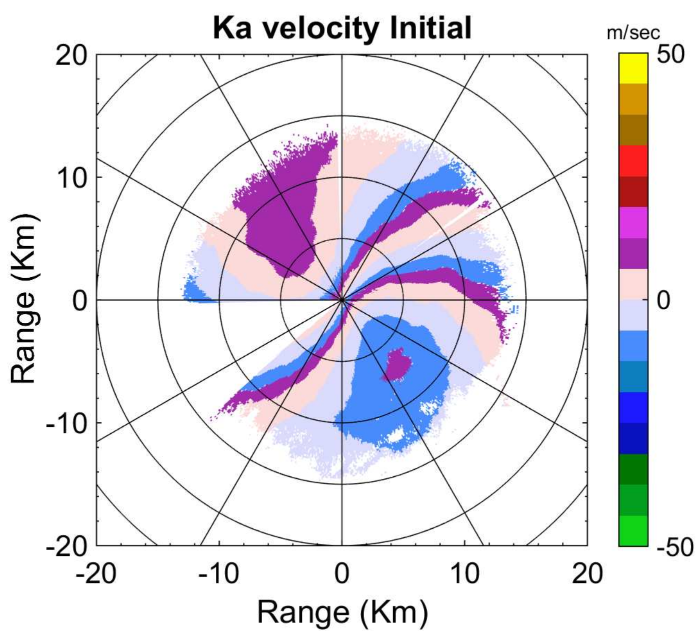

(B) Ka velocity before correction for 4th March 2017 case.

FIGURE 4.24. Velocities before correction for 4th March 2017 case.

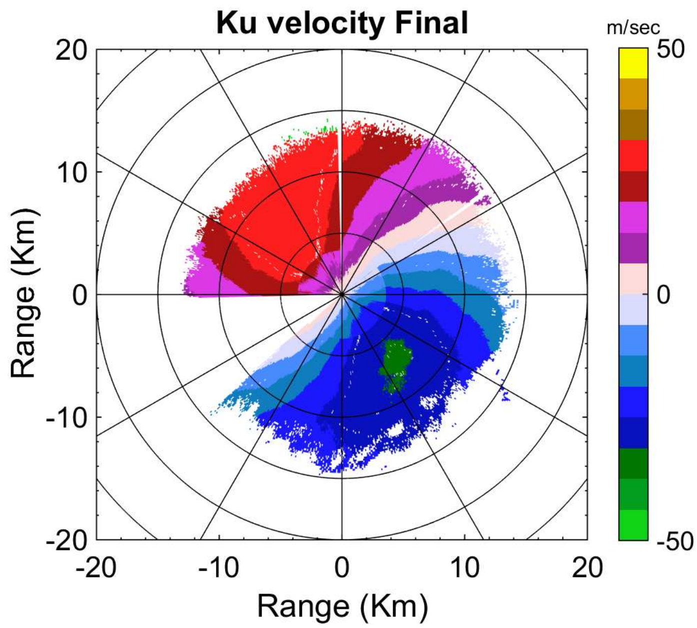

(A) Ku velocity after correction for 4th March 2017 case.

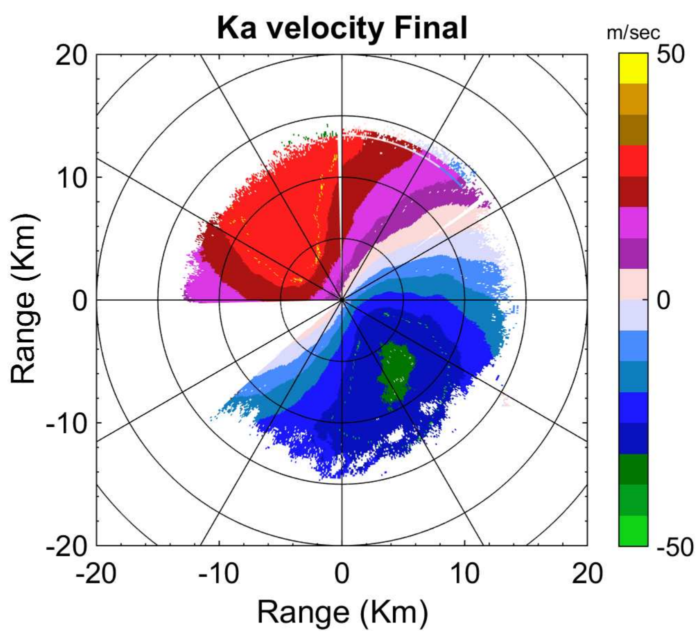

(B) Ka velocity after correction for 4th March 2017 case.

FIGURE 4.25. Corrected velocities for 4th March 2017 case.

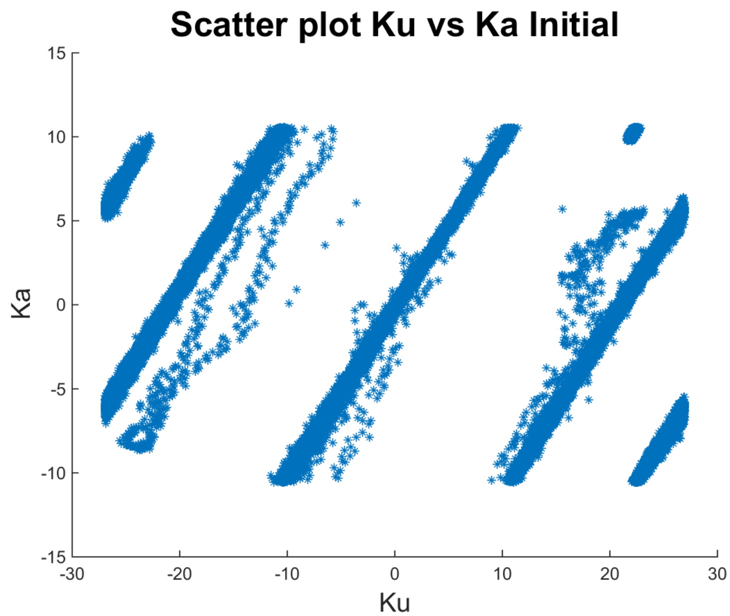

(A) Scatter plot of Ku versus Ka velocity for 4th March 2017 case before correction

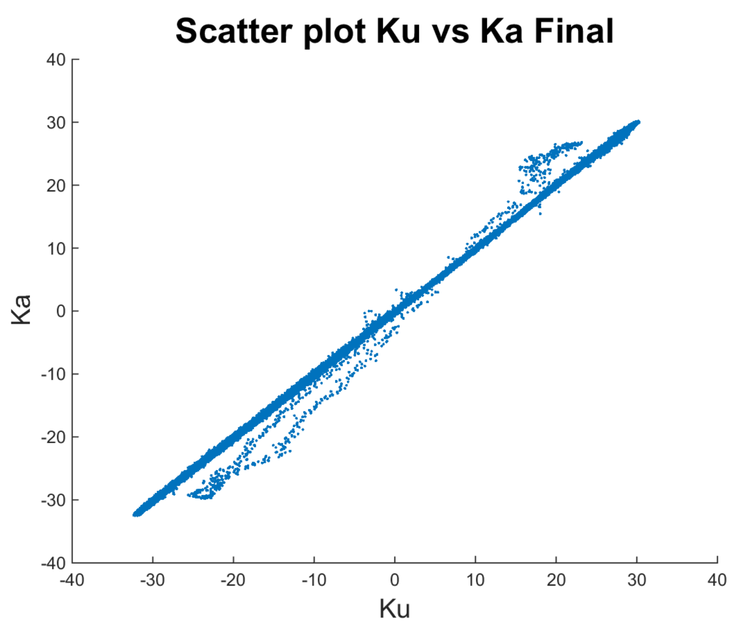

(B) Scatter plot of Ku versus Ka velocity for 4th March 2017 case after correction

FIGURE 4.26. Scatter plots before and after correction for 4th March 2017 case.

Chapter 5

Calibration and first results from D3R after the upgrade

D3R 2.0 was ready for its first deployment outside North America in September 2017. The radar was deployed in International Collaborative Experiment held during the PyeongChang 2018 Olympics and Paralympic winter games (ICE-POP 2018). ICE-POP 2018 was a large field campaign in which science instruments from all over the world were deployed. The main goal of this field campaign was to improve the understanding of the precipitation events on complex terrain and improve the meteorological models. The D3R 2.0 observations will also aid in understanding the evolution of snow clouds utilizing it's dual polarization capabilities.

ICE-POP 2018 was a challenging campaign for the D3R 2.0 because it will be operating in extreme winter conditions. The D3R 2.0 was deployed on the rooftop of Daegwallyeong Regional Weather Office (DGW) in the Daegwallyeong-myeon province of South Korea. The terrain surrounding the radar was complex due to which the radar beam was blocked at low elevation angles. The radar was at a height of 785 m from the sea level. The operational period of the D3R 2.0 for this field campaign was from 30th of October 2017 to 18th of March 2018. During this period the radar captured many interesting rain and snow events, a total of twenty significant events were captured during this campaign.

In this chapter, the calibration exercises which were carried out for the D3R 2.0 before and after deployment in the ICE-POP field campaign is discussed. Next, analysis of some of the snow and rain events which were captured during the field campaign are discussed. Later

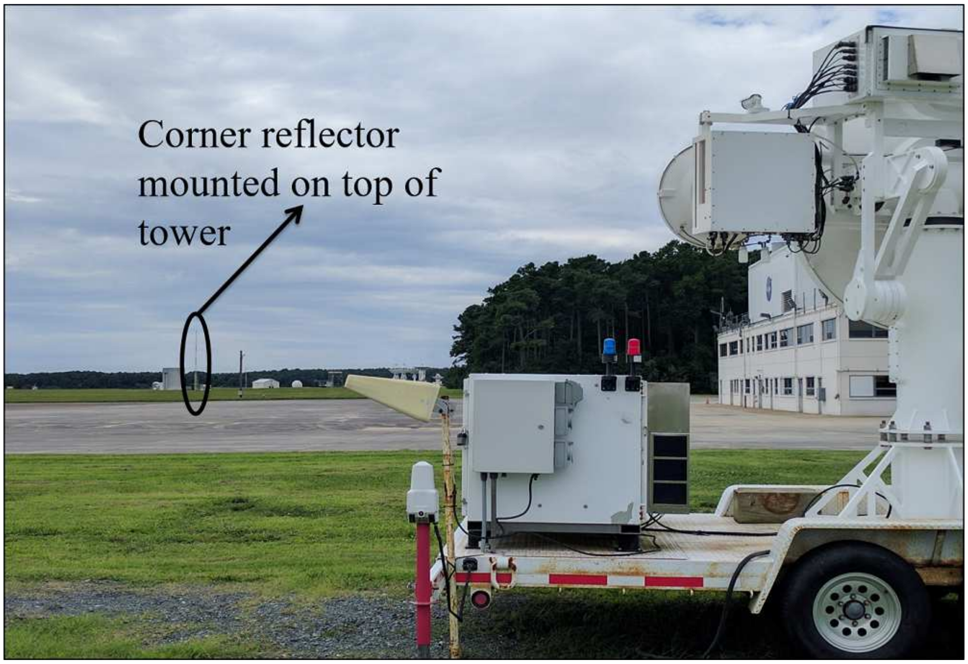

Figure 5.1. Setup of tower calibration.

in the chapter, vertical profile analysis which is helpful in studying microphysics of precipitation will be discussed. Finally, the performance of D3R 2.0 in ICEPOP-2018 campaign is compared with the MxPOL radar which also deployed in the field campaign.

5.1. Calibration of D3R

5.1.1. Tower calibration. The D3R 2.0 went through tower calibration process in late August 2017 at Wallops Flight Facility (WFF) in Virginia, USA. During this calibration procedure, a corner reflector was placed on top of a tower at approximately 480 meters from the radar. The tower height was about 30.5 meters and the radar height was about 2.5 meters. From this information, we can interpret that the radar beam hitting the tower will be approximately 3° in elevation for both Ku and Ka band since both antennas are co-aligned. The tower is equipped with a rotor in azimuth to control the corner reflector direction and azimuth of the tower is approximately 198° with respect to the D3R 2.0. The setup of the tower calibration is shown in figure 5.1.

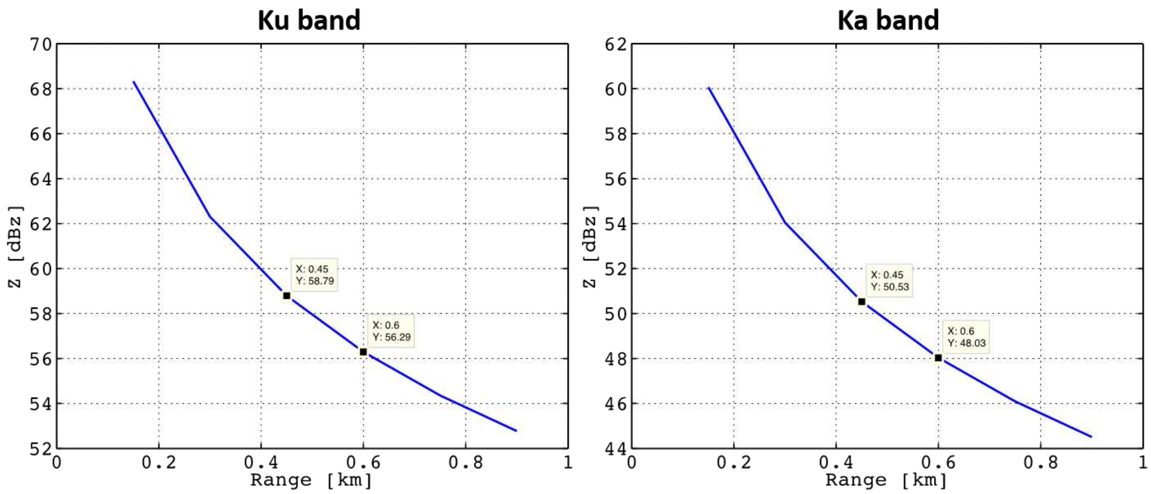

FIGURE 5.2. Expected return power values from corner reflector for Ku and Ka band.

For this calibration exercise, a small trihedral corner reflector having 6.4 inches inside edge dimension was used. The radar cross section of this corner reflector was computed which is then used to compute the expected reflected power from the Ku and Ka band. At a distance of 450 m, -25.4 dBm and -33 dBm are expected at the antenna ports for Ku and Ka band respectively. D3R has a range resolution of 150 m. The expected power return plots for Ku and Ka bands are shown in figure 5.2. Since we know the exact location of the corner reflector from the radar, once the signal is transmitted from the radar, we can pinpoint the exact range bin from which the corner reflector will reflect back the signal to the radar. The system parameters of the radar are measured and adjusted to get the maximum signal strength. The results of returned power from the tower calibration exercise for Ku and Ka band is shown in figure 5.3. From the results, we can see that we are getting signal levels close to the expected values.

5.1.2. ANTENNA CO-ALIGNMENT CALIBRATION. Co-alignment calibration between the Ku and Ka band antenna is important to get accurate data. Sun is used as a reference point and the co-alignment between the Ku and Ka band antennas is checked. Shims on

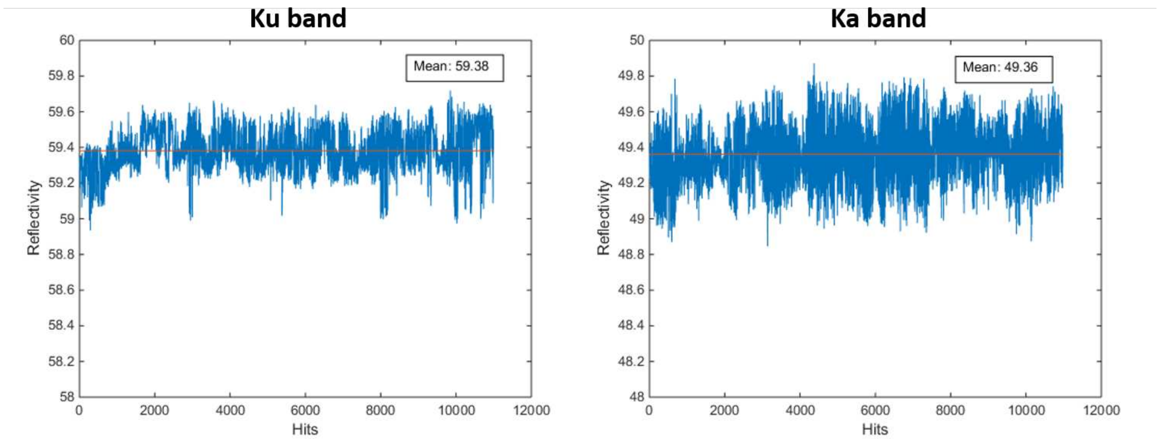

FIGURE 5.3. Actual return power values from corner reflector for Ku and Ka band.

the four antenna mount points can be adjusted to match the alignment between the two antennas. Once the adjustment is done the co-alignment is checked again with the sun as the reference. This process is repeated until we get the best co-alignment between the Ku and the Ka bands. During the ICEPOP campaign, the antenna co-alignment was checked periodically. The result of antenna co-alignment exercise carried out on December 04, 2017 is shown in figure 5.4. The 3 dB contours seen in the figure are generated from a second order polynomial surface fitted to the received power. If the Ku and Ka antennas are perfectly co-aligned the contour rings will be concentric. From the result shown in figure 5.4 we can see that the D3R 2.0 azimuth and elevation are co-aligned to within 0.15 degree and <0.1 degree respectively. Since we know the exact location of the sun during a particular time of the day, this calibration exercise is also used to adjust the azimuth of the radar with respect to true north when deployed in a new location.

5.1.3. Calibration of Polarimetric variables. The D3R 2.0 data will be used for science and research; it is important to regularly calibrate and check the polarimetric variables obtained from the radar. Since D3R 2.0 uses short and medium pulse, the starting differential phase (ϕ_{dp}) value of both these pulses may be different. This will appear as a

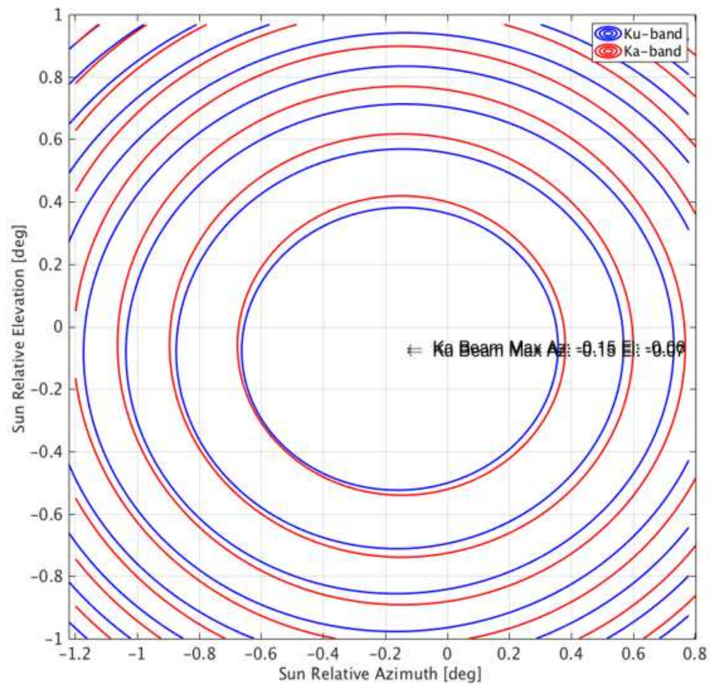

FIGURE 5.4. The solar observations from December 04 2017 to verify the antenna co-alignment.

discontinuity in data at the output. With careful calibration, these discontinuities can be removed by comparing the ϕ_{dp} values for the same range gates for short and medium pulse in light rain or moderate rain event. ϕ_{dp} of either of the two pulses can be adjusted to gain continuity. The phase wrapping is then removed if any by measuring the starting ϕ_{dp} at range zero. The correction for phase wrapping is applied for both short and medium pulse.

Differential phase (Z_{dr}) is another polarimetric variable which is sensitive to changes in system parameters between H and V polarization channels. The Z_{dr} calibration is performed by taking vertical pointing data, the mean Z_{dr} for the vertical pointing data should be 0 dB in light or moderate rain event. The offset from this value is measured and applied for the short pulse data. Then the common range bins are taken for the short and medium pulse and corrected for discontinuities.

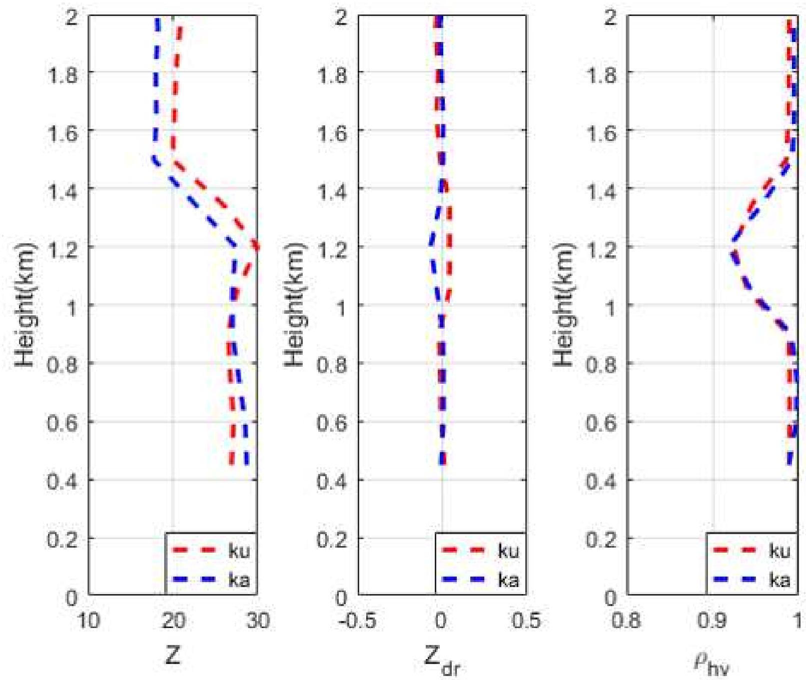

FIGURE 5.5. Calibration check using birdbath scan performed in light rain at 07:32 UTC on November 10 2017

5.1.4. CALIBRATION CHECK OF THE DATA. Regular calibration checks were carried out in ICE-POP 2018 using the data collected by the radar. Birdbath scan data is used to check the quality of the radar data. A birdbath scan data from 10th November 2017 at 07:32 UTC is shown in figure 5.5. From the figure, it can be seen that the differential reflectivity bias is approximately 0 dB for both Ku and Ka band. It can also be seen that around 1.2 km a melting layer is present and the reflectivity and co-polar correlation values are as expected for both Ku and Ka bands. If necessary, the parameters of the radar will be adjusted and the calibration check will be carried out again.

5.2. ANALYSIS OF DATA COLLECTED IN ICE-POP

During the ICE-POP 2018 campaign, many interesting events were captured by the D3R 2.0. The data from the radar aided the local agencies to predict snow which could not be detected by other radars due to complex terrain. On 28th February 2018, there was a huge snow storm in the PyeongChang region. Around 42 cm of snow was accumulated during a single snow event. RHI plot from the same day at 11:25 UTC is shown in figure 5.6. From the figure, it can be seen that the reflectivity values are extending up to 8 km in height. It is also seen that the reflectivities as low as 0 dBZ are observed when we have good SNR data. The co-polar correlation values are close too unity. A significant differential phase shift is observed as we go in range from the radar, this feature clearly indicates the radar beam is going through big scatterers, indicating ice or snow. We also have differential reflectivity, specific phase and spectral width data from which the characteristics of the hydrometers can be determined. Using this RHI data the microphysics of precipitation particles can also be studied.

5.2.1. Attenuation Correction. Weather radars operating at higher frequency bands are more prone to have attenuation in the rain. D3R 2.0 operating at Ku and Ka bands is also suffered by attenuation during rain events. The attenuation in Ka band is more compared to the Ku band and attenuation increases along the range going away from the radar. Attenuation correction must be implemented to map the exact values from the radar.

Previous work in attenuation correction are based on the empirical relationship between attenuation and reflectivity values. These methods are severely affected by measurement errors and bias in the radar system. Attenuation correction methods based on dual-polarization information have proven good results. D3R 2.0 employs a robust attenuation correction algorithm [26] based on dual-polarization measurements from the data to correct the reflectivity and differential reflectivity moments. Attenuation correction results from an RHI case from D3R 2.0 Ku band on 10th November 2017 around 07:34 UTC is shown in figure 5.7. In the figure, the plots on the left side are the moments without any attenuation correction and on the right side are the moments after attenuation correction is done. We can clearly see from

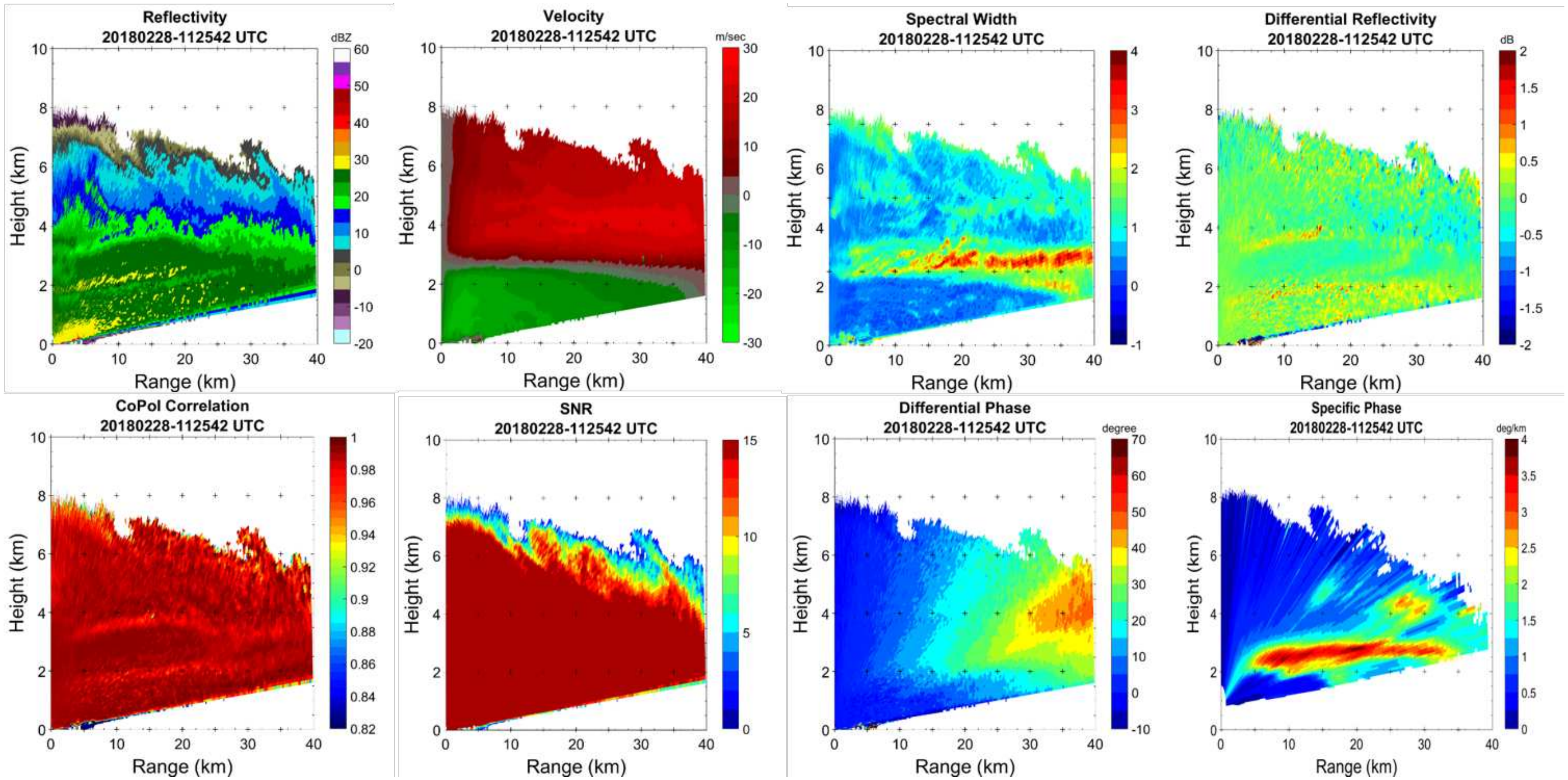

FIGURE 5.6. Moment data from D3R 2.0 Ku band for 18th February 2018 snow case.

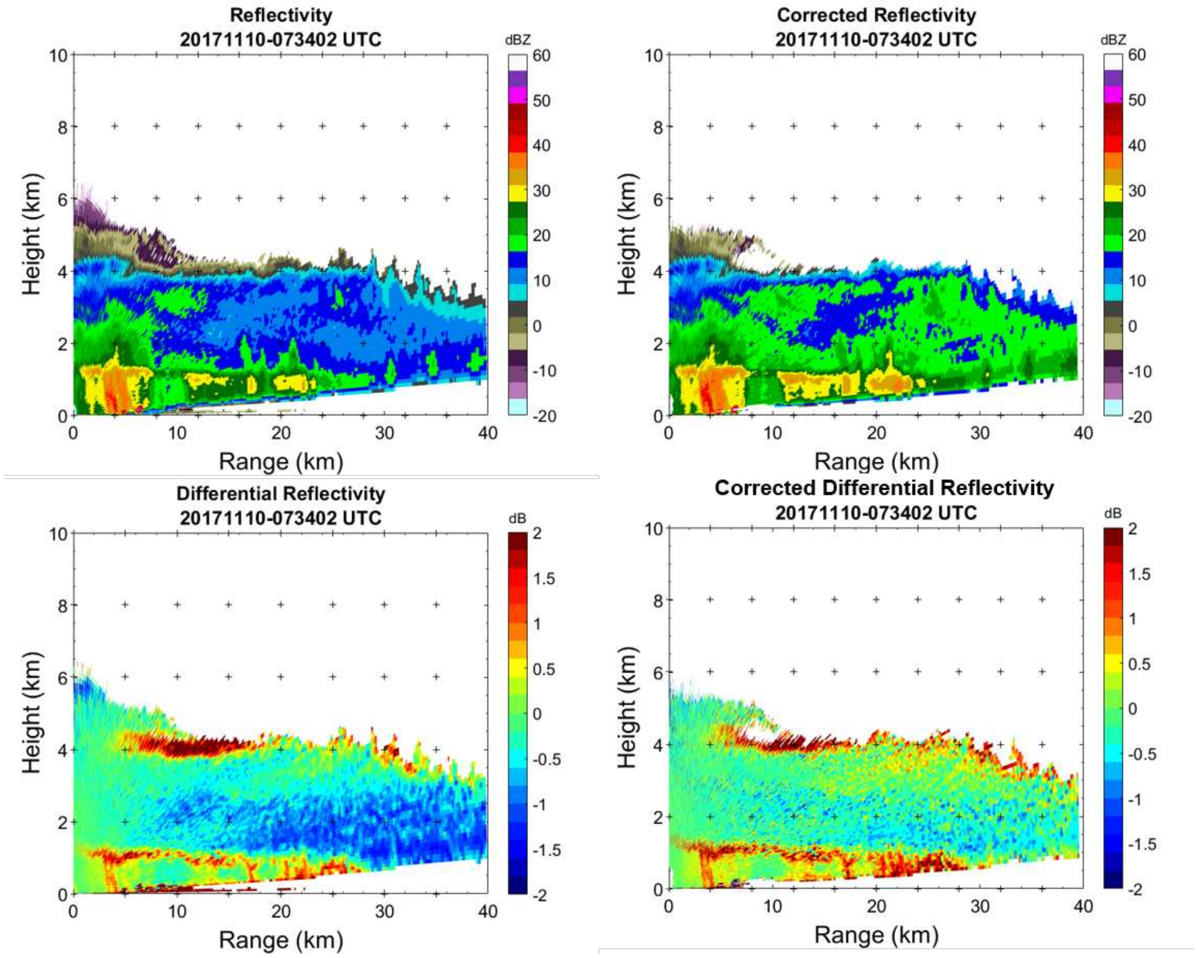

FIGURE 5.7. Attenuation correction results for D3R 2.0 Ku band on 10th November 2017 at 07:34 UTC.

the figure that the attenuation correction for the moments will aid in interpreting the data correctly.

5.2.2. PRECIPITATION CLASSIFICATION. Precipitation classification is an important derived product in radar meteorology. Most of recent precipitation classification schemes are based on fuzzy logic. When the radar observations are noisy at the input, the classification output obtained might be inaccurate, since the classification process is bin based and the information from neighboring radar cells is not considered. An improved classification methodology is used in D3R 2.0 [27]. The precipitation classification output for a rain case from D3R 2.0 Ku band on 10th of November 2017 is shown in figure 5.8. In this figure, it can

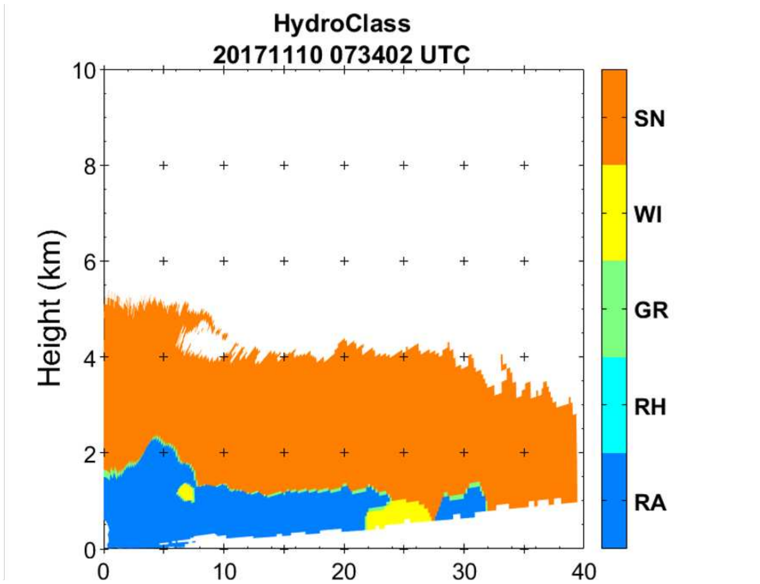

FIGURE 5.8. Precipitation classification result for D3R 2.0 Ku band on 10th November 2017 at 07:34 UTC.

be seen that the melting layer is around 1.5 km. The algorithm is classifying precipitation as rain below the melting layer and above the melting layer it is classifying as snow which is the usual trend in any rain event. Another case for precipitation classification for a snow event from D3R 2.0 Ku band on 28th February 2018 is shown in figure 5.9. In this figure, we can see the algorithm classifying the precipitation as snow, which is correct.

5.3. Analysis of data to study microphysics

5.3.1. CASE 1: Rain event.

A rain case from the D3R 2.0 Ku band on 10th November 2017 at 7:34 UTC is considered here. Vertical profile of data is taken from RHI scan at an azimuth angle of 299.91 degrees and at 4 km range. Various dual-pol moments are shown in figure 5.10. From the figure, it can be seen that the precipitation classification is classifying the data as rain from the lowest height until 1.4 km in height and then light rain till 2 km in height. We can observe that the co-polar correlation values decrease and differential

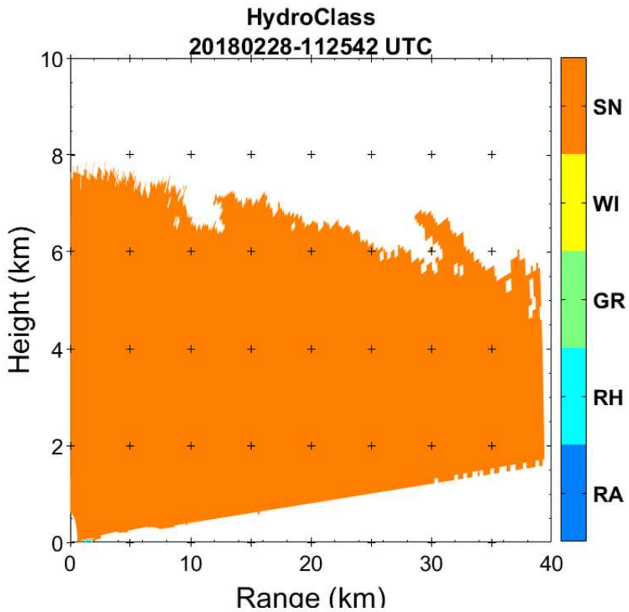

Figure 5.9. Precipitation classification result for D3R 2.0 Ku band on 28th February 2018 at 11:25 UTC.

reflectivity values increase around 1.1 km these features are typically seen in the melting layer region. The classification of light rain may be due to small drops measured above the melting layer; this might indicate the presence of super cooled liquid water contents above the melting layer. Above 2 km in height, the reflectivity values decrease with low differential reflectivity (indicates vertically oriented particles) and high co-polar correlation can be seen, these features indicate the features of ice-crystals. The precipitation classification algorithm output also indicates ice crystals above 2 km height. This is an interesting case because we can see precipitation classification of rain above the melting layer which might be due to super cooled liquid water content which is not common.

5.3.2. CASE 2: Snow event. A snow case on 28th February 2018 at 11:25 UTC is considered here. Vertical profile of data is taken from an RHI scan data with an azimuth angle of 51.36 degrees and at 10 km range. Various dual-pol moments for this vertical

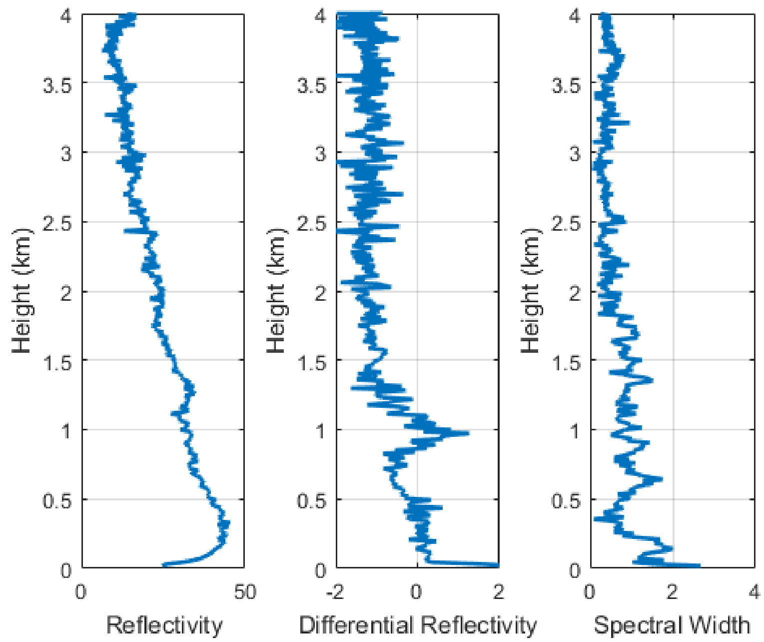

(A) Vertical profiles of reflectivity, differential reflectivity and spectral width.

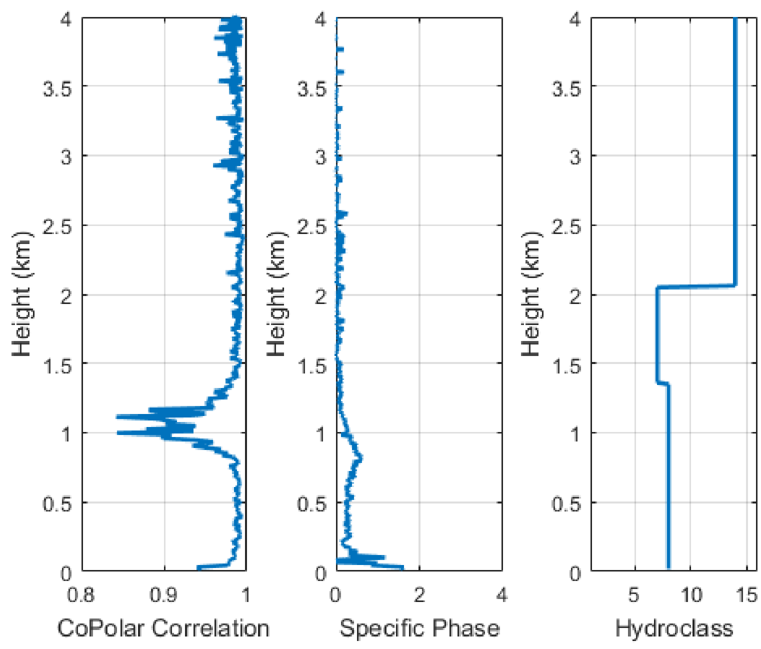

(B) Vertical profiles of co-pol correlation, specific phase and precipitation classification

FIGURE 5.10. Vertical profile analysis 10th November 2017 case

profile are shown in the figure 5.11. From the figure, it can be seen that the precipitation classification output is dry snow from 0.5 km to 1.5 km. In this region the reflectivity value is around 25 dBZ, differential reflectivity value is low, co-polar correlation value is high around 0.99, and the specific phase value is low. These characteristics match with the characteristics of dry snow. Going further in height the dry snow changes to dendrites this is observed with an increase in specific phase values. Around 1.8 km it can be seen that the precipitation classification indicate dendrites. This is matching the features of the dendrites which have a drop in correlation as the specific phase increases and also the reflectivity drops down by a few dBZ. After 2 km in height, it can be seen that the dendrites are disappearing and dry snow taking over, this can be matched with features of dry snow. After 4 km in height, it can be seen that the reflectivity drop occurs with high co-polar correlation and low specific phase which are the signatures of ice crystal region, the precipitation classification output confirms ice-crystals in this region. In this case, we can see that dry snow dominates the lower part of the storm, some dendrites present from 1.5 km to 2.2 km approximately in height indicates microphysical process was happening at this height, then as we go in height dry snow dominates and crystals appear after 4 km.

5.4. Comparison with MxPOL radar

In ICE-POP 2018 field campaign, various science instruments were brought together from around the world. The D3R 2.0 data quality was compared with other science instruments in the campaign. The MXPol X-band dual-polarimetric radar which operates at a frequency of 9.41 GHz was set up at the Gongneung-Wonju National University site. This site was located at a distance of 16.9 km from D3R 2.0 as shown in figure 5.12. The height from the sea level to the D3R 2.0 radar was 785 m and the height from sea level to the MXPol radar was 66

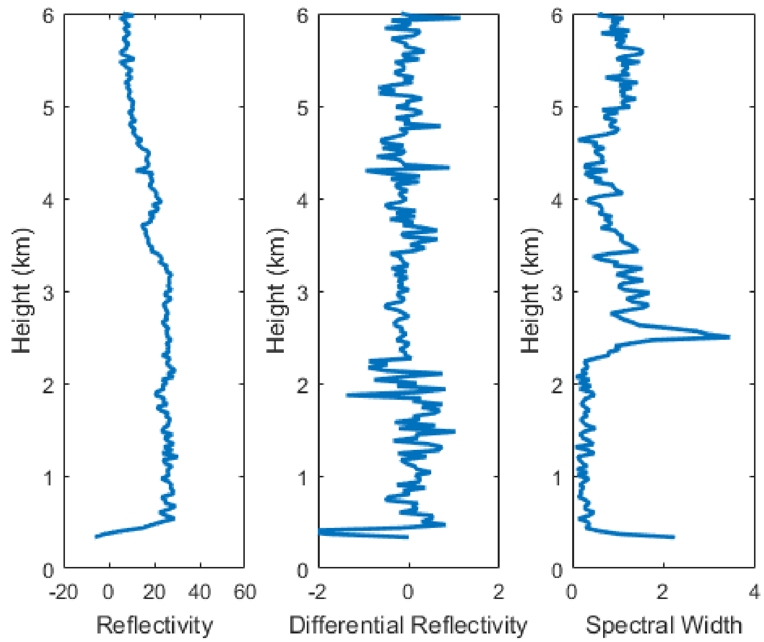

(A) Vertical profiles of reflectivity, differential reflectivity and spectral width.

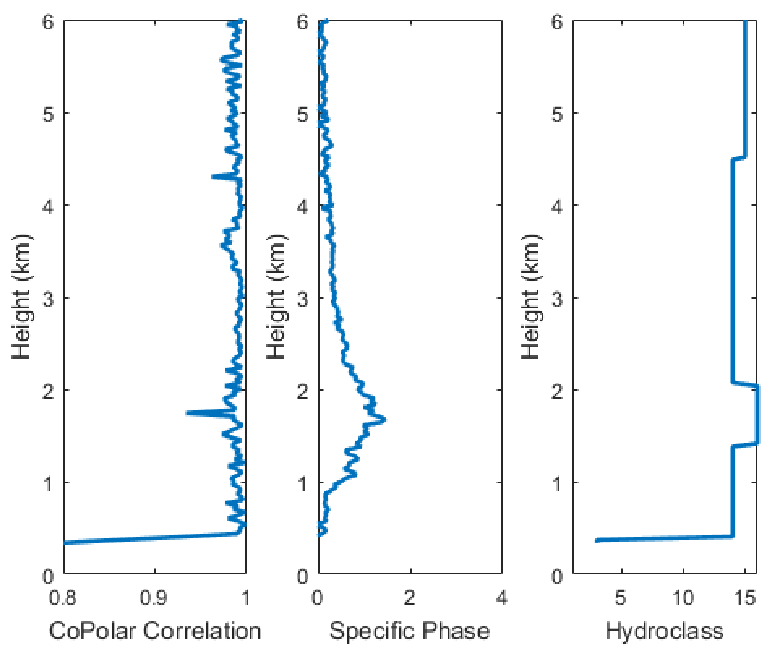

(B) Vertical profiles of co-pol correlation, specific phase and precipitation classification

FIGURE 5.11. Vertical profile analysis for 28th February 2018 case

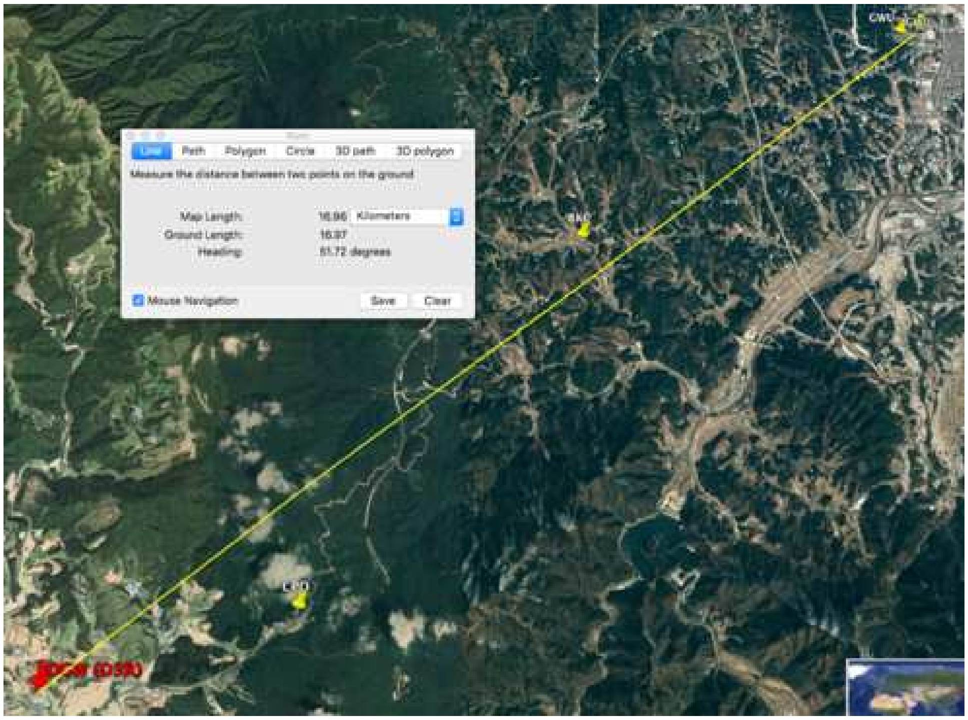

FIGURE 5.12. Locations of the D3R 2.0 and MXPol radar.

m. This big difference in height was because the D3R 2.0 was deployed on the mountains in Daegwallyeong region and MXPol was deployed in the coastal region of Gangneung. The terrain between the two radars is complex, with mountains present between them. The minimum elevation angle for the D3R 2.0 to clear the beam blockage in the direction of MXPol was 3.27 degrees.

A PPI scan is considered here from D3R 2.0 Ku band and MXPol during a snow event on 28th February 2018 around 12:31 UTC to compare the moments from both the radars. The elevation angle of PPI scan of D3R 2.0 was 4.88° and the elevation angle of the MXPol was 6°, the azimuth angle for D3R 2.0 was 53° and the azimuth angle for MXPol was 233° to be in the line of sight with each other. The common observation volume diagram for D3R 2.0 and MXPol is shown in figure 5.13. From this figure, it can be seen that the common volume of overlap is between 5.2 km and 7.2 km, with range starting from D3R 2.0.

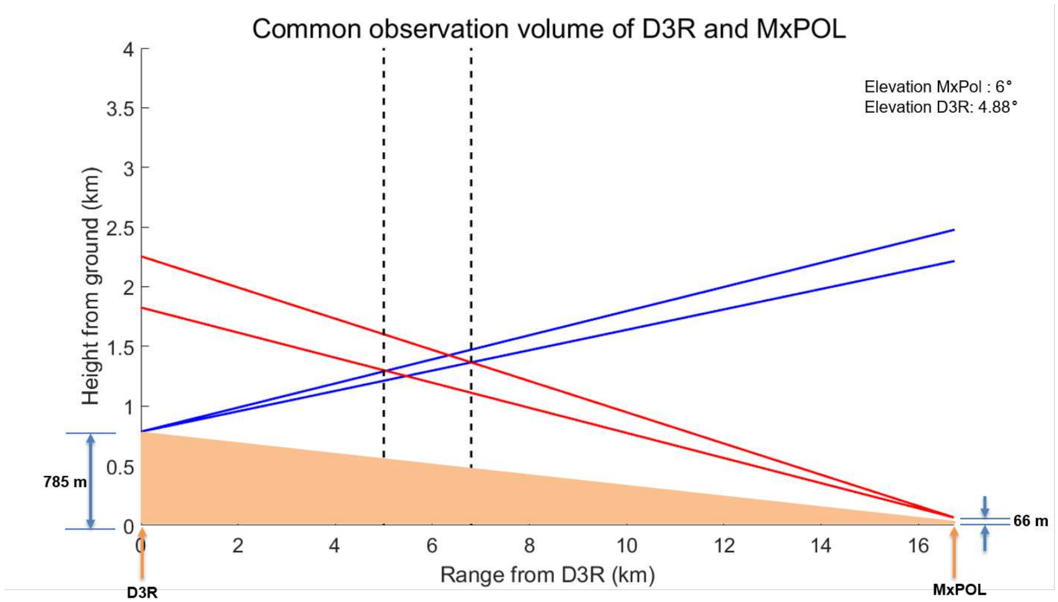

FIGURE 5.13. Common observation volume of the D3R 2.0 and MXPol radar.

Figure 5.14 shows the reflectivity ray plot versus range from D3R 2.0; the blue line indicate the reflectivity measurements from D3R 2.0 Ku band and the black line indicates the reflectivity measurements from MXPol. From the figure, it can be seen that in the common observation volume region the reflectivities of both D3R 2.0 and MXPol are matching very well. Attenuation correction is not considered since it was a snow event.

Another case is considered for comparison in this an RHI scan of D3R 2.0 Ku band is considered and compared with MXPol radar. Data from 28th February 2018 around 11:25 UTC is considered. This was an interesting case to compare since both the radars are at different heights from the sea level and the RHI plots start at different heights. The azimuth angle for D3R 2.0 was 51.4° (53° is the exact angle in the line of sight with MXPol) and the azimuth angle for MXPol was 233°. We can see from these plots that reflectivities from both the radars are matching well. An interesting observation from these plots is that we can see the melting layer around 0.8 km in height from the MXPol radar. The D3R 2.0 is not detecting this melting layer because of the difference in radar heights and radar beam

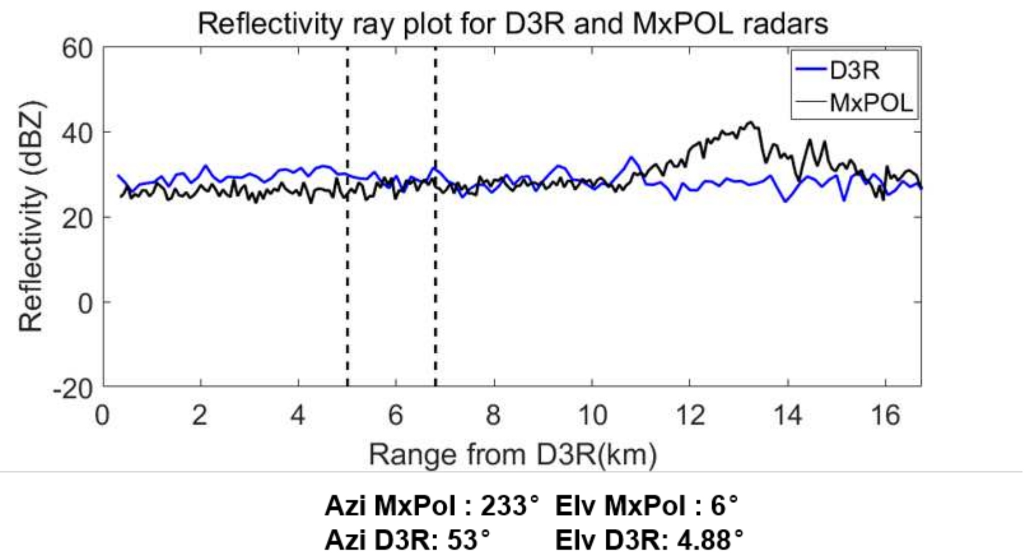

FIGURE 5.14. Reflectivity ray plot of the D3R 2.0 and MXPol radar for 28th February 2018 case.

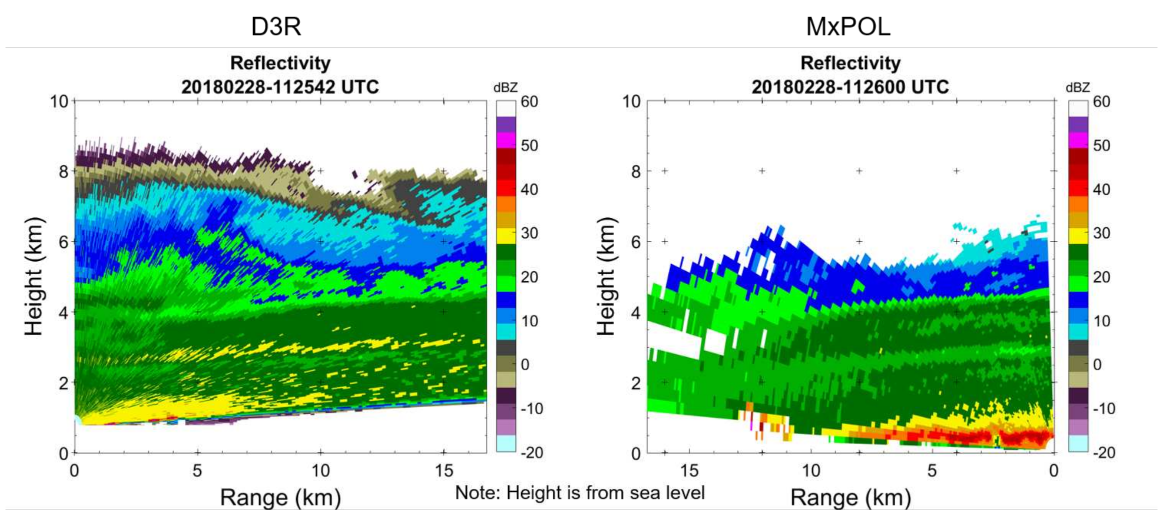

FIGURE 5.15. RHI comparison of the D3R 2.0 with MXPol radar for 28th February 2018 case.

doesn't encounter the melting layer. Since D3R has a higher sensitivity, we can see the data up to 8 km in height with good spatial resolution. This case explains the need for many short range radar network when having a complex terrain. Overall from the two figures, we can see that the D3R data quality was excellent.

Chapter 6

Summary and future work

6.1. Summary

Weather radars measure signal backscattered from precipitation particles in a resolution volume. A pulsed Doppler weather radar transmits a train of pulses and the received samples can be viewed in range-time and sample-time. This received signal from the radar is a complex stochastic signal. The power spectral density of the stochastic signal will provide the decomposition of the signal power into various frequencies. The distribution of the particles in a precipitation event is assumed to be Gaussian. Radars operating with polarization diversity can transmit and/or receive two orthogonally polarized signals at the same time. Horizontal and vertical polarizations which are orthogonally separated are employed by the radars. Using the information from the signal characteristics of the horizontal and vertical received signals we can determine the particles size, shape, type and orientation in the resolution volume. The received voltage levels which are mapped to the backscattering matrix, from which various radar moments such as equivalent reflectivity factor, velocity, differential reflectivity, differential phase shift and co-polar correlation are computed.

Dual-frequency dual-polarization Doppler Radar (D3R) was developed as a ground validation tool for the DPR radar which is on the GPM core satellite. D3R operating at Ku and Ka frequency bands have higher sensitivity and can measure light rain and snow. Dual-frequency measurements aid in computing drop size distribution and understanding the characteristics of precipitation medium. In the past years, D3R has participated in several field campaigns across North America. The data from the campaigns were used for multiple purposes ranging from ground validation to input for hydrological models. The campaigns in which D3R took part were Mid-latitude Continental Convective Clouds Experiment (MC3E), GPM Cold-season Precipitation Experiment (GCPEx), Integrated Precipitation and Hydrology Experiment (IPHEx), Iowa Flood Studies (IFloodS) and Olympic Mountain Experiment (OLYMPEx).

A compact and transportable system was achieved for the D3R by using efficient and state of the art technology. Solid state transmitters are used with a peak power of 200 W for Ku band and 40 W for Ka band. In addition to dual-polarization moments, D3R's derived products include attenuation corrected variables, specific-phase and precipitation classification. With an operating range of approximately 40 km, the D3R can operate in uniform PRT mode and staggered PRT mode. The D3R also has the capability of operating in the alternate mode in addition to simultaneous mode, the added advantage of this mode is that we can get the linear de-polarization ratio output.

The system architecture of the D3R can be broadly divided into two sections; non-rotating and rotating sections. The rotating sections consist of the antenna, transmitters, waveform generator, IF electronics and the digital receiver. The antennas of Ku and Ka reside on an antenna frame; these antennas are linearly polarized prime focus parabolic reflector type. The antennas are co-aligned so that they scan the same resolution volume. The IF electronics along with waveform generator and digital receiver are packed inside a temperature controlled IF box. All the rotating system are attached on to the antenna pedestal. The non rotating systems consist of the generator, UPS, signal processing servers and storage servers. These non-rotating systems are housed inside temperature controlled enclosures. The whole D3R system is placed on a trailer which can be adjusted accordingly to get a precise leveled system. DR3 has a specialized software running on it. The D3R software has the capabilities of signal processing, timeseries and NetCDF file generation and storage. The software also provides a real time display. The major advantage of the software architecture is that all the sub-systems are networked such a way that the radar operator can control these sub-systems through an internet connection to the radar. If a fault is detected in a sub-system, it can be remotely debugged and power cycled if necessary.

D3R went through an upgrade to enhance it's features and provide more flexibility for research. The upgrade was carried out between August 2016 and September 2017. The hardware modifications and changes were discussed with the help of the block diagram of the system. The up-converter and down-converter chain were redesigned for both Ku and Ka bands, this design process was explained in detail. The mixer, amplifier and interface board layout design and the realized board were shown. The integration of components on to the PCB board was accomplished using infrared IC heater at CSU. The revised IF frequency plan was accomplished and implemented. The clock box which houses all the components required for synthesis of different frequencies was shown. Configuring the digital receiver FPGA was also discussed. The changes in the software of the D3R were discussed briefly.

A brief overview of the mechanical aspects of the system design was given. The enclosures which houses the PCB boards and the IF boxes were shown. An overview of Waveform design aspects which were implemented in the D3R 2.0 was given. Further approaches for designing the waveform and filtering the signal were discussed. The system sensitivity was compared to that of the old system, from this we could see the improvement in sensitivity with the upgraded D3R. The preliminary stages of hardware integration were tested at CSU. The final upgraded hardware was bench tested at GSFC and then integrated at WFF. The whole upgrade for the radar was carried out in two stages. First, the Ku system was upgraded and then the Ka system was upgraded.

The range-velocity ambiguity associated with the pulsed Doppler radar limits maximum unambiguous range (r_a) and maximum unambiguous velocity (v_a). Both r_a and v_a are dependent on the pulse repetition frequency of the radar. The v_a is also dependent on the frequency of operation of the radar. With a lower r_a we have more probability of encountering second trip echoes. It is challenging to detect and mitigate the second trip when the second trip signal overlaps with the first trip signal. Many methods have been developed to mitigate the range-velocity ambiguity to an extent. Some of the methods use the concepts of staggered PRT, dual PRF and phase coding schemes. The staggered PRT or dual PRF is also used to dealias the second trip signals into their corresponding range bins. When using phase coding schemes in the radar, the transmitted pulses are coded using systematic and random codes. The methods for getting the first trip and second trip moments when using phase codes was explained. From simulations of random and SZ phase codes for estimating second trip moments, we can see that SZ codes perform better than random phase codes. Also, it is seen that as we go higher in frequency the recovery region for second trip becomes narrow, this poses a challenge for detecting and estimating second trip echoes at higher frequencies.

Based on the concepts of staggered PRT and random phase codes, an algorithm was developed to characterize and mitigate the second trip echoes in D3R. This method also places the second trip echoes in their respective range bins using the information from staggered PRT. The performance of the method to characterize and mitigate the second trip echoes was shown using data from D3R. The algorithm performed well in characterizing and mitigating the second trip echoes; the second trip echoes were also put correctly in their respective range bins. The estimation of second trip is inaccurate when first and second trip signal overlap, this is a limitation of using random phase codes.

Weather radars operating at higher frequency have small v_a, folding of velocity values can be observed if the velocity values exceed v_a limit. A method to unfold the velocity components for the D3R was explained. Since D3R is a dual-frequency radar, the radar scans the same resolution volume at the two frequencies; this information can be used to dealias the velocity components of both the frequency bands. The method was explained using simulated signals and the performance of the method was discussed using the data from D3R. This velocity ambiguity mitigation method will be helpful in observing storms which have high velocities.

D3R 2.0 was deployed in ICE-POP 2018 field campaign in South Korea. This was the first campaign for the radar outside the North American continent and also the first campaign after the upgrade. Calibration procedures which were carried out for D3R 2.0 were explained in detail. Tower calibration using a corner reflector was done prior to deployment of the radar to ICE-POP 2018. Antenna co-alignment calibration was done regularly by observing the sun and computing the offset between the Ku and Ka band antennas. Calibration of other polarimetric variables which were done was also explained. The results from the D3R 2.0 for rain and snow events during the ICEPOP 2018 field campaign were discussed. Various derived moments were discussed in detail. Vertical profile analysis was studied to understand the microphysics of precipitation. Finally, the performance of D3R 2.0 with respect to other instruments in the field campaign was shown.

6.2. Future work

Different phase coding schemes will be implemented in D3R 2.0 and their performance in handling the range ambiguity will be studied. Orthogonal phase codes which lead to better cross-polarization measurements and Walsh-Hadamard coded waveforms for retrieving LDR can be implemented and researched. Software for the D3R will be modified to dynamically handle the control signals for the radar from the user. Also, the signal processor will be modified to handle complex modes of operations which D3R 2.0 is capable of in future.

Bibliography

[1] M. A. Vega, *Multi-frequency dual-polarized platform for validation of satellite precipitation measurements*. PhD thesis, Colorado State University. Libraries.

[2] Pentek Inc, *3-Ch. 200 MHz A/D, 2-Ch. 800 MHz D/A, Virtex-6 FPGA - XMC*. 71620.

[3] V. N. Bringi and V. Chandrasekar, *Polarimetric Doppler Weather Radar: Principles and applications*. Cambridge University Press, first ed., 2001.

[4] V. Chandrasekar, M. Schwaller, M. Vega, J. Carswell, K. Vijay Mishra, C. Nguyen, R. Meneghini, and W. Peterson, "The nasa dual-frequency dual-polarized doppler radar (d3r) system for gpm ground validation," in *EGU General Assembly Conference Abstracts*, vol. 12, p. 5578, 2010.

[5] R. M. Beauchamp, V. Chandrasekar, H. Chen, and M. Vega, "Overview of the d3r observations during the ifloods field experiment with emphasis on rainfall mapping and microphysics," *Journal of Hydrometeorology*, vol. 16, no. 5, pp. 2118–2132, 2015.

[6] V. Chandrasekar, R. M. Beauchamp, M. Vega, H. Chen, M. Kumar, S. Joshil, M. Schwaller, W. Petersen, and D. Wolff, "Meteorological observations and system performance from the nasa d3r's first 5 years," 2017.

[7] V. Chandrasekar, H. Chen, R. M. Beauchamp, M. Vega, M. Schwaller, W. Petersen, D. Wolff, and D. Willie, "Deployment and performance of the nasa d3r during gpm ifloods field campaign," in *Geoscience and Remote Sensing Symposium (IGARSS), 2014 IEEE International*, pp. 4970–4973, IEEE, 2014.

[8] V. Chandrasekar, R. M. Beauchamp, H. Chen, M. Vega, M. Schwaller, D. Willie, A. Dabrowski, M. Kumar, W. Petersen, and D. Wolff, "Deployment and performance of the nasa d3r during the gpm olympex field campaign," in *Geoscience and Remote Sensing Symposium (IGARSS), 2016 IEEE International*, pp. 2142–2145, IEEE, 2016.

[9] D. N. Moisseev and V. Chandrasekar, "Nonparametric estimation of raindrop size distributions from dual-polarization radar spectral observations," *Journal of Atmospheric and Oceanic Technology*, vol. 24, no. 6, pp. 1008–1018, 2007.

[10] N. Bharadwaj and V. Chandrasekar, "Wideband waveform design principles for solid-state weather radars," *Journal of Atmospheric and Oceanic Technology*, vol. 29, no. 1, pp. 14–31, 2012.

[11] V. Chandrasekar, Y.-G. Cho, D. Brunkow, and A. Jayasumana, "Virtual csu-chill radar: The vchill," *Journal of Atmospheric and Oceanic Technology*, vol. 22, no. 7, pp. 979–987, 2005.

[12] M. Kumar, S. S. Joshil, M. Vega, V. Chandrasekar, and J. W. Zebley, "Nasa d3r: 2.0, enhanced radar with new data and control features," in *Geoscience and Remote Sensing Symposium (IGARSS), 2018 IEEE International*, IEEE, 2018.

[13] M. Kumar, S. S. Joshil, V. Chandrasekar, R. M. Beauchamp, M. Vega, and J. W. Zebley, "Performance trade-offs and upgrade of nasa d3r weather radar," in *Geoscience and Remote Sensing Symposium (IGARSS), 2017 IEEE International*, pp. 5260–5263, IEEE, 2017.

[14] C. M. Nguyen and V. Chandrasekar, "Sensitivity enhancement system for pulse compression weather radar," *Journal of Atmospheric and Oceanic Technology*, vol. 31, no. 12, pp. 2732–2748, 2014.

[15] P. Joe, J. Scott, A. Siggia, and R. Passarelli Jr, "Random phase processing for the recovery of second trip echoes," in *COST-75 International Seminar*, pp. 20–23, 1994.

[16] R. J. Doviak *et al.*, *Doppler radar and weather observations.* Courier Corporation, 1993.

[17] Q. Cao, G. Zhang, R. D. Palmer, and L. Lei, "Detection and mitigation of second-trip echo in polarimetric weather radar employing random phase coding," *IEEE Transactions on Geoscience and Remote Sensing*, vol. 50, no. 4, pp. 1240–1253, 2012.

[18] K. Golestani, V. Chandrasekar, and R. J. Keeler, "Dual polarized staggered prt scheme for weather radars: Analysis and applications," *IEEE transactions on geoscience and remote sensing*, vol. 33, no. 2, pp. 239–246, 1995.

[19] S. M. Torres, Y. F. Dubel, and D. S. Zrnić, "Design, implementation, and demonstration of a staggered prt algorithm for the wsr-88d," *Journal of Atmospheric and Oceanic Technology*, vol. 21, no. 9, pp. 1389–1399, 2004.

[20] N. Bharadwaj and V. Chandrasekar, "Phase coding for range ambiguity mitigation in dual-polarized doppler weather radars," *Journal of Atmospheric and Oceanic Technology*, vol. 24, no. 8, pp. 1351–1363, 2007.

[21] D. Zrinc and P. Mahapatra, "Two methods of ambiguity resolution in pulse doppler weather radars," *IEEE Transactions on Aerospace and Electronic Systems*, no. 4, 1985.

[22] M. Sachidananda and D. S. Zrnic, "Systematic phase codes for resolving range overlaid signals in a doppler weather radar," *Journal of Atmospheric and Oceanic Technology*, vol. 16, no. 10, pp. 1351–1363, 1999.

[23] D. Chu, "Polyphase codes with good periodic correlation properties (corresp.)," *IEEE Transactions on information theory*, vol. 18, no. 4, pp. 531–532, 1972.

[24] J. Y. Cho, "Multi-pri signal processing for the terminal doppler weather radar. part ii: Range–velocity ambiguity mitigation," *Journal of Atmospheric and Oceanic Technology*, vol. 22, no. 10, pp. 1507–1519, 2005.

[25] N. Bharadwaj, V. Chandrasekar, and F. Junyent, "Signal processing system for the casa integrated project i radars," *Journal of Atmospheric and Oceanic Technology*, vol. 27, no. 9, pp. 1440–1460, 2010.

[26] S. Lim and V. Chandrasekar, "A robust attenuation correction system for reflectivity and differential reflectivity in weather radars," *IEEE Transactions on Geoscience and Remote Sensing*, vol. 54, no. 3, pp. 1727–1737, 2016.

[27] R. Bechini and V. Chandrasekar, "A semisupervised robust hydrometeor classification method for dual-polarization radar applications," *Journal of Atmospheric and Oceanic Technology*, vol. 32, no. 1, pp. 22–47, 2015.